The Strength of Polycrystalline Silicon at the Micro- and Nano-Scales with Applications to MEMS

Thesis by

Ioannis Chasiotis

In Partial Fulfillment of the Requirements

for the Degree of

Doctor of Philosophy

California Institute of Technology

Pasadena, California

2002

(Defended July 6, 2001)

© 2002

Ioannis Chasiotis

All Rights Reserved

Gratefully dedicated to all who remained faithful during this journey

Αφιερωμένο με ευγνωμοσύνη σε όσους έμειναν πιστοί ως το τέλος αυτού του ταξιδιού

Acknowledgements

The very first person I would like to fully acknowledge is my research advisor and mentor, Professor Wolfgang G. Knauss, for his unconditional and continuous trust, his constant support and his undeniably strong and catalytic influence in my development as a young scientist and member of the research community. His devotion to meticulous scientific work and his cautious guidance was my inspiration and the source to draw strength and confidence during my work. It has been a pleasure and a great privilege for me to work with Professor Knauss and learn from his experience.

A professor who has been very influential to my personal and professional development is Professor Guruswami Ravichandran who patiently helped me with the long process of searching for an academic position and shared with me his thoughts and concerns about my progress. I would also like to acknowledge him and Professors David Goodwin, Ersan Ustundag and Yu-Chong Tai for kindly accepting to participate in my thesis committee. I would also like to thank Professor Ares Rosakis for all the in depth discussions about my work and his influential teaching, Professor Brent Fultz for introducing me to the reign of Transmission Electron Microscopy (TEM), Professor Daniel Rittel for initiating me in the field of fractography, and Dr. Sangwook Lee for providing me with his invaluable assistance in learning ABAQUS.

I also want to take this opportunity to thank Dr. Russell Lawton from the Jet Propulsion Laboratory (JPL) for all his devoted effort to create the JPL-Caltech Reliability Alliance and I wish him all the best in his long journey and Dr. David LaVan from the Sandia National Laboratories for kindly providing the tensile specimens for the study on size effects.

In addition I want to thank the people who facilitated this work, especially Mr. Petros Arakelian, from our technical staff, and the invaluable administrative assistants, Ms. Denise Thobe, Mrs. Danna Griego and Mrs. Cynthia Torres, for their help and friendship.

This project was initiated as an exploratory study in the "Experimental Mechanics" (Ae104c) course in 1997 and preliminary work was conducted with Mr. Nitin Deshpande who contributed to the initial decision-making.

Of course very little would have been accomplished without the financial support by the Airforce Office of Scientific Research (AFOSR) through grant F49629-97-1-0324 (Round Robin Program) including funds from the National Science Foundation (NSF), under grant F49620-99-1-0091, with Major Brian Sanders, Drs. O. Ochoa, D. Segalman, and T. Hahn as the monitors.

After long coffee discussions with a good friend I concluded that all that matters in ones career is the existence of a strong support system, which is strictly human in nature. The desire to accomplish is irreplaceable in the quest for success but one needs the everyday support, especially when "the trip is long and the destination is not yet in sight". The first person who provided this support to me and I must sincerely thank is my brother, Christos, who has always been, in his own way, there for me. I also want to thank my parents for their continuous support while I was away from them, as well as for the faith and the confidence they have shown to my choices. I cannot also forget the continuous support by two close friends, who, although were thousands of miles away, kept our friendship alive withstanding the eroding effects of time and distance. They are

my dear friends Prodromos and Elpida who always reminded me that there were people thinking about me in my struggle away from home. I would also like to express my appreciation to Mr. Georgios Zamanakos (or σύμβουλας), a friend I could rely on all these years and discuss my problems and concerns with him.

I would also like to acknowledge a number of people who have been very supportive all those years. These are my friends at Caltech who taught me a lot and were by my side when I needed their help. I would like to specifically thank my lab mate and dear friend, Dr. Ying Huang, who helped me to get started in the lab and taught me how to use the Atomic Force Microscope (AFM). I would also like to thank the numerous Caltech friends I had lunch, coffee and dinner together and especially my friends Dr. Shiming Zhuang for the endless discussions about life, principles and human virtues, Dr. Murat Vural for his all his help and support on many everyday matters and Dr. Eric Burcsu for always being a person I could ask for help when I had a problem.

Abstract

Three aspects concerning the reliability of MicroElectroMechanical Systems (MEMS) are discussed in this work. These aspects are: (1) the development of a new tensile testing technique for measuring the elastic modulus and rupture strengths of thin films, (2) an assessment of stress concentration and specimen size effects in failure of micron-sized specimens and (3) the consequences of Hydrofluoric Acid (HF) chemical treatment on the microstructural integrity and the tensile strength of polycrystalline silicon.

A new method for tensile testing of thin films by means of an improved apparatus has been developed to measure the elastic properties (Young's modulus, tensile strength) of surface micromachined polycrystalline silicon specimens. The newly designed tensile tester makes use of an Ultraviolet (UV) light curable adhesive to clamp micron-sized specimens. It permits for the first time the testing of thin film materials possessing high failure strength. The properties determination utilizes surface topologies of deforming specimens, acquired with an Atomic Force Microscope (AFM), for determining strain fields by means of Digital Image Correlation (DIC). This full-field, direct and local measurements technique provides the capability of testing any type of thin film materials with nanometer resolution. The gage section of the specimens tested in this study varied between 200 and 1000 μm in length, 6 and 50 μm in width, all for a nominal thickness of 2 μm.

The dependence of fracture strength on micron and sub-micron sized geometries was studied by means of specimens containing various degrees of stress concentrations. A systematic study of small-scale size effects was thus performed by tensioning

elliptically perforated specimens (minimum radius of curvature of 1 μm) so as to: (a) vary the stress concentration with constant radius of curvature, (b) increasing radius of curvature of micronotches relative to the grain size. The results demonstrate a strong influence of the size of the highly strained domain (decreasing notch radii) on the failure strength of MEMS scale specimens, while the effect of varying the stress concentration factor is rather insignificant. In addition, tests performed on unnotched tensile specimens of varying dimensions revealed a specimen size effect by which the values of strength scaled with the specimen length. The Young's modulus, however, is found to be rather insensitive to the specimen dimensions at the scale of microns.

In an effort to assess the unexplained and puzzling large variation in properties reported for very small polysilicon specimens a study was conducted to search for a cause. Contrary to the common belief that 49% HF wet release represents a safe post-process for manufacturing polycrystalline silicon, this study has clearly identified the release process as a key item in determining thin film failure properties. It is found that surface roughness as characterized by groove formation at the grain boundaries depends distinctly on the HF release time. In addition, while the actual failure mechanism in polysilicon follows a transgranular fracture, moderate exposure in HF results in partial intergranular fracture at the film surface that is responsible for complete failure. Long exposures yield films of low mechanical strength that demonstrate clear intergranular failure.

Contents

Acknowledgements v

Abstract viii

Contents x

Figures xiii

Tables xviii

Introduction 1

1.1 The Role of Mechanics in MicroElectroMechanical Systems (MEMS) 1

1.2 Experimental Mechanics at the Micron Scale 4

1.3 Outline of Present Work 9

Measurements at the Submicron Scale 10

2.1 Instrumentation for Microtensile Testing 10

2.2 Microtensile Specimens 17

2.2.1 Design of Microtensile Specimens *17*

2.2.2 Microfabrication of Micron-Sized Specimens *21*

2.2.3 Release and Post-Processing of Specimens *25*

2.3 Strain Measurement 27

2.4 Error Analysis for the Experimental Technique 29

2.5 Microtensile Tests of Polysilicon Specimens 32

2.5.1 Calculation of the Elastic Modulus Based on Compliance Measurements *32*

2.5.2 Modulus Calculation Based on AFM Measurements 37

2.6 Specimen Characterization and Metrology 39

2.6.1. Specimen Microstructure and Surface Topography 39

2.6.2. Measurement of Specimen Thickness 43

2.7 Discussion 44

Influence of Scale on Strength **49**

3.1 Introduction 49

3.2 Tensile Tests of Perforated Micro-Specimens 51

3.2.1 Equations and Assumptions 51

3.2.2 Finite Width Correction Factors 55

3.2.3 Design of Perforated Micro-Tensile Specimens 58

3.2.4 Numerical Calculation of Stresses in a Finite, Perforated Plate 63

3.2.5 Calculation of the Finite Width Correction Concentration Factor 64

3.2.6 Results and Data Analysis 66

3.3 Specimen Size Effect 74

3.3.1 Weibull Statistical Analysis of Failure 75

3.3.2 Specimen Design and Testing 77

3.3.3 Failure Analysis 82

3.3.4 Discussion and Implications 85

Effects of Prolonged Exposure to HF **87**

4. 1 Introduction 87

4.2 Effects of Exposure of Polycrystalline Silicon to HF Solutions 88

4.3 Discussion 98

Comments and Conclusions **104**

References **107**

APPENDIX **115**

A. Calculation of the Voigt - Reuss - Hill Bounds 115

Figures

Figure 1.1 Failure of a micromotor shaft during operation [10]. 3

Figure 1.2 Failure of microgyroscope in simulated launch environment (Provided by Dr. Russell Lawton, JPL). 3

Figure 1.3 Tensile specimen with nominal dimensions of 100x5x2 microns. 8

Figure 1.4 Detail of figure 1.3 indicating the inhomogeneous and anisotropic polycrystalline structure of polysilicon. 8

Figure 1.5 Surface roughness of the marked area in figure 1.4 as recorded by an AFM... 8

Figure 2.1 Outline of the major components of the experimental setup. 11

Figure 2.2 The key parts of the microtensile testing apparatus. 11

Figure 2.3 Diagram of the load cell calibration. 12

Figure 2.4 Side view of the specimen via a 300x magnification microscope. The sample (top) and its reflection on the substrate (bottom) are parallel indicating proper alignment. The right side of the image is the transition to the paddle. 13

Figure 2.5 Successive steps of film gripping using UV curable adhesive. 16

Figure 2.6 Tensile specimens designed on a silicon chip, using the MUMPs surface micromachining process. The film thickness is nominally 2 μm. 18

Figure 2.7 Schematic of a die with six freestanding specimens from MUMPs21. 21

Figure 2.8 Schematic of a die with 14 freestanding specimens from MUMPs35. 21

Figure 2.9 Cross-section of the die after successive depositions of structural and sacrificial layers [22]. 23

Figure 2.10 Cross-section of the final structures after exposure to 49% HF removes the sacrificial layers [22]. 24

Figure 2.11 AFM data sampling along a scan line on polysilicon surface. 31

Figure 2.12 Load *vs.* total elongation of the specimen and the test apparatus. 33

Figure 2.13 Load *vs.* elongation of the test apparatus. 33

Figure 2.14 Fractured tensile specimen attached to the glass grip. 35

Figure 2.15 Fractured specimen indicating dynamic failure in the gage section. The area marked by the dashed line is modeled via ABAQUS as seen in figure 2.16. 35

Figure 2.16 σ_{11} stress contours of the marked specimen area as calculated per ABAQUS. The circled areas mark stress concentrations with K=1.04. 36

Figure 2.17 AFM recorded surface topography at applied load of 0.06 N. 38

Figure 2.18 Displacement field for topography seen in 2.17. 38

Figure 2.19 SEM picture of the bottom surface of the specimen (MUMPs35). 40

Figure 2.20 SEM picture of the top surface and the sidewalls of the specimen (MUMPs 35). 40

Figure 2.21 SEM picture of the fractured cross-section of the specimen. The columnar grain structure can be seen from the grooves and the extrusions in the fractured section. The specimens were manufactured in MUMPs19. 40

Figure 2.22 Three-dimensional rendering of the surface topography revealing the columnar structure of the material and the surface roughness. The z-direction is exaggerated compared to the lateral dimensions to make the grain structure more apparent. 40

Figure 2.23 Grain structure and artificial coloration of MUMPs polysilicon according to the orientation obtained by TEM after focused ion beam sectioning. (Provided by Dr. Russell Lawton (JPL), after personal communication.) 41

Figure 2.24 Diffraction pattern for MUMPs polysilicon obtained with Co K_{α}. 42

Figure 2.25 Effect of annealing temperature on grain texture [30]................................ 43

Figure 2.26 Ratio of the actual Young's Modulus to the effective (experimentally measured) value, E_{eff}/E_{real}, determined from a bending test, as a function of the wavelength and the amplitude of the surface roughness. 47

Figure 2.27 Ratio of the actual Young's Modulus to the effective (experimentally measured) value, E_{eff}/E_{real}, determined from a tensile test, as a function of the wavelength and the amplitude of the surface roughness. 47

Figure 3.1 Geometry of an internal elliptical notch and stress distributions for K=11 [40]. 52

Figure 3.2 σ_v and σ_{max} along the y-axis for an elliptical notch with radius of curvature of ρ=8 microns and K=11. 54

Figure 3.3 σ_θ and σ_{max} along the y-axis for a circular hole of ρ=8 microns and K=3. 54

Figure 3.4 SEM micrograph of an elliptically perforated specimen.............................. 59

Figure 3.5 SEM micrographs of perforations with nominal K=3, 6, 8 as calculated by (3.5).. 61

Figure 3.6 Representative mesh for the numerical calculation of the stress field around an elliptical notch in a finite plate. The inset illustrates the detailed mesh used in the region of the notch tip.. 63

Figure 3.7 Numerically calculated σ_{11} stress for a specimen with nominal K=8, R=8. .. 64

Figure 3.8 Fracture cross-section of specimens with circular (K=3) and elliptical (K=6) notches with ρ=2 μm. 67

Figure 3.9 Experimental results of the local stress at failure at the tip of the notch for different stress concentrations. The dashed line shows the tensile strength.. 69

Figure 3.10 Local stress at failure for different stress concentrations. The gray bar indicates the minimum strength and the white bar, the scatter of the experimental data. 70

Figure 3.11 σ_{11} stress profile along the y-axis (according to figure 3.1) for constant K and different radii of curvature as calculated by the FEM model. 71

Figure 3.12 Tangential stress as computed by (3.5) for different K and same ρ. 72

Figure 3.13 Experimental values of the average local failure stress as a function of the radius of curvature. 73

Figure 3.14 Optical microscope images of tensile specimens manufactured by Sandia National Labs. The indicated dimensions are the Length x Width of the gage section. 79

Figure 3.15 Young's modulus measured from specimens with various gage sections.... 81

Figure 3.16 Tensile strength of microtensile specimens as a function of gage surface. .. 81

Figure 3.17 Bar chart of the tensile strength as a function of gage surface. 82

Figure 3.18 Probability of failure for different specimen lengths as a function of failure stress. The filled boxes are for 6 microns wide specimens and the empty boxes for 20 microns wide specimens 83

Figure 3.19 Scaling factor as calculated for different specimen dimensions. 84

Figure 3.20 Scaling factor as calculated for specimen of the same length. 84

Figure 3.21 Weibull distributions for $\sigma_0 = 1.2$ (left) and $\sigma_0 = 0$ GPa (right). 85

Figure 4.1 AFM line profiles of surface roughness for different etch times in 49% HF. 90

Figure 4.2 Tensile strength vs. exposure time in 49% HF. 91

Figure 4.3 Stress concentration at a surface groove as a function of surface roughness computed in ABAQUS. 92

Figure 4.4 Fracture cross-section of specimen exposed to HF for 13 minutes. The tensile strength was 0.95 GPa. 93

Figure 4.5 Cross-section of a specimen tested in tension. Note the "crust" on the top surface of the specimen (13 minutes of exposure to HF). 94

Figure 4.6 Specimens exposed for 13 minutes to HF demonstrated delamination of a surface layer (crust) and intergranular fracture at the top surface. 94

Figure 4.7 Fracture profile composed of a series of SEM pictures that indicates local intergranular fracture (see grooves on the top surface) as well as signs of transgranular failure at the cross-section. The film was exposed for 13 minutes to HF. 95

Figure 4.8 AFM image of intergranular failure by a through the thickness crack. 96

Figure 4.9 Detail of image 4.8 that shows crack arrest when a crack meets a grain........ 96

Figure 4.10 The marked groove indicates the missing columnar grain through the film thickness that corresponds to a grain diameter 0.3 microns. 97

Figure 4.11 Specimens exposed to HF for 20 min. Two matching surfaces with multiple cracks at the sides of the main crack. 97

Figure 4.12 Long exposure to HF leads to distinct intergranular fracture. 98

Figure 4.13 Characteristic "zipper" pattern of intergranular fracture. 98

Figure 4.14 Specimens from MUMPs19 strongly curled after long HF release........... 100

Tables

Table 2.1 Specimen designs and dimensions tested in this work 20

Table 2.2 Release times and drying process for every batch of specimens 26

Table 2.3 Round Robin results (MUMPs21) 34

Table 3.1 Nominal K and dimensions of tested perforated specimens 58

Table 3.2 Nominal vs. measured hole dimensions 62

Table 3.3 Stress concentration factors for the different perforations 65

Table 3.4 Stress gradient at the notch root and decay length for K=3 71

Table 3.5 Nominal dimensions and properties of tested samples 79

Table 3.6 Cross comparison of experimental results 80

Table 3.7 Results of Weibull analysis 84

Table A1. Silicon stiffness, c_{ij}, and compliance, s_{ij}, elastic constants 116

Table A2. Voigt - Reuss bounds for the elastic constants of polysilicon 116

CHAPTER 1

Introduction

1.1 The Role of Mechanics in MicroElectroMechanical Systems (MEMS)

The parallel progress in mechanics and electronics created a new technology that incorporates mechanics and electronics under the name of MicroElectroMechanical Systems (MEMS). It has rapidly become the most promising technology with seemingly unlimited potential to dominate modern and future scientific and technological developments [1-3]. Mechanics plays a leading role in the development of new MEMS applications that will lead future technology through devices that either perform basic functions, such as airbag accelerometers [4] and radio frequency microswitches for wireless communications, or advanced tasks, such as microgyroscopes, digital micromirror displays and pico-satellites. New systems with embedded microactuators, microsensors [5-6] and control devices that are developed for guidance, navigation, motion control and high resolution flow visualization, can provide experimental evidence about phenomena at small scales, verify fundamental principles and study quantum effects at the nanoscale [7]. Texas Instruments Inc.'s digital micromirror display, for example, acts as a spatial light modulator for projection displays using a large array of tilting micromirrors. Applications in microfluidics are the solutions to high efficiency chemical reactions or effective drug delivery, while BIOMEMS [8] are increasingly

gaining in interest in the biomedical engineering community. Cost effective solutions emerge due to the possible mass production of MEMS. In addition, these devices operate with minimal energy requirements.

New applications will incorporate advanced piezoelectric, ferroelectric, or magnetostrictive (smart) materials with enhanced functions to devise “intelligent” micromachines that offer hitherto unheard of performance. Whenever mechanics can replace electronics, it provides superior functionality not subject to undesirable electronic noise. For example, the classical electronic components of fiber-optic networks are replaced by optical MEMS [9] switches that enable the creation of arrays of miniature, high-capacity optical switches for future fiber-optic networks. New technologies have already emerged in the form of MicroOptoElectroMechanical Systems (MOEMS), BIOMEMS and NEMS (NanoElectroMechanical Systems), given that the electronics community, currently operating at the nanoscale for reproducing features with dimensions of 130 nm, presages that during the next decade new targets of 30 nm will be met.

The mass production of MEMS with identical geometries guarantees controlled performance to the designed standards. However, the reliability of these devices has to be meticulously assessed since this is a vital requirement for further progress. The 10^6 rpm micromotors, recently demonstrated by Sandia National Labs, unfolded the nearly unlimited potential of MEMS but their short operating life (figure 1.1) indicated the immediate need for a better understanding of the physical mechanisms that lead to failure due to wear. In a similar manner, structural failure of the microgyroscopes (figure 1.2) occurred in tests performed in a simulated launch environment, underlining the

catastrophic consequences of the lack of understanding the appropriate mechanical reliability constraints. New experimental techniques for mechanical and material properties measurements must be developed to address the critical and fundamental questions of constitutive and fracture behavior at the micro- and nano-scales and conduct measurements with nanometer resolution. The macroscopic behavior of the devices relies on their integrity at the nanometric level. Materials testing and stress analyses are key parts of this development and the existing experimental methods have to be refined or completely revised to match the new scales challenges and requirements. Necessary tools capable of providing visualization of deformations at small scales are already available; Scanning Electron Microscopes (SEM) and Transmission Electron Microscopes (TEM) are instruments capable of high resolution, while the Atomic Force Microscope (AFM) provides unprecedented resolving power and unparalleled flexibility to facilitate material tests in virtually any environment.

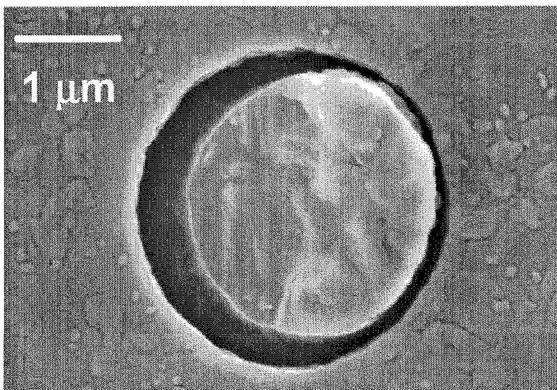

Figure 1.1 Failure of a micromotor shaft during operation [10].

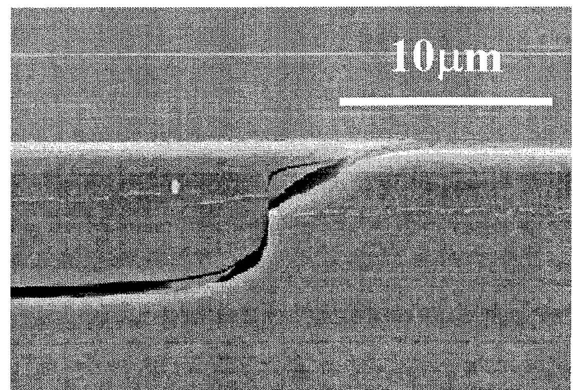

Figure 1.2 Failure of microgyroscope in simulated launch environment (Provided by Dr. Russell Lawton, JPL).

These new challenges have to be confronted by a methodical effort of the mechanics community concerned with MEMS. Device design, manufacturing, testing and reliability assessment need to be addressed in a coordinated effort that weights equally all the aforementioned aspects of MEMS development. Presently, the micromechanics field is largely application-driven, and reliability has been addressed without significant mechanics understanding; only a few case studies have been conducted, without developing the appropriate general tools and methods to resolve issues of mechanical integrity. Yet, the introduction of novel and important applications requires a thorough mechanics-based reliability assessment. Before the introduction and advancements of new micromachines are accomplished, the mechanics community needs to demonstrate the requisite progress; in this regard, residual stresses, stress concentration effects at micronotches and corners and failure by crack propagation are becoming increasingly frequent issues, often causing a halt to the research on new microstructures. The required experimental and analytical tools are, in principle, already available or progressed to a level of development that make such investigations feasible. It is necessary, however, that the mechanics research community pay careful attention to the early stages of the development of microtechnology and coordinate its efforts in this direction through an interdisciplinary effort.

1.2 Experimental Mechanics at the Micron Scale

The reliability of MEMS devices is a major issue and it can only be addressed by direct measurements on miniature specimens with dimensions on the same order of magnitude

as the fabricated microdevices. Thin film properties depend on the deposition and post-processing conditions and they are idiosyncratic for every clean room. There are several aspects of material properties that have to be addressed when developing a mechanical properties test method for MEMS devices. The method has to be flexible to provide measurements for different mechanical properties of interest. It is important that the experimental and testing technique possess the capability of testing structural materials other than polycrystalline silicon, that are considerably stronger, such as SiC, Si_3N_4 and amorphous diamond, materials that behave non-linearly, like Au, Cu or Al used for interconnects, Ni that is used as structural material in the LIGA process[1], or even viscoelastic and other polymeric materials, such as polyimides, that are important candidates for special applications. Polycrystalline silicon is a superb material to demonstrate the potential of micromachines, but the investigation of new MEMS devices indicates the need for new application-specific materials. The constitutive behavior of those materials is important to be measured without any assumptions that are currently often invoked to perform indirect measurements of strain. In addition to the constitutive behavior, other important quantities that are either (postulated) material properties, such as the critical stress intensity factor, or geometry-related effects, such as stress concentrations at notches and corners with dimensions comparable to the grain size, need to be studied. The latter are strictly local in nature and demand the use of direct measurements on the surface of the film at the area of interest, which cannot be addressed by the presently available strain measurements methods. Moreover, the test method has to

[1] Acronym for the German words for lithography, electroplating and molding.

possess the capability of conducting measurements in different environments, as, e.g., in vacuum, in air, in the presence of inert gases and humidity or at high temperatures. Until the relevant issues or problems are better understood, it seems important to develop a reliable method that addresses all the above, since the use of different approaches for each of the aforementioned conditions may result in a variety of uncorrelated data as demonstrated in previous round robin studies [11]. Finally, it is critical that the test method be able to address the characteristic length scale of the material at the dimensions of MEMS and possess spatial resolution that can capture the material microstructure, i.e., the grain size and the surface roughness (figures 1.3-1.5).

To date, polysilicon is the main structural material used in MEMS fabricated by surface micromachining. Various techniques have been developed in the past to address the issues of mechanical integrity and evaluation of the elastic properties of polysilicon [11-12]. Such properties depend on the microfabrication conditions, involving the grain size [13], deposition temperature, doping, annealing [14], chemical etching, etc. Methods based on membrane deflection [14], beam bending [15], tensile [11, 13, 16, 17, 18] and nanoidentation tests or resonant frequency measurements of microcantilever beams [11] have provided a span of values for the elastic constants. Prominent reasons for the variety of reported results are the considerable differences in the test methods, imprecise specimen geometries, unresolved boundary conditions and the physical differences in the tested material presumed nominally to be identical. The load deflection method [19], for instance, requires the knowledge of Poisson's ratio to evaluate Young's modulus and does not apply to compressively stressed films or to films that are difficult to make into membranes [14]. Moreover, since Poisson's ratio is unknown, the errors caused by

assuming its value are magnified in the evaluation of Young's modulus. For example, for calculating the bending moment in beam-bending tests, two contributions must be taken into account; the rotation of the cantilever support point due to the applied force and the moment due to the stress gradient through the thickness of the cantilever. For this method the precise knowledge of the film thickness is mandatory to evaluate accurately the mechanical constants.

In this context, surface roughness plays a potentially important role and, as is shown in Chapter 2, contributes to the overall error. A numerical analysis [20], for instance, proves that the error due to surface roughness in bending tests can be very important, sometimes exceeding the experimental and systematic errors, while its effect on tensile test data is minimal. Of the aforementioned techniques, tensile tests are less vulnerable to geometry-induced errors and the measurements are easier to interpret from the point of view of error analysis. The design and implementation of tensile test apparatus may be complicated, but can lead to effortless and accurate data interpretation. Uncertainties of the specimen thickness, density, undercuts, rigid body rotation at the specimen support, effect of the residual stress gradient in the actual deflection and the interpretation of the influence of those parameters on the experimental data are generally not an issue or can be incorporated in data processing. Tensile tests have been performed using electrostatics [17], adhesive media [13], or specially designed micromanipulators [16, 18] to grip the specimens, either in a scanning electron microscope (SEM), or interferometrically [21], to measure the displacements. Accurate and reliable properties, however, can only be obtained by direct measurements on small specimens with dimensions on the same order of magnitude as the fabricated microdevices.

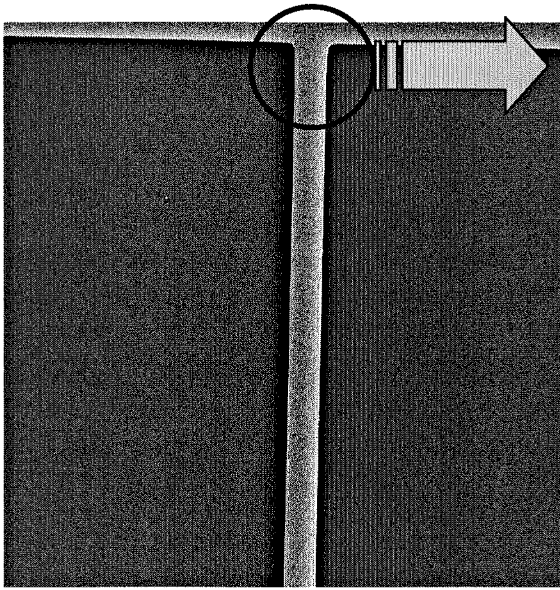

20μm 1000X

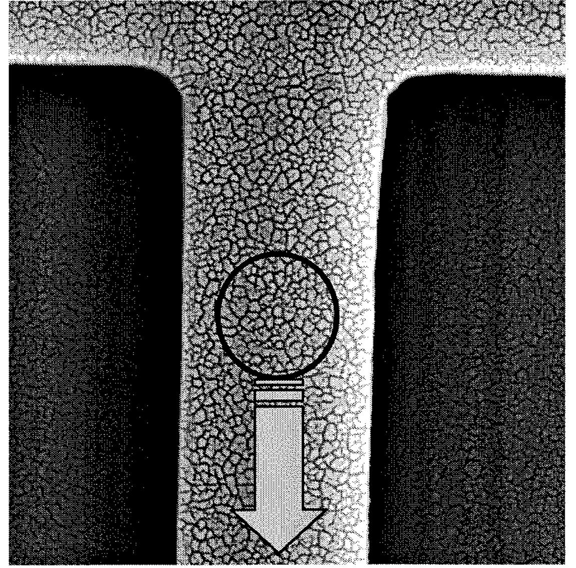

4μm 6000X

Figure 1.3 Tensile specimen with nominal dimensions of 100x5x2 microns.

Figure 1.4 Detail of figure 1.3 indicating the inhomogeneous and anisotropic polycrystalline structure of polysilicon.

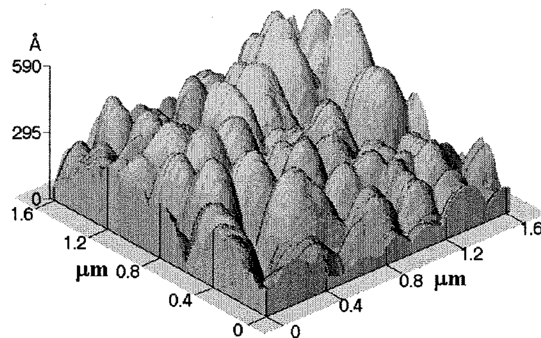

Figure 1.5 Surface roughness of the marked area in figure 1.4 as recorded by an AFM.

To date, there are no mechanical properties measurement techniques available for the microscale in accordance to the ASTM-approved standards that require measurement of strains in small domains directly on the specimens. In the present technique, direct, local and full field measurements on the specimen surface are obtained with nanometer

resolution by an AFM. This is important in understanding the deformation mechanisms in the submicron regime. The grain size of polysilicon is on the order of 300 nm. For specimen dimensions of a few microns (figure 1.3) the material substructure becomes important (figure 1.4). In the same manner, imaging the surface via an AFM reveals (figure 1.5) that the film is not atomically flat and the existing roughness induces stress amplifications and provides surface failure initiation sites.

1.3 Outline of Present Work

The following chapters illustrate the three primary components of this investigation. Chapter 2 discusses in detail the development of an experimental apparatus, a microtensile tester, to perform tensile tests on micron-sized specimens. The device facilitates the use of an AFM to perform measurements of the deformation directly on the surface of the thin film specimen. The use of this experimental apparatus along with the results is illustrated in performing tests on polycrystalline silicon specimens. In Chapter 3, the effect of specimen size on the modulus and the failure strength of micron-sized specimens is investigated. In parallel, the effect of stress raisers with various stress concentrations (K=3-12) and radii of curvature (ρ=1, 2, 3, 8 microns) on failure by fracture is examined. Chapter 4 is concerned with the effect of 49% wet HF etch, an important step in post-processing of MEMS microdevices, on the strength and microscopic integrity of polysilicon specimens. Finally, Chapter 5 summarizes the most important aspects of this work.

CHAPTER 2

Measurements at the Submicron Scale

2.1 Instrumentation for Microtensile Testing

An important aspect of the design of the experimental apparatus for MEMS testing is the inherent dependence of the specimen geometry on the test device layout. The test method needs to be formulated taking into account the combination of optimum specimen and apparatus design. Experimenting with small specimens demands the test device to be designed so that it simultaneously addresses the important issues of:

- Specimen mounting,
- Facilitation of the necessary electrical connections,
- Load cell, specimen and grip alignment, and
- Positioning under the AFM.

The experimental arrangement for subjecting small "dog-bone" shaped specimens to tension is outlined in figure 2.1 with a close up view of the experimental apparatus in figure 2.2. The displacements are imposed on the specimen via an inchworm actuator from Burleigh Corporation that is powered by a system of a personal computer and a dedicated controller. The controller provides a measurement of the system composite displacement (specimen + loading device) with an accuracy of 4 nm for every single step of the actuator where the smallest displacement induced by the controller is 10 nm. The

applied load is measured by a miniature tension/compression load cell with an accuracy of 10^{-4} N and maximum capacity of 0.5 N. The load cell has been calibrated in a vertical arrangement via dead-weight loading and the calibration diagram is shown in figure 2.3. The linearity of the load cell is excellent for small and high loads with correlation coefficient, R^2, equal to 0.9999, which implies almost absolute linearity.

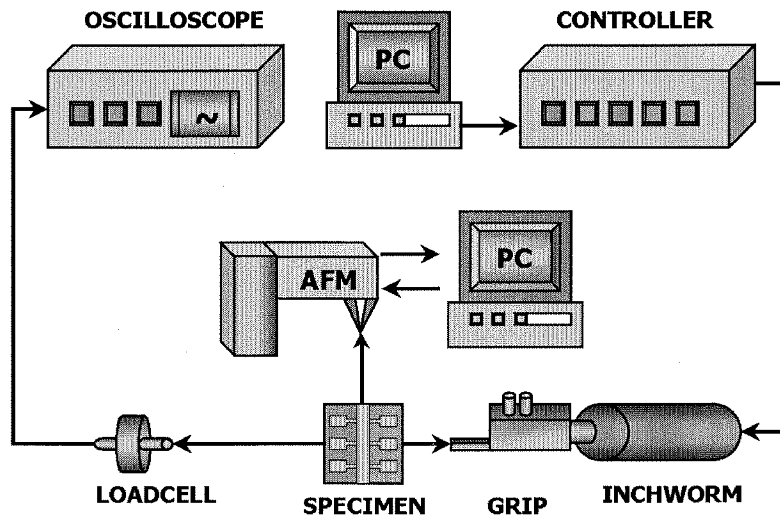

Figure 2.1 Outline of the major components of the experimental setup.

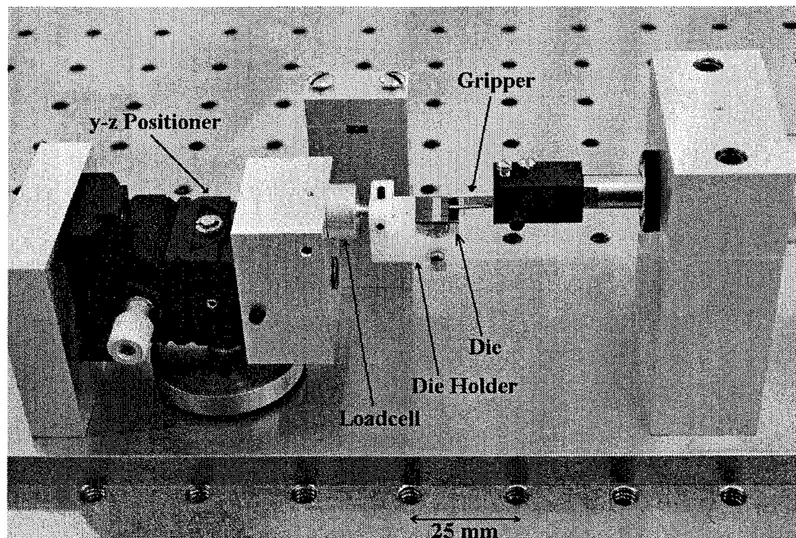

Figure 2.2 The key parts of the microtensile testing apparatus.

A miniature, manually operated, y-z translation stage from Newport Co. is employed for sample positioning relative to the grip, while the experimental setup allows for rotational adjustments about the x-axis (along the load cell - specimen - inchworm axis) and y-axis (on the plane of the specimen). The local deformation is monitored directly on the specimen surface with an AFM. The resolution of the y-z translation stage is on the order of 1 micron; this is sufficient so that proper positioning of the grip can be achieved in the close proximity of the specimen surface before applying the voltage, or curing the adhesive, as described later on. This capability assures satisfactory alignment, virtually eliminating any possible bending of the specimens during the test.

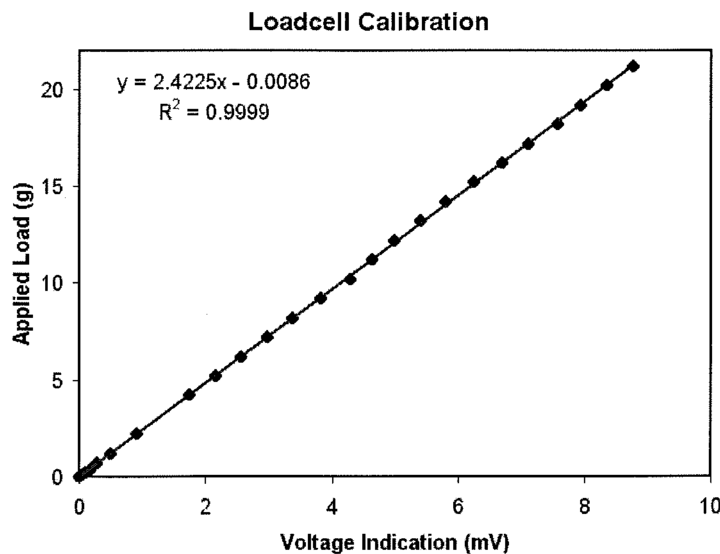

Figure 2.3 Diagram of the load cell calibration.

The performance of each individual component has been examined to establish their accuracy. The hysterisis and the linearity of the load cell have been evaluated to identify possible sources of error. The linearity of the load-extension curve is very good for our purpose (error < 0.10%). The effective value of hysterisis is on the order of 1.8%

of the maximum load, restricted only to loads below 0.05 N, and it is constant and consistent over a series of repeat measurements. The performance of the inchworm actuator has been calibrated via an AFM. In this way, a correction factor of 1.12 to the indication for the induced displacement by the controller and the actual motion of the actuator was established. A horizontally positioned 300x optical microscope provided a side view of the specimen during positioning (figure 2.4). This helped in prevent undesirable specimen bending or buckling and facilitated the monitoring of the specimen during the test. Due to the formation of native oxide with thickness of about 2 nm on the surface of the specimen (the tests were conducted in open air), the AFM was operated in Non-Contact Mode (NCM). In this mode the cantilever tip is not in physical contact with the sample but vibrates over a distance of 2-3 nm above the sample at its resonant frequency. This latter minimizes the effect of surface charges and induced vibration to the freestanding film by the cantilever tip during measurements.

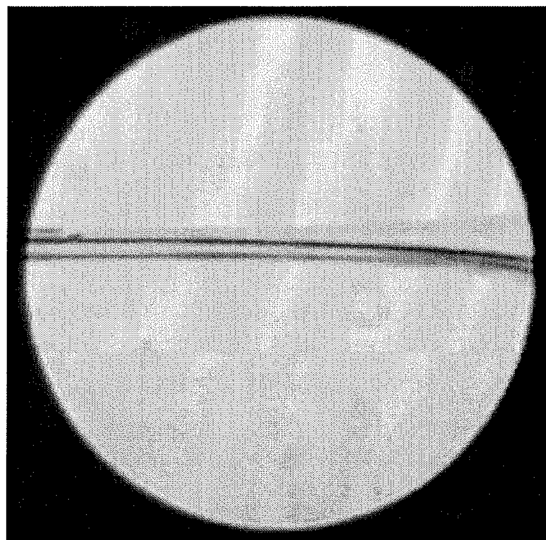

Figure 2.4 Side view of the specimen via a 300x magnification microscope. The sample (top) and its reflection on the substrate (bottom) are parallel indicating proper alignment. The right side of the image is the transition to the paddle.

The tensile tester, as originally designed, took advantage of the electrostatic forces that can be exerted between two conductive capacitor surfaces separated by a non-conductive medium[2]. The grip was comprised of a narrow silicon beam coated with a 200 nm Si_3N_4 insulating layer. The very thin electrical insulation made the necessary operational voltage relatively low. The electrical forces were sufficiently high to grip the specimen upon applying a potential of 10-20 Volts (since only the paddle's stiction against the substrate has to be overcome). The operating voltage was on the order of 80V. Voltages above 80-90 V resulted in arcing as will be described later. The surface of the insulated grip was smooth with a topography variation of 10-20 nm. This smoothness was the reason for the low values of friction coefficient that were observed, since the contribution to this value results mostly from the roughness on the top surface of the specimen.

The frictional force is derived from the equation

$$F_f = -n\frac{\varepsilon_0\varepsilon}{2}\left(\frac{V}{d}\right)^2 DL \tag{2.1}$$

where F_f is the frictional force, n is the friction coefficient between the two surfaces, ε_0 and ε are the dielectric constants of vacuum and silicon nitride ($\varepsilon=10^7$ V/cm) respectively, d is the silicon nitride insulation thickness, D, L are the width and length of the paddle respectively. This force and the electrical force exerted in a direction parallel to the paddle (which is minimal compared to the frictional force) contribute to the total force that loads the specimen.

---

[2] This technique was first introduced by Tsuchiya [17] for tensile tests performed in a SEM.

An electrostatic grip provides, however, a limited induced load capability for a certain combination of paddle size and insulator thickness, restricted by the friction coefficient between the paddle and the electrostatic grip. The applied voltage, in conjunction with the local arcing, can induce surface charges, thereby obstructing the use of a surface probing technique (AFM, STM). In addition, breakdown voltage and charging effects that occur due to the applied "high" voltage can easily cause severe damage to the test samples. Moreover, the recent trend to use materials other than polysilicon that have higher strength (SiC, Si_3N_4) and better functionality in harsh environments, indicated the need to redesign the tensile test device. A new, more efficient gripping method has been developed that makes use of a high viscosity Ultraviolet (UV) adhesive provided by Dymax Co. This newly developed tensile tester is free of any problems due to accumulated charges on the film and facilitates the test of high failure strength or non-linear materials, making the proposed approach a universal test method for different thin films that do not even necessarily need to be conductive.

The operation of the newly implemented grip is illustrated in figure 2.5. Electrostatic forces are applied (figure 2.5, I) to force the thin polysilicon film to lie flat on the substrate (due to the effect of the residual stress gradient, the released film may be curved in the out-of-plane direction, causing buckling if gripped "as is"). The glass grip is then moved (figure 2.5, II) towards the flat paddle. The grip is transparent to allow UV light to be transmitted and to cure the underlying adhesive layer effectively in a short time. Next, the two surfaces of the substrate and the specimen paddle, which adhere to each other electrostatically and due to stiction forces, are separated by changing the voltage polarity so that the film is now repelled by the substrate (figure 2.5, III) and

adheres to the grip covered by a thin UV adhesive layer. Strong capillary forces keep the paddle in contact with the glass grip until the glue is cured by a short exposure (less than one minute) to 365 nm UV light[3]. The aforementioned process eliminates the need of mechanically pressing the grip against the paddle and the substrate, the potential flow of the adhesive on the substrate and consequently pre-test specimen damage. It is also important to note that the new grip provided us with nearly 100% of successful tests, thus increasing by a factor of two the number of tests performed previously by the electrostatic grip.

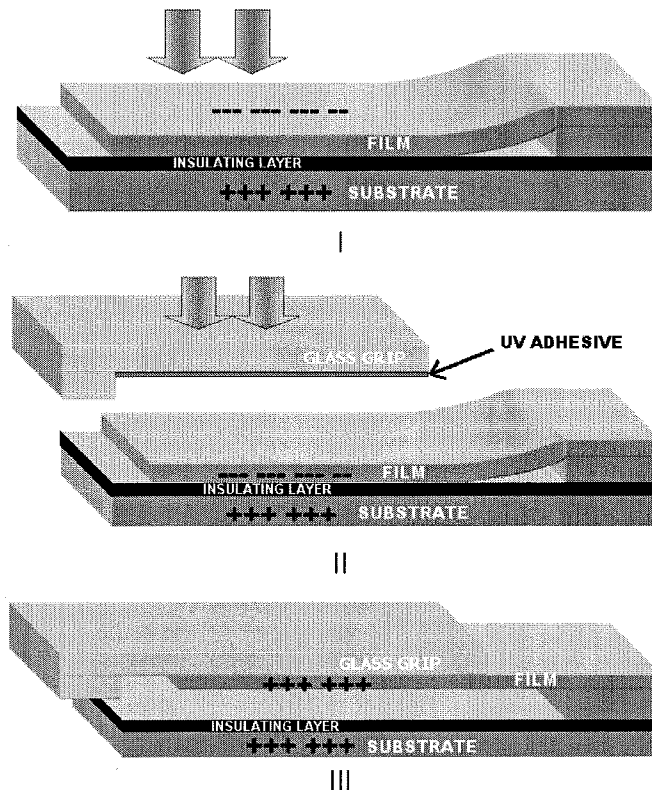

Figure 2.5 Successive steps of film gripping using UV curable adhesive.

---

[3] The light source used in this work was a 365 nm UV light lamp by

2.2 Microtensile Specimens

The preparation of microfabricated specimens involves a lengthy procedure that begins with the design of the different layers (or masks) using AutoCAD. More sophisticated software is available but at a prohibitive price. Theses designs converted to the appropriate file types (GDS II) are submitted to the Microelectronics Center in North Carolina (MCNC, currently Cronos) for fabrication that lasts about 8-10 weeks. The final chips (dies) are post processed to remove some of the previously deposited layers (sacrificial layers) and provide final free structures.

2.2.1 Design of Microtensile Specimens

Tensile, "bone-shaped" specimens with various gage section dimensions attached to a silicon wafer have been designed. The dimensions of the gage section varied from 400x80x2 microns to 400x6x2 microns (figure 2.6). They were freestanding beams ending in a large paddle for convenient "gripping." The deformation of the gage section was monitored by an AFM. Four thin gold markers 20x5 μm were also employed[4] to define a square area, opposing sides of which served as base length markers of "micro-strain gages." The adhesion of the gold markers, however, was typically weak and they were "drifted" by the AFM probe. The idea to incorporate wider markers [21] was abandoned, as their effect on the local deformation was apparent [20]. Three different types of specimens (with and without etch holes) were designed for three different

---

[4] Gold markers were used first by W. N. Sharpe in the development of an interferometric testing technique

microfabrication MUMPs runs (Multi User MEMS Process) at MCNC and are referred to as MUMPs19 (without release holes), MUMPs21 (with release holes) and MUMPs35, (with release holes) as illustrated in figure 2.6. The fact that the specimens rest on the substrate - due to their large lateral dimensions compared to the thickness - led to stiction after their release. This stiction demanded, in some cases, mechanical dislodging before testing the specimens.

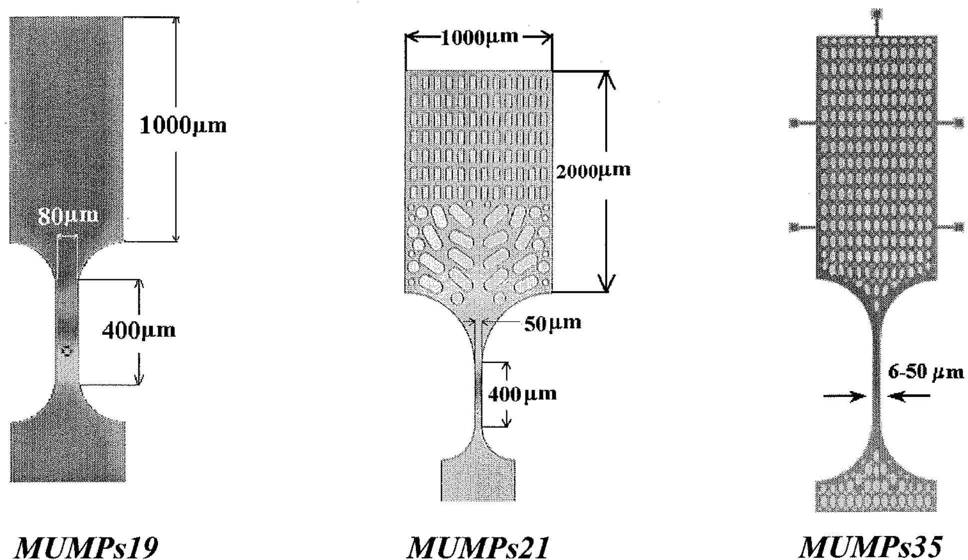

Figure 2.6 Tensile specimens designed on a silicon chip, using the MUMPs surface micromachining process. The film thickness is nominally 2 μm.

The specimens from MUMPs21 and later runs were designed so as to take into account the spatially frequent use of etch holes to facilitate the post-processing stage of wet oxide etching. The use of etch holes on the paddle (see figure 2.6) facilitated the rapid release of the structural polysilicon layer[5] from the underlying sacrificial silicon

[5] See also the description of the microfabrication process in paragraph 2.2.2.

oxide in short time so that the effect of HF on the metal layer is minimal. The pattern for the etch holes on the paddle was chosen to avoid specimen fracture from any stress concentrations in the transition from wide paddle to the test section. This pattern has been optimized in the case of specimens from MUMPs35 by placing the elliptical release holes along the contours of the maximum principal stress in the transition part. The use of "anchors" for the large paddle grip section (the small beams at the sides and the top of the paddle in figure 2.6 for MUMPs35) ensured failure-free handling before testing and decreased the risk of (potentially disastrous) specimen drift on the silicon die during the release process. A special probe stage, to be described in paragraph 2.2.3, has been built to sever the narrow anchor beams.

The MUMPs microfabrication process provides for every design 15 identical dies (chips) with dimensions of 1x1 cm each, and a potentially large number of test structures on each die. Figures 2.7 and 2.8 show the top view of the chips from MUMPs21 and MUMPs35 runs that included 6 and 14 specimens per die respectively.

Specimens designed for the MUMPs35 run took advantage of polysilicon dimples created at the bottom surface of the specimens. These dimples, bumps with a lateral diameter of 10 microns, assisted in reducing significantly the contact surface between the paddle and the substrate and reduced the risk of attendant stiction problems.

The specimen dimensions varied considerably from run to run. The nominal dimensions and geometries of all samples tested in this work are listed in table 2.1.

Table 2.1 Specimen designs and dimensions tested in this work

Micro-Fabrication Process	***Film Thickness (μm)***	***Paddle dimensions (LxW), (μm)***	***Gage Section Dimensions (LxW), (μm)***	***Notch Type***	***Notch Dimensions (txρ)[6], (μm)***
MUMPs19	2	1000x500	400x80	N/A	N/A
MUMPs21	2	2000x1000	500x50	N/A	N/A
MUMPs35 (Chapter 3)	2	1400x700	500x50	N/A	N/A
	2	1400x700	500x30, 500x60, 500x60, 800x160	Circular	1x1, 2x2, 3x3, 8x8
	2	1400x700	500x50, 500x100, 500x150, 800x280	Elliptical	6x1, 12x2, 18x3, 50x8
	2	1400x700	500x50, 500x100, 500x150, 800x340	Elliptical	12x1, 24x2, 36x3, 98x8
Sandia SUMMiT V (Chapter 3)	2.5	1000x600	250x20, 250x6 1000x20, 1000x6	N/A	N/A

[6] t is the notch long axis and ρ is the radius of curvature.

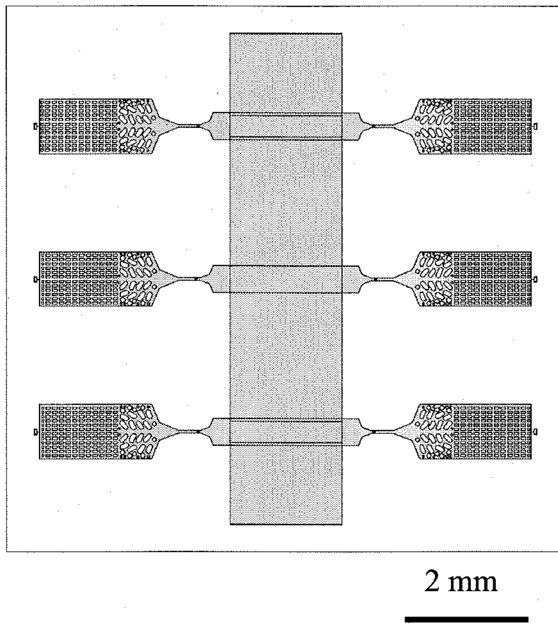

Figure 2.7 Schematic of a die with six freestanding specimens from MUMPs21.

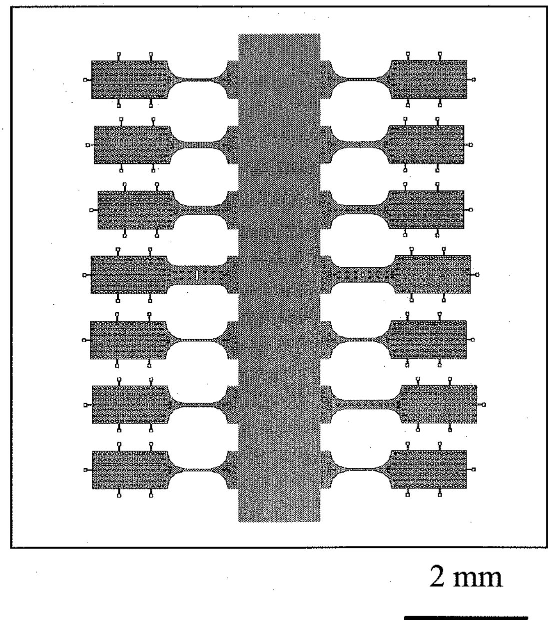

Figure 2.8 Schematic of a die with 14 freestanding specimens from MUMPs35.

2.2.2 Microfabrication of Micron-Sized Specimens

The MUMPs process [22] was used to manufacture our surface micromachined specimens. This process uses two polysilicon layers as structural material. A silicon wafer with (100) orientation, heavily doped with phosphorus via $POCl_3$, is used as substrate. First, a 600 nm electrical insulation layer of low-stress silicon nitride (see NITRIDE in figure 2.9) is deposited by low-pressure chemical vapor deposition (LPCVD). This layer is essentially a hard insulation to isolate the structures from the substrate. The first (nonstructural) 500 nm layer of polysilicon (POLY0) is deposited by LPCVD and is photolithographically patterned by exposing a photoresistive material with

the appropriate mask and developing the exposed photoresist to create the desired etch mask for subsequent pattern transfer into the underlying layer. The photoresist is etched away by Reactive Ion Etching (RIE). This is followed by a 2.0 μm phosphosilicate glass (PSG) LPCVD deposition (1st OXIDE) and annealing at 1050 °C for 1 hour in argon. The latter is a sacrificial layer and, by being lithographically patterned, can provide dimples under the next polysilicon film. The dimples, with nominal depth of 750 nm, are transferred into the sacrificial PSG layer by RIE.

A mask is used to etch holes in the PSG and provide anchor holes to be filled by the subsequent polysilicon layer. Then a 2.0 μm thick polysilicon structural layer (POLY1) is deposited followed by a 200 nm PSG layer and annealing at 1050 °C for 1 hour. This provides uniform doping to the first structural polysilicon layer on both sides and reduces the residual stresses in the structural layer. The polysilicon and the PSG masking layer are lithographically patterned using a mask to define the structures built by the first structural layer. This polysilicon layer is the material tested in this work. The hard mask is more resistant to the polysilicon etch chemistry than the photoresist and ensures better transfer of the pattern into the polysilicon. After etching the polysilicon the photoresist is stripped and the remaining oxide hard mask is removed by RIE.

In the next step, a second PSG layer (2nd OXIDE) is deposited and annealed. The second oxide is patterned by using two different etch masks with different objectives. One is used to create holes in the second oxide layer and thus provide mechanical and electrical connection between the two structural layers. This oxide layer is lithographically patterned and etched by RIE. A second etch mask is used to etch both the first and the second oxide layers in one step and create anchors for the topmost

polysilicon layer. This eliminates any misalignment between separately etched holes. This layer is lithographically patterned and etched by RIE.

The second structural layer is then deposited (1.5 μm thick) followed by the deposition of 200 nm PSG. As with the first polysilicon layer, the thin PSG layer acts as both an etch mask and a dopant source for the second structural layer. The wafer is annealed for one hour at 1050 °C to dope the polysilicon and reduce the residual stress. The second polysilicon layer is lithographically patterned and the PSG and polysilicon layers are etched by RIE using the same processing conditions as for the first structural polysilicon layer. The photoresist is then stripped and the masking oxide is removed. Finally, the wafer is patterned lithographically to create the metal contacts and a 0.5μm layer of gold with a thin chrome adhesion layer is deposited and patterned using lift-off. The photoresist and the unwanted metal are then removed in a solvent bath. This is the last step of the pre-release microfabrication process. The final layout is illustrated in figure 2.9.

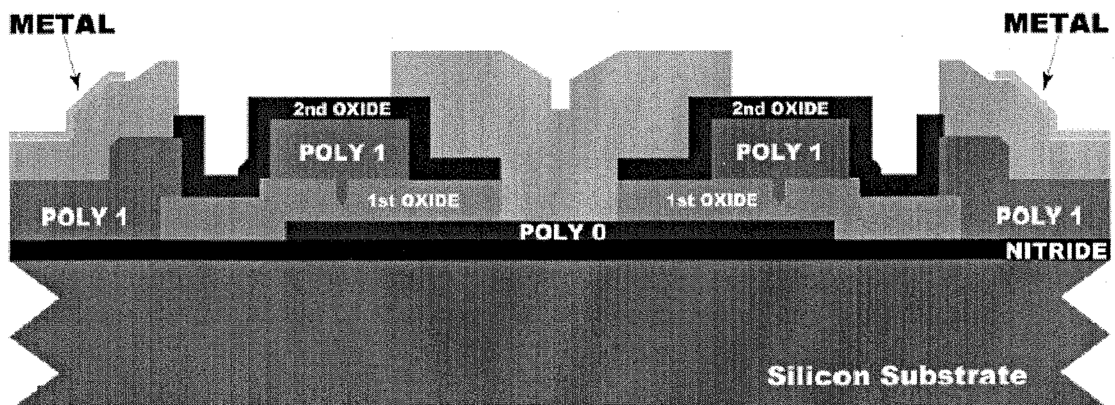

Figure 2.9 Cross-section of the die after successive depositions of structural and sacrificial layers [22].

The removal of the sacrificial layer (release of the structures) is performed by immersing the chip in a bath of 49% HF for a sufficient amount of time that depends on the size of the structures and the density of the etch holes. This is followed by rinsing the dies with de-ionized water and then methanol to reduce stiction. Then the dies are baked for 10 minutes at 1100 °C. In this work, the CO_2 supercritical process was used in most cases instead of baking the dies to reduce the risk of stiction. During the CO_2 supercritical drying process, following the rinse in alcohol, the die is immersed in a CO_2 bath that undergoes a thermal cycle through the triple phase point and the liquid phase changes to gaseous form with an attendant decrease of the capillary forces (and thus stiction) in the resulting free structures. A cross-section of the final microfabricated structures is shown in figure 2.10.

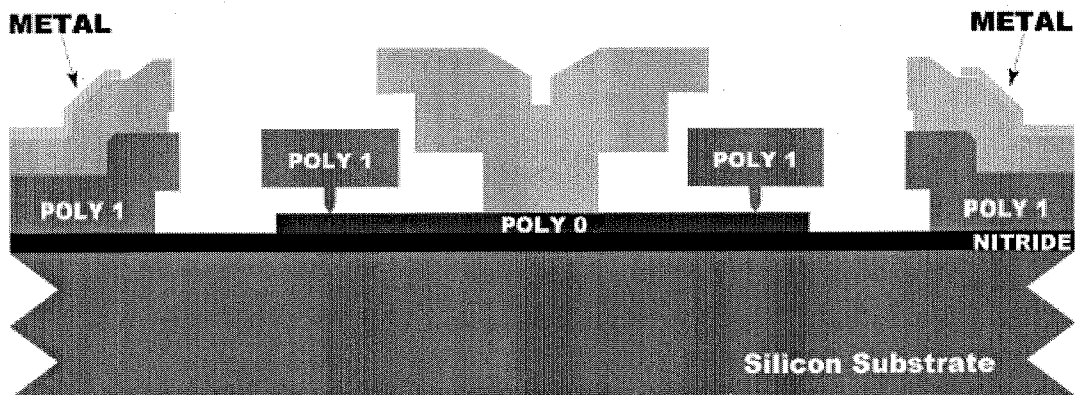

Figure 2.10 Cross-section of the final structures after exposure to 49% HF removes the sacrificial layers [22].

2.2.3 Release and Post-Processing of Specimens

The first specimens designed with solid paddles (MUMPs19) suffered from repeated stiction. The total release time needed to release the structures at MCNC was 20 minutes in 49% HF with water rinse and methanol treatment and finally oven baking. During the release, the specimens became strongly "curved up" in water and subsequently in alcohol, but they finally remained adhered to the wafer surface. The bending was attributed to the high compressive stresses in the polysilicon as a result of the prior deposition on PSG and the mismatch of the thermal expansion coefficient. After HF release, stiction was a major problem with the specimens from MUMPs19. The main causes were the large contact surface and the lack of etch holes and dimples at the bottom of the samples.

The adhesion forces were strong enough to overcome the action of the restoring elastic forces and thus the beams could not be freed from the substrate. Several types of forces can contribute to this phenomenon; depending on the separation of two surfaces, their intensity varies and in general they are the capillary, electrostatic, van der Waals, solid bridging and hydrogen bonding forces [23, 24]. Several solutions [23] have been proposed to avoid stiction, but in the present case stiction was severe and the only solution was to probe the structures mechanically with a fine tool tip. To this end, a very sensitive and accurate device with a very sharp tip was built, so that the movement of the tip would not damage the specimens. The tip was manufactured by the same technique used to fabricate sharp tips for STM instruments by subjecting a 100 μm in diameter Tungsten wire to 1 N NaOH solution and applying a potential of 2 V.

Stiction was limited in specimens from MUMPs21 and MUMPs35 after adding tethers to keep the sides of the paddle away from the substrate and dimples under the

paddle to minimize the total contact surface between the paddle and the substrate. These specimens were dried using the CO_2 supercritical drying process. Specimens that have been treated using this process have demonstrated very limited stiction effects and facilitated easy testing in our apparatus.

Specimens that have been designed for MUMPs35 did not suffer from the stiction problem because of the included dimples (10 microns in diameter) that considerably reduced the contact area between the paddle and the substrate. Specimens fabricated in different runs or facilities were treated in different ways and with different release times and drying process. The details of every specimen set are presented in table 2.2.

Table 2.2 Release times and drying process for every batch of specimens

Microfabrication Process	**Release Time (min) / Release Agent**	**Drying Process**	**Post -Processing Facility**
MCNC MUMPs19	19 (49% HF)	Oven Bake	MCNC
MCNC MUMPs21	13 (49% HF)	CO_2 Supercritical	MCNC
MCNC MUMPs35	15 (49% HF)	CO_2 Supercritical	MCNC
Sandia SUMMIT V	90 (1:1 49% HF:H_2O)	CO_2 Supercritical	Sandia N.L.

2.3 Strain Measurement

Displacement and strain measurements in micromechanical testing are a cumbersome task, mainly because of the lack of techniques that can provide accurate and direct measurements of deformations. Although high-resolution microscopy tools do exist, handling of microscopic samples is not mature yet. Displacement measurements are usually performed in an average manner with the best of the available techniques [21] measuring the displacement of a single point on the surface of the deforming thin film using an interferometric technique. In the present work, the design of the test setup has multiple functions: First, it allows for measurements of the average deformation. In this operation, the compliance of the experimental setup is measured by attaching the grip to the die and applying load. The load *vs.* displacement curve is recorded and the compliance of the test apparatus is calculated. During a tensile test the combined compliance of the test apparatus and the specimen are measured. Then, using a linear spring model the effective modulus of elasticity for polysilicon is calculated. The percentage of the system compliance to the specimen compliance is 10%-12% for the specimens manufactured at MUMPs21 and 2%-6% for the specimens provided by the Sandia National Labs.

The advantage of the present AFM probe technique is the capability of full field and direct measurement of the deformation field obtained on the surface of the film. In this approach, the topography of the film is obtained by an AFM at different load levels. The successive AFM images are correlated by Digital Image Correlation (DIC) to calculate the displacements. The latter are used to extract the strain field. By making use

of the nominal tension stress that is calculated for the measured applied load and the nominal cross-section, the Young's modulus is obtained.

The DIC [25-27] method is used to resolve relative displacements through an interpolation scheme. The deformation of part of the test section is monitored by an AFM, making use of the natural surface roughness features as distributed markers. This method of extracting in-plane deformations requires the ability to follow shape changes by comparing (surface) records before and after deformation. This information is obtained by a probe microscope (AFM) through records of surface features taken before and after deformation and then computing from this information the movement of the (three-dimensional) surface features. DIC achieves this by defining a correlation coefficient as a function of the kinematic transformation relating the deformed to the undeformed geometry. The displacements and strains are parameters in this mapping, and are determined by a (nonlinear, multi-degree of freedom) minimization of the correlation coefficient. The method is capable of detecting displacements with a resolution up to $1/8^{th}$ of a datum pixel[7], which implies capability of resolving strains on the order 0.03% for a 512x512 data pixel AFM image.

[7] When the noise levels can be minimized or almost eliminated.

2.4 Error Analysis for the Experimental Technique

There are several contributing sources of error in the experimental procedure: The first originates in the measurement of the load via the load cell. Provided the alignment of the specimens is accurate, the error in the measurement of the applied load and the calculation of the stress originates in the readings of the voltage recorder. The available instrument was capable of measuring 1 mV with accuracy two decimal digits accuracy. The uncertainty of the measured voltage was 5 μV regardless of the voltage amplitude which translates to 1/8000 N maximum error. The minimum recorded load at failure was about 0.025 N. Thus, the error in the measurement of load is at most 1/(8000*0.025)*100%= 0.5%.

The second source of error stems from the limited hardware resolution of the AFM. The radius of curvature of a new AFM tip is on the order of 10-15 nm, which after a number of scans becomes about 20 nm. The minimum sampling area is a disc with radius of 20 nm. In a measurement grid of 512x512 data points, the minimum area that can be reliably imaged is (20x512)x(20x512) =10x10 microns. This was also selected as the minimum AFM scan size in this work.

The accuracy of the AFM to track surface features depends on the shapes of the AFM tip and the sampled surface. If the polysilicon sample surface is modeled according to figure 1.5 by a sinusoidal profile, $y=A\sin(2\pi x/\lambda)$, where A is the bump height and λ is the grain size, and the AFM cantilever tip is considered to have a rounded shape, then a study of the effects A and λ parameters can be performed.

First, the tip must be sharp enough to reach any point on the surface of the film, i.e., the slope of the tip should be smaller than the maximum slope observed on the specimen. Thus:

$$\frac{dy}{dx}=\frac{2\pi A}{\lambda}\cos(\frac{2\pi}{\lambda})\Rightarrow\left.\frac{dy}{dx}\right|_{\max}<\frac{2\pi A}{\lambda} \tag{2.2}$$

Second, the radius of curvature of the tip must be smaller than the local radius of curvature of the scanned surface. This implies that

$$-\frac{1}{R}=\frac{d^2y}{dx^2}=-\frac{4\pi^2 A}{\lambda^2}\sin(\frac{2\pi}{\lambda})\Rightarrow\frac{1}{R}>\frac{4\pi^2 A}{\lambda^2}\Rightarrow R<\frac{\lambda^2}{4\pi^2 A} \tag{2.3}$$

For the specimens tested in this work:

A = 30 nm (average peak-to-valley height)

λ = 300 nm (average grain size)

Thus, from (2.2) and (2.3):

$$\left.\frac{dy}{dx}\right|_{\max}<0.63\Rightarrow\theta<\frac{90°-32°}{2}\Rightarrow\theta<27° \quad (\theta \textit{ is the half angle})$$

$$R<75nm \tag{2.4}$$

The limits in (2.4) provide the tip geometry requirements for appropriate imaging of the surfaces involved in this work and are satisfied by the used tips. Figure 2.11 illustrates an AFM data sampling along a scan line. The z-axis has been amplified for viewing purposes. The shallow and long grooves satisfy the requirements in the relations (2.4).

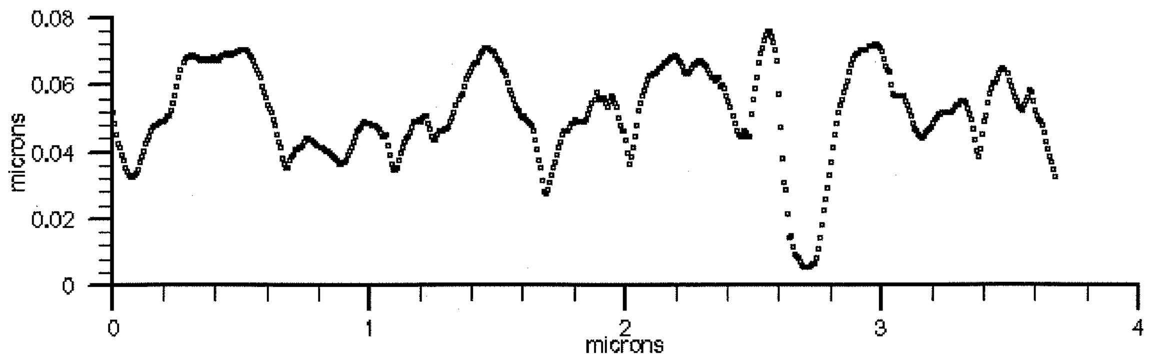

Figure 2.11 AFM data sampling along a scan line on polysilicon surface.

On the other hand, the data obtained via AFM are not fully repeatable. Noise and other errors originating in the performance of the piezoelectric tube add a combined error of about half pixel. Another source of error is the performance of the inchworm actuator, when the latter is used to estimate the total displacement. In this case, the resolution of the input is 4 nm; in other words, one step of the actuator. The minimum step in motion was between 200-400 nm, which implies an error of 1%-2% in the readings of the actuator.

The aforementioned errors in measurement are in all cases smaller than the data scatter, which is more than 5%. Thus their contribution is included in the scatter of the data but does not fully explain them.

2.5 Microtensile Tests of Polysilicon Specimens

The initial stage of this work was part of a "Round-Robin" experimental determination of physical properties of polysilicon specimens at the micron scale [11]. Because of the considerable uncertainties in the reported physical properties, the objective was to perform a comparative study of elastic modulus and failure strength measurements of polysilicon specimens by means of different experimental methods. Other participants in this effort were W. N. Sharpe [Johns Hopkins University], S. Brown [Failure Analysis Associates] and G. C Johnson [U.C. Berkeley]. The specimens were all manufactured in MUMPs21 run by MCNC and all dies were placed in adjacent positions on the wafer.

2.5.1 Calculation of the Elastic Modulus Based on Compliance Measurements

Tests were performed by making use of the system-specimen compliance technique and by using both the electrostatic and the UV adhesive grip. In graphs 2.12 and 2.13 the load vs. the total displacement for the specimen-test apparatus system and the load vs. the microtensile tester displacement curves are shown. The displacement is measured by the total travel of the inchworm that has been calibrated using the AFM. The periodic "knots" seen on the graphs are due to the operation of the piezoelectric clamps inside the inchworm actuator. For every 2.5 microns of travel the actuator switches internally to a new piezoelectric clamp that results in a small shaking effect. The effect of these jumps in the overall curve is, however, minimal. The system stiffness was measured at the end of the test and was found to be mostly the stiffness of the load cell with the contribution of the remaining parts of the apparatus being negligible.

Both the electrostatic and the UV adhesive based gripper were used in the tests. The voltage used to test the structures by the electrostatic grip was 70-90 Volts. Higher voltages produced sparks and caused damage to the specimens. These values depend on the thickness of the dielectric deposited on the electrostatic gripper. For low applied voltages the linear behavior seen in 2.12 is modified by a slip-stick effect between the grip and the paddle. These slips allowed the derivation of the friction coefficient which was found to be about $\mu = 0.1$. The static friction coefficient was calculated using equation (2.1) for the maximum load under which slip occurred. In this derivation, the total surface area excluded the area of the release holes on the paddle.

High voltages gave stable behavior until total displacement of 10 μm when complete slip occurred and the ultimate strength of the film could not be measured. This problem was overcome by employing the UV adhesive grip.

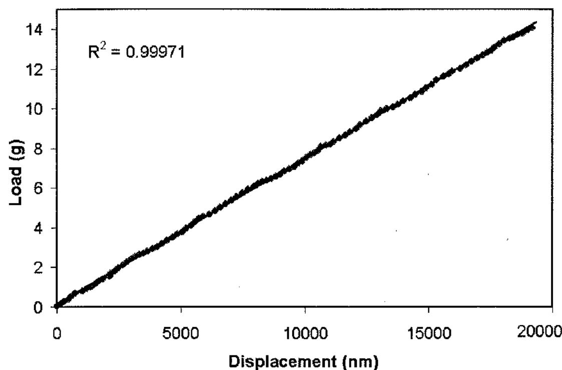

Figure 2.12 Load *vs.* total elongation of the specimen and the test apparatus.

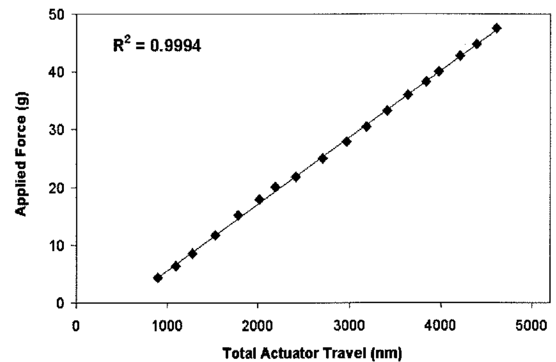

Figure 2.13 Load *vs.* elongation of the test apparatus.

The test results were evaluated using ABAQUS to model the specimen geometry and the boundary conditions. A plane stress model of a linearly elastic homogenous and isotropic material was used. Special consideration was given to other details of the specimen configuration such as undercuts and exact grip location. The experimental data,

in conjunction with the finite element analysis to model the specimen geometry, provided a value of the elastic modulus as 165.7±4.7 GPa, the value for the fracture strength as 1.00±0.1 GPa, where 0.1 GPa is one standard deviation of the nominal tensile strength, and a maximum tensile strain as 0.65%. The difference in the strength values reported in this work was probably the result of the different etch times that weakened the specimen structure as it will be discussed in detail in Chapter 4.

The operation of the electrostatic tensile tester provided an additional measurement. Based on the measured force values, for which relative slip between the grip and the paddle occurred, the static friction coefficient was calculated. The friction coefficient ranges from 0.07-0.1 with an average of 0.08. The scatter is attributed to the variation of the surface roughness.

Table 2.3 Round Robin results (MUMPs21)

	U.C. Berkeley *Static* *Bending Test*	*F. A.A.* *Resonant* *Frequency* *(Bending)*	*Johns* *Hopkins U.* *Tensile Test*	*Caltech* *Tensile Test*
Film thickness (μm)	2	2	1.5 / 3.5	1.915
Etch time (minutes)	9	2.5	9	13.5
Young's modulus (GPa)	**174**	**137**	**136/142**	**165.7±4.7**
Failure Strength (GPa)	**2.8**	**2.7**	**1.3**	**1.0±0.1**

As expected, the fracture was brittle and in most of the cases occurred near the ends of the test section (figure 2.14) as indicated by the finite element analysis of the specimen geometry shown in figures 2.15 and 2.16. The tensile stress assumes its highest value at the circled points (figure 2.16), differing by 4% from the central portion of the specimen. It is significant in the context of later discussion to mention at this point that specimens exposed to HF for times longer than 15 minutes demonstrated fracture at random locations in the test section, indicating that the HF induced roughness in the form of scattered micronotches or other flaws created random sites for fracture initiation.

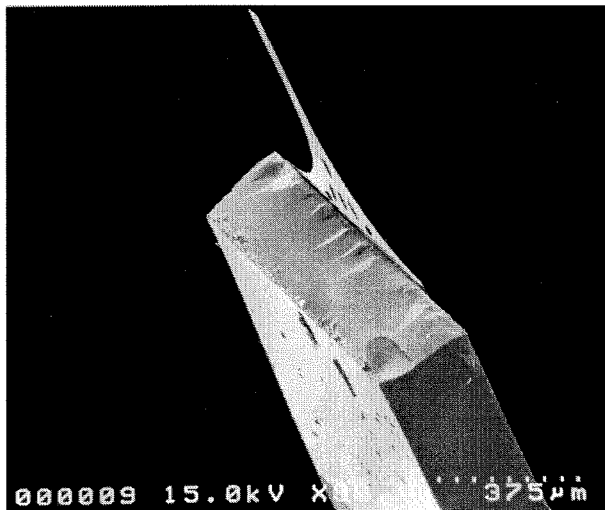

Figure 2.14 Fractured tensile specimen attached to the glass grip.

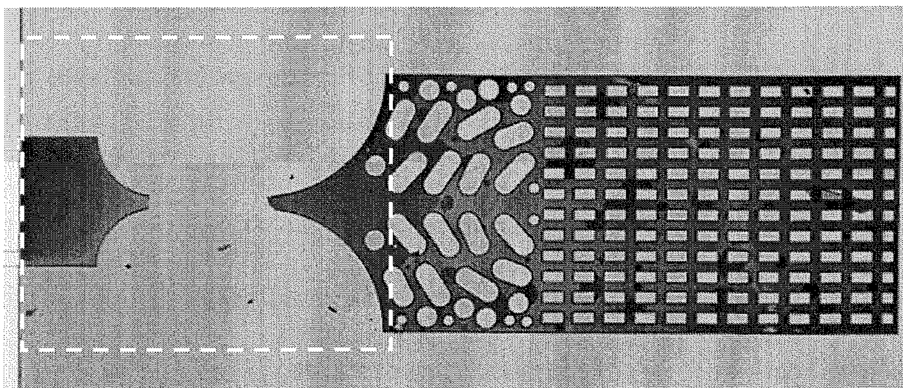

Figure 2.15 Fractured specimen indicating dynamic failure in the gage section. The area marked by the dashed line is modeled via ABAQUS as seen in figure 2.16.

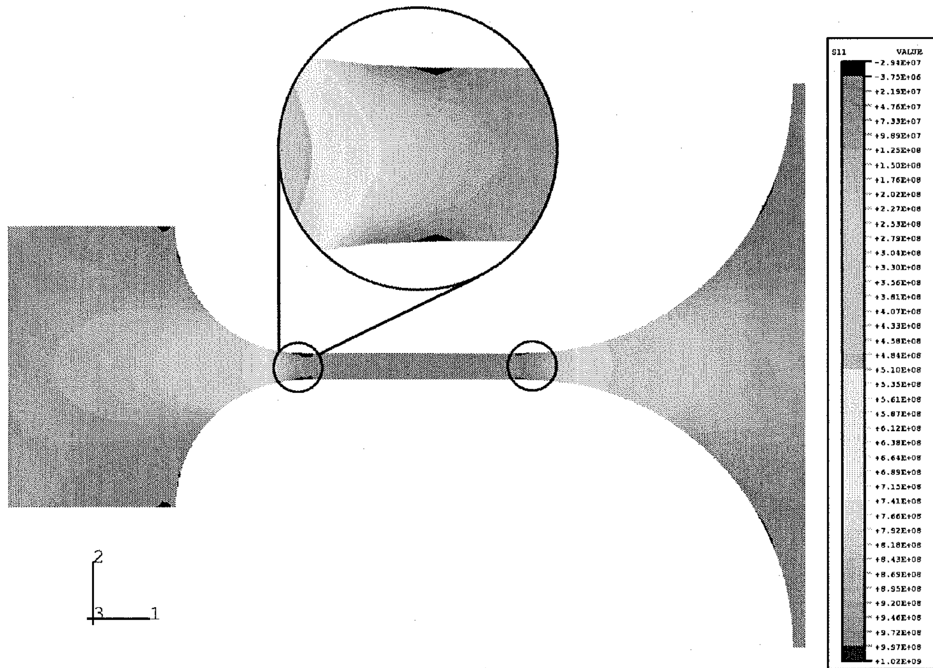

Figure 2.16 σ_{11} stress contours of the marked specimen area as calculated per ABAQUS. The circled areas mark stress concentrations with K=1.04.

The discrepancy in the modulus values, as determined by the four participants in the round robin effort, can be attributed in part to the differences in the experimental techniques employed. The assumptions and the boundary conditions involved in the case of bending and resonant structures used by two participants are more complicated in nature and result in larger uncertainties. On the other hand, the higher values of strength reported for bending and resonant frequency tests stem from the difference in the stress distribution in the specimens. When the specimens are subjected to tension, the total volume of the gage section is subject to the maximum stress (or the ultimate stress when failure occurs); on the other hand, when the specimens are subjected to bending tests, only a thin layer of the film is subject to the maximum stress. A probabilistic approach to

failure explains the higher "apparent strength" measured in bending tests compared to tensile tests. More insight in this problem will be given in Chapter 4.

2.5.2 Modulus Calculation Based on AFM Measurements

In addition to the aforementioned results obtained using the signal from the controller to the inchworm actuator, the displacements on the surface of the specimen are also measured using AFM records of deforming specimen configurations. As a demonstration of probe microscopy to determine strains locally, figure 2.17 illustrates an AFM record of the surface of the film at a deformed state during a load step of 0.06 N of axially applied load in the vertical direction of the figure. Point-to-point measurements provided a value of 155 GPa for the elastic constant, which agrees well with the modulus obtained using the inchworm indications (165±5 GPa).

An investigation of the error analysis for the DIC shows that the quality of the results depends on several parameters [28]. These include the identification of a necessarily large correlation domain, which is however sufficiently small from the point of view of strain resolution. The grain size relative to the correlation square is an important parameter that can be used as a guide to increase the speckle density in the area of study. In this work the AFM scan sizes were selected to be 10-20 μm square regions in order to satisfy the aforementioned considerations. Another consideration is the noise reduction to a degree that correlation errors are minimized and the efficiency of the method in detecting actual displacements is improved.

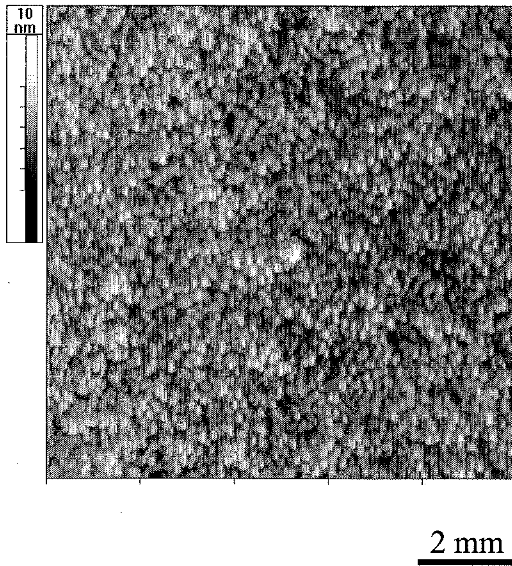

Figure 2.17 AFM recorded surface topography at applied load of 0.06 N.

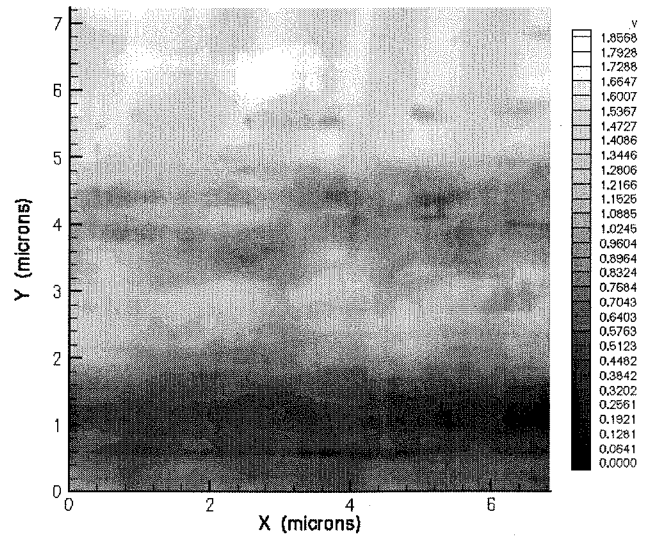

Figure 2.18 Displacement field for topography seen in 2.17.

Using the displacement field in figure 2.18 calculated *via* DIC and averaging over the entire area the value of Young's modulus was found to be 160 GPa. This value is very close to the experimentally obtained value using the compliance technique (165±5 GPa).

At this point it is important to delineate the importance and the potential of the new method that not only can measure the elastic constants directly on the film, but also it possesses the capability to monitor the deformation fields around notches and cracks and provide measurement of small displacements and at the same time sufficient information about the film microstructure (grain size, surface roughness) to correlate the measured properties with the physical condition of the test samples. This technique can be used to perform measurements in the vicinity of crack tips to resolve changes of the elastic strain energy during quasi-static crack propagation.

2.6 Specimen Characterization and Metrology

2.6.1. Specimen Microstructure and Surface Topography

The surface topography differs considerably between the "top" and the "bottom"[8] side of the specimens. The bottom surface is smoother with periodic well-shaped bumps (figure 2.19), while the top surface is considerably rougher (figure 2.20). As seen in the same figure, the sidewalls have periodic bumps of various dimensions similar to those observed at the bottom surface. These bumps are grains grown during the annealing process at the expense of the adjacent PSG material. The fractured cross-section of the specimens displayed a fairly columnar grain structure according to SEM images (figure 2.21). An average grain size of 300 nm with a Gaussian distribution from 200 nm to 400 nm was measured via AFM for MUMPs19 and MUMPs21. The bumps that are not overlapping in figure 2.22 are considered to be grains separated by grooves associated with grain boundaries. The ratio of the surface roughness to the specimen thickness is on the order of 1-2.5%, as calculated by measurements of the polysilicon film thickness variation using an AFM, This surface roughness has been identified as an important reason for the scatter of the strength measurements when fracture is assumed to initiate at surface defects [13].

The height of the surface bumps (figure 2.22) follows a Gaussian distribution with maximum probability 50 nm and 40 nm for MUMPs19 and MUMPs21, respectively. The minimum and maximum values of roughness are 30 nm and 80 nm for MUMPs19 and 25

---

[8] The bottom surface is the surface of the specimen opposite to the substrate and it is the first layer of deposited polysilicon, while the top side is the visible surface of the specimen which is deposited last in the manufacturing process

nm and 50 nm for MUMPs21. X-ray diffraction measurements have also revealed that LPCVD deposited films grow faster in the <110> crystallographic directions, displaying a columnar structure [13, 29].

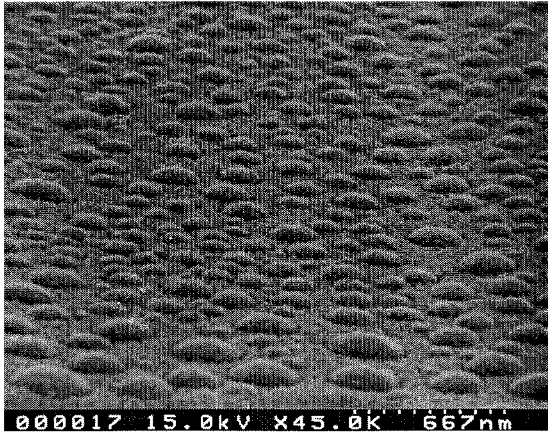

Figure 2.19 SEM picture of the bottom surface of the specimen (MUMPs35).

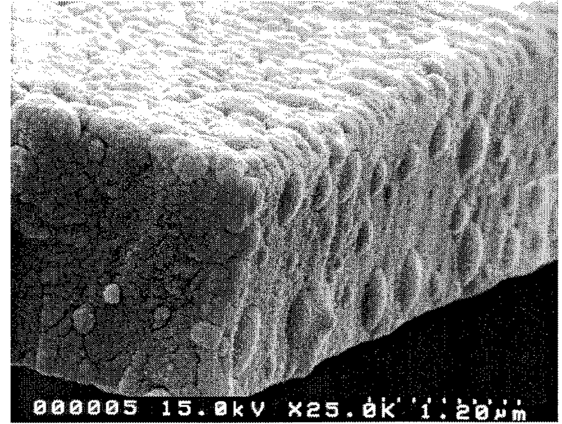

Figure 2.20 SEM picture of the top surface and the sidewalls of the specimen (MUMPs 35).

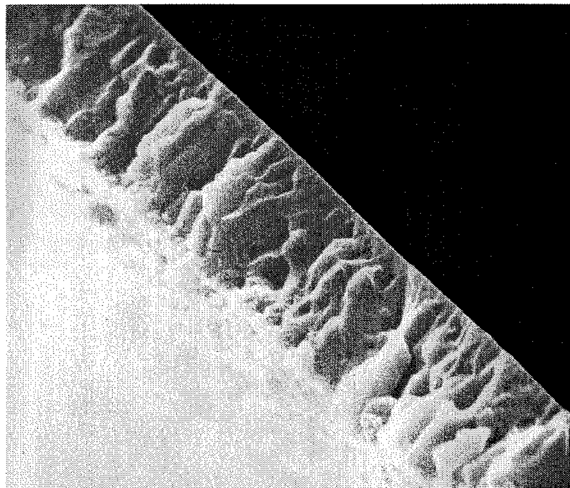

Figure 2.21 SEM picture of the fractured cross-section of the specimen. The columnar grain structure can be seen from the grooves and the extrusions in the fractured section. The specimens were manufactured in MUMPs19.

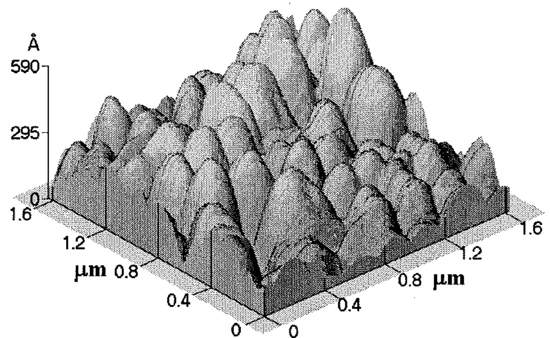

Figure 2.22 Three-dimensional rendering of the surface topography revealing the columnar structure of the material and the surface roughness. The z-direction is exaggerated compared to the lateral dimensions to make the grain structure more apparent.

Cross-sectional TEM performed via Focused Ion Beam (FIB) cuts on MUMPs specimens has also shown a fairly columnar structure as seen in figure 2.23. The crystallographic orientation of the grains, however, appears to be random.

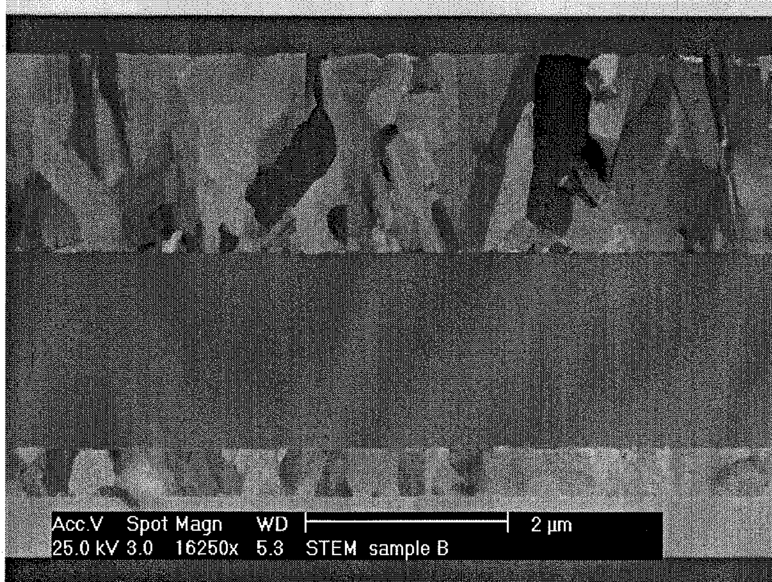

Figure 2.23 Grain structure and artificial coloration of MUMPs polysilicon according to the orientation obtained by TEM after focused ion beam sectioning. (Provided by Dr. Russell Lawton (JPL), after personal communication.)

X-ray diffraction analysis using an INEL© diffractometer has been performed on specimens from MUMPs21 to obtain the average diffraction pattern from a 1x1 mm area. The indexed diffraction pattern obtained with Co Kα radiation is shown in figure 2.24. A comparison with patterns available in the literature for randomly oriented polysilicon samples [30, 31] shows a strong qualitative resemblance including preservation of the random height of the diffraction peaks. Some of the diffraction peaks are absent from diagram 2.24 because of the crystal symmetry. The existence and intensity of the {110} and {100} peaks are determined by the presence of the fairly strong {220} and {200}

peaks. Although we tilted the sample over a large range of angles, no preferable texture was detected. Thus, although the texture is fairly columnar, as seen in 2.23 there is no strong preference of a specific texture in our specimens. It is important, however, to underline the limitations presented by the accuracy of the diffractometer and its capability to handle these small samples, as well as the average character of the measurement that included a total area of 2x2 mm.

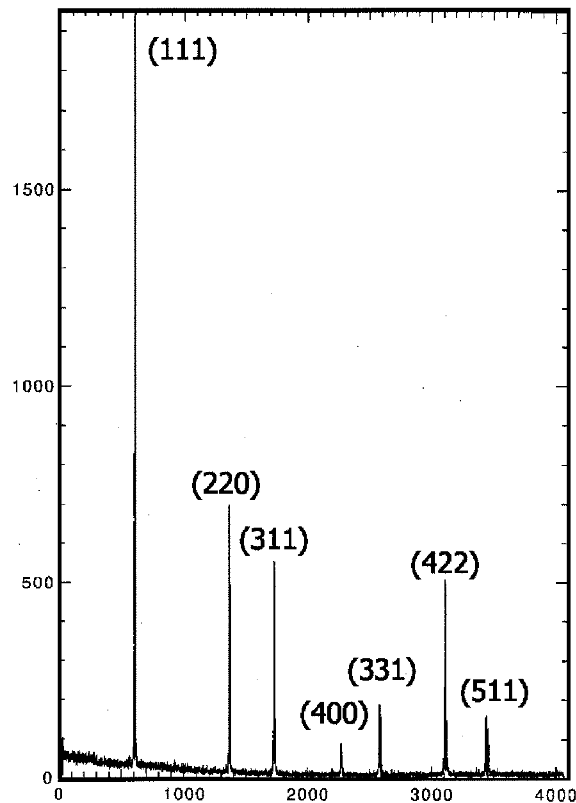

Figure 2.24 Diffraction pattern for MUMPs polysilicon obtained with Co K_{α}.

{110} is usually the texture associated with columnar structure in polysilicon [30]. Because the X-ray measurements sample the structure through he entire thickness of the film, the amount of other textures, i.e. {111}, in the upper regions is even less than

indicated by the diffractometer data. Much of the {111} texture must be located near the lower part of the film. In general, in silicon the {110} plane is the densest followed by {111} and {100} [30]. For lightly doped films deposited at 620 °C, annealing at 1100 °C causes a decrease of dominant {110} texture and an increase of {331} and {111} texture [30] as evidenced by the X-ray diffraction peaks in this work (see figure 2.25).

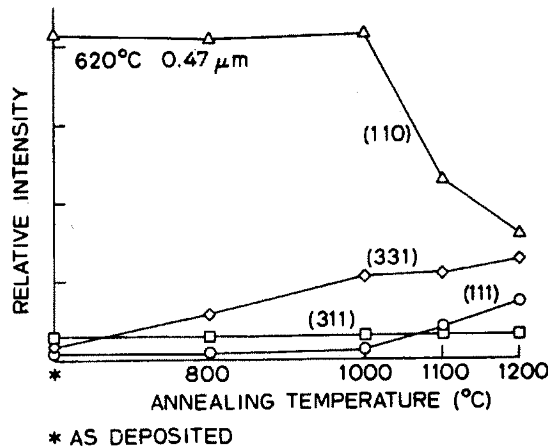

Figure 2.25 Effect of annealing temperature on grain texture [30].

2.6.2. Measurement of Specimen Thickness

The AFM is capable of providing images with atomic resolution. This assures that AFM measurements can also provide an accurate value of the film thickness, provided the latter is within the capability range of the microscope. The thickness that was measured with an AFM for MUMPs19 polysilicon was 1895 nm with a std. deviation of 50 nm, compared to the value given by MCNC (using a surface profilometer) of 1965 nm, with a std.

deviation of 48 nm. The AFM value agrees well also with that obtained by means of an SEM (1880 nm). The thickness that was measured for MUMPs21 for polysilicon was 1915 nm with a std. deviation 40 nm, compared to the MCNC given value of 1926 nm, with a std. deviation of 42 nm. The standard deviation corresponds to the surface roughness we have analyzed in a previous paragraph. The two independent measurements (by means of AFM and SEM) gave almost the same results that can be used to obtain more accurate values of the elastic constants than by using the nominal value (2.0 μm) for the film thickness. For example, using the nominal value of the thickness for the case of tensile test yields a 5% error, and translates into 12% for bending.

2.7 Discussion

A comparison of the acquired data using the new grip with the data obtained by the electrostatic method shows excellent linearity in the absence of slip steps. The UV curable glue technique makes also the use of AFM considerably easier. The absence of charges on the surface facilitates the operation of a probe microscope in the regime of very small interaction forces between the film and the AFM probe.

Our X-ray diffraction measurements revealed no preferential crystallographic in-plane texture. Therefore, the Young's modulus of an isotropic polycrystalline solid should be calculable by averaging the modulus value of all crystallographic directions on a specific plane [32]. Two models have been proposed: an isostrain, or Voigt [33] model, for the upper bound, and an isostress, or Reuss [34] model, for the lower bound, and the experimental value should lie within the Voigt-Reuss bounds. Using literature values

[35], for the stiffness constants, the modulus bounds are calculated (see Appendix 1) to be: 160<E<166 GPa. Our measurements agree well with this theoretical estimate.

The columnar structure of the film, in conjunction with the direction of the applied force (action in series), would tend to yield modulus values close to the lower bound. However, the existence of other textures in smaller percentage, such as {111} that is characterized by modulus invariance with respect to the crystallographic direction [35] and a value of 168.9 GPa, and the deviations from the columnar structure, can lead to measurements outside the aforementioned bounds. At the bottom of the film (see figure 2.23) the texture is not well defined yet and the grains are much smaller, so that for thin films the modulus value deviates from these values. The modulus of polysilicon for random orientation is 163 GPa [36]. Young's modulus is influenced by the interatomic distortions and it is not affected by the grain size of polycrystalline materials. But when the dimensions of the specimen are small in comparison to the grain size, the apparent properties are dominated by the grain orientations. In addition, the films under study were phosphorus-doped. Doping processes change the interatomic distance and thus the value of Young's modulus can be affected, but only by 1-2 %.

Accurate thickness measurements are important to evaluate mechanical properties. The uncertainty of the thickness of the film is increased by the fact that the surface displays roughness due to emerging grains. LPCVD deposition and lithographic methods inherently cause an uneven surface topography. Usually, this feature has not been taken into account when experimental results were evaluated. A (two-dimensional) finite element program (ABAQUS) has been exercised to investigate the influence of surface roughness as observed in the micro-manufactured specimens. A plane stress

model was used. The influence of two parameters was examined: The average bump height (wave amplitude) and the bump width (wavelength) for both tensile and bending tests. The roughness was modeled as sinusoidal surface variations, to simulate the real surface topography of the AFM data. Figures 2.26 and 2.27 show the effect of surface roughness on the data accuracy for tension and bending configurations. Clearly, this effect is stronger in the case of bending tests, reaching values of almost 10% for small grain diameters and high roughness amplitudes. Compared to figure 2.26, the effect for tension is almost a third of that for bending and rather minimal compared to other experimental errors (see paragraph 2.4). Taking into account figure 2.22 and using the plots 2.26 and 2.27, the error due to surface roughness for the tensile test is on the order of 1.5%, while for bending the error is almost 5%.

Thus, surface roughness represents a potentially important geometrical parameter to be considered when evaluating test data for determining the elastic modulus or the film strength precisely. The frequency and the amplitude of the surface undulations can have a particularly strong influence on data derived from bending inasmuch as surface roughness of relatively thin members will affect the bending rigidity more than the tension stiffness. In that case the roughness-induced errors can exceed the systematic errors.

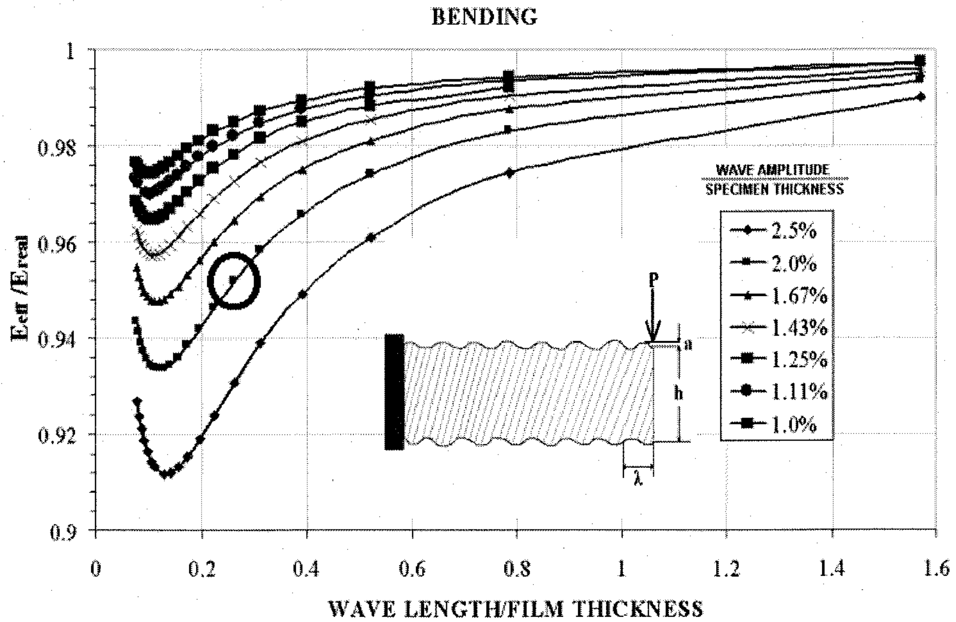

Figure 2.26 Ratio of the actual Young's Modulus to the effective (experimentally measured) value, E_{eff}/E_{real}, determined from a bending test, as a function of the wavelength and the amplitude of the surface roughness.

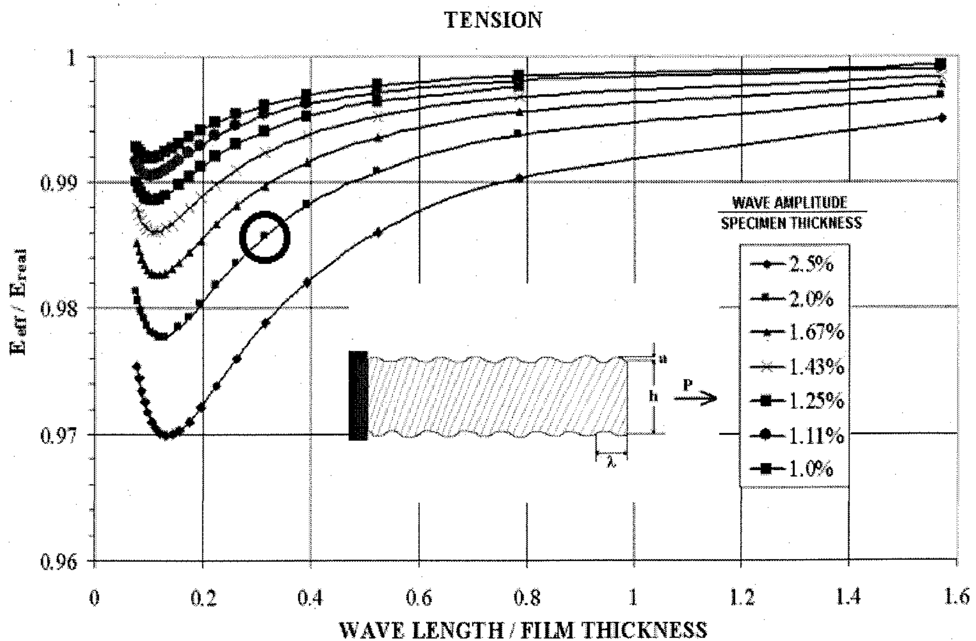

Figure 2.27 Ratio of the actual Young's Modulus to the effective (experimentally measured) value, E_{eff}/E_{real}, determined from a tensile test, as a function of the wavelength and the amplitude of the surface roughness.

In the FEM model of the specimen geometry the only assumed value in the modulus calculation was the Poisson's ratio, ν. The modulus value presented in table 2.3 was obtained using the experimentally available [21] Poisson's ratio value of ν=0.22. This value is also within the calculated Voigt-Reuss bounds (see Appendix 1). Theoretically, Poisson's ratio ranges [35] between $0.18<\nu<0.28$ for the most common crystallographic directions of polysilicon. For this broad range, the values of Young's modulus, as calculated by the FEM model, vary over the interval $165.65<E<165.8$ GPa. Thus, the influence of this parameter is minimal for our work.

The use of an AFM as a metrology tool needs to be improved and optimized further. Low frequency, large amplitude, lateral vibrations proved to be very important in the measurement of deformations along the axis perpendicular to the loading direction without measuring the value of the Poisson's ratio. Also, the sampling frequency of the AFM is limited to spatial resolution of 0.2% in strain, which, although it can be strongly enhanced by employing the DIC, it can be restrictive, especially when very narrow regions, such as grain boundaries, need to be imaged. Another limitation in the spatial resolution of the AFM is imposed by the radius of curvature of the AFM cantilever tip, which is on the order of 20 nm after the first use. This is the limiting parameter in resolution and can only be improved by use of new cantilever tips that have smaller radii of curvature or are made out of single or multiple wall carbon nanotubes. The latter can provide tips with radii of curvature on the order of a nanometer, but new considerations of the stability and durability of these tips are yet to be addressed.

CHAPTER 3

Influence of Scale on Strength

3.1 Introduction

Mechanical testing at micron and submicron scales possesses inherent difficulties associated with the available measurement techniques. In addition to the complexity presented by the available measurement equipment, the specimen dimensions, on the same order of magnitude as the material grain size, and the spatially statistical distribution of micro flaws in the structure, become important. Careful selection of the specimen geometry and size is critical to draw conclusions about the "tensile strength" of the material. At the macroscopic scale, since the pioneering work of Griffith on size effects in glass fibers[9] in 1921 [37], detailed work has shown that the scale effects are very important for brittle materials [38]. In the present work specimens, containing different and no perforations as well as various gage section dimensions, have been fabricated at MCNC, and at Sandia National Laboratories and were tested using the

---

[9] Before Griffith, Mariotte (1686) experimented with ropes of different dimensions made out of paper and tin, and he proposed the principle of "Inequality of the Matter whose absolute Resistance is less in one Plane than another."

microtensile tester described in Chapter 2. The goal was to investigate the existence of size effects in the measurement of mechanical strength for micron-sized specimens.

In the context of macroscopic design, notches and perforations play a fundamental role in assessing structural integrity. The associated variations in the stress and deformation fields (stress/strain concentrations) are well documented as part of the classical repertoire of failure initiation analysis. Commensurate with varying degrees of stress enhancement in the phenomenon of stress localization in domains that are governed by the smallest dimensions, namely the notch/perforation radius of curvature. Thus the classical notch theory offers itself naturally to investigate the relation of failure to size-scale by manipulating notch geometries so as to control the magnitude of stress locally as well as the domain size where the stresses are elevated.

In addition, the effects of small radii of curvature and stress concentration factors to failure were investigated. Because of limitations imposed by the microfabrication technique, the grain size in all samples was constant. To circumvent this problem, geometry induced stress concentrations facilitated the localization of stresses in very small volumes of the specimen. By testing specimens with the same geometry and appropriate perforation dimensions, size effects were investigated at even smaller length scales, which, essentially approach the grain size.

3.2 Tensile Tests of Perforated Micro-Specimens

The design of perforated tensile micro-specimens follows the general guidelines described in 2.2. Special consideration though, was given to the dimensions of the perforations and the gage sections since their combination will dictate the stress concentration at the internal notch tip. During the preliminary design of specimens the Neuber equations were used as a first approximation for the calculation of stresses, while a more detailed study was conducted later using approximate analytical solutions from literature and a finite element analysis.

3.2.1 Equations and Assumptions

The stresses around an elliptical notch in an infinite medium were derived first by Inglis [39] in 1913. Later, Neuber [40] derived full field solutions for a number of geometries and loading conditions that incorporate notches. These solutions were been employed in this work to design internally perforated tensile specimens. The material was assumed to be linearly elastic, homogenous and isotropic. The calculated values of stress are approximate since polycrystalline silicon is not a homogenous material at the micro-scale. Due to the columnar grain structure, the material is fairly isotropic only in the in-of-plane direction. In figure 3.1 the geometry and the important parameters are stated for an internal elliptical notch with stress concentration factor K. For the case of an infinitely large plate, the characteristic dimensions of the internal perforations are the radius of curvature, ρ, at the sharp notch tip and the long axis of the ellipse, t, or for a circular hole, the radius, r. Let the applied load away from the notch be P and the corresponding far

field stress p. The following derivations are based on the geometrical description in figure 3.1.

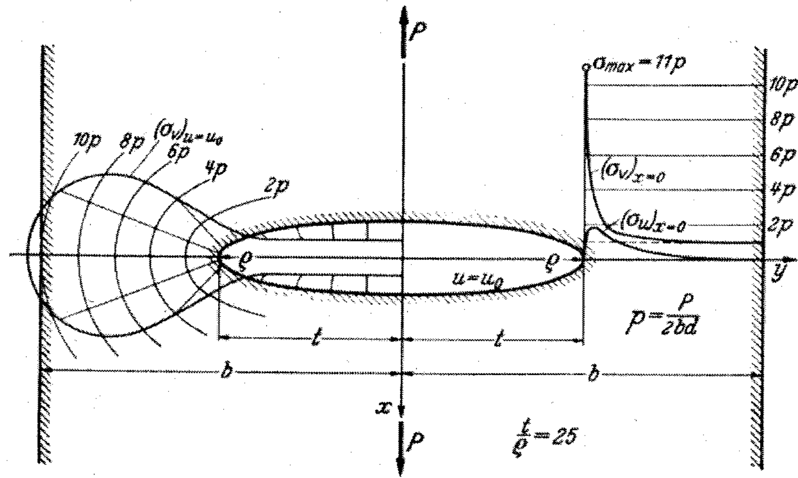

Figure 3.1 Geometry of an internal elliptical notch and stress distributions for K=11 [40].

For the problem described in figure 3.1, the solution is given in elliptical coordinates, with normal stresses σ_u and σ_v, in u and v directions respectively. The stress function in elliptical coordinates is as follows:

$$F=\frac{p}{8}\left\{\begin{array}{l}1+Cosh(2u)+2(-1-Cosh(2u_0)+2(1+e^{2u_0})e^{-u}Sinh(u)+\\ \left[-Cosh(2u)-1+2(\frac{1}{2}e^{2u_0}+\frac{3}{4}-\frac{1}{4}e^{4u_0})e^{-2u}+2(1+e^{2u_0})e^{-u}Sinh(u)\right]\cos(v)\end{array}\right\} \tag{3.1}$$

The stresses can be calculated in elliptical coordinates from the stress function, F, by

$$\sigma_u=\frac{1}{h}\frac{\partial}{\partial v}\left(\frac{1}{h}\frac{\partial F}{\partial v}\right)+\frac{1}{h^3}\frac{\partial h}{\partial u}\frac{\partial F}{\partial u} \tag{3.2}$$

$$\sigma_v = \frac{1}{h}\frac{\partial}{\partial u}\left(\frac{1}{h}\frac{\partial F}{\partial u}\right) + \frac{1}{h^3}\frac{\partial h}{\partial v}\frac{\partial F}{\partial v} \tag{3.3}$$

$$\tau_{uv} = -\frac{1}{h}\frac{\partial}{\partial u}\left(\frac{1}{h}\frac{\partial F}{\partial v}\right) + \frac{1}{h^3}\frac{\partial h}{\partial v}\frac{\partial F}{\partial u} \tag{3.4}$$

From the previous equations the tangential stress, σ_v, along the y-axis is

$$(\sigma_v)_{v=\frac{\pi}{2}} = p + \frac{p}{2}\frac{\cosh(u_o)}{\sinh(u)}\left[e^{u_o}\left(e^{2u_o} - 3\right)\left(1 + \frac{1}{2}\coth(u)\right)e^{-2u} + \cosh(u_o)\coth(u)\right] \tag{3.5}$$

where

$$u_0 = arc\coth\left(\sqrt{\frac{t}{\rho}}\right) \tag{3.6}$$

$$y = \sqrt{t^2 - b^2}\cosh(u)\sin\left(\frac{\pi}{2}\right) \tag{3.7}$$

b = short axis of the ellipse

u_o = constant that designates the elliptical boundary in elliptical coordinates

From equation (3.5) for $u=u_o$ the stress at the root of the ellipse is as follows:

$$(\sigma_v)_{u=uo,v=\frac{\pi}{2}} = \sigma_{\max} = p(1 + 2\coth(u_0)) = p\left(1 + 2\sqrt{\frac{t}{\rho}}\right) \tag{3.8}$$

Equation (3.8) is the well-known formula for the stress in a infinite, centrally and elliptically perforated plate under tension p normal to ellipse long axis.

For specimens with a circular hole, the tangential stress reduces to [41]

$$\sigma_\theta = \frac{p}{2}\left(1+\frac{a^2}{r^2}\right) - \frac{p}{2}\left(1+\frac{3a^4}{r^4}\right)\cos 2\theta \qquad (3.9)$$

where

σ_θ = circumferential stress

θ = angle with respect to the direction of the applied load

a = radius of the circular hole

r = distance from the center of the circular hole.

The amplitudes of the tangential stress, σ_v, and the maximum principal stress along the y-axis for the ellipse are shown in figure 3.2. The stress decreases rapidly away from the edge of the notch tip. Similarly, the maximum principal and the hoop stress, σ_θ, for a circular hole are plotted in figure 3.3. As one can see, the maximum stress and the tangential stress on the y-axis overlap. Thus, the tangential stress is responsible for failure along y if homogeneity is assumed.

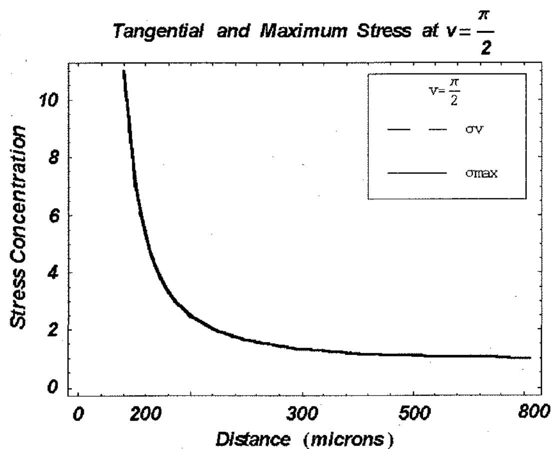

Figure 3.2 σ_v and σ_{max} along the y-axis for an elliptical notch with radius of curvature of ρ=8 microns and K=11.

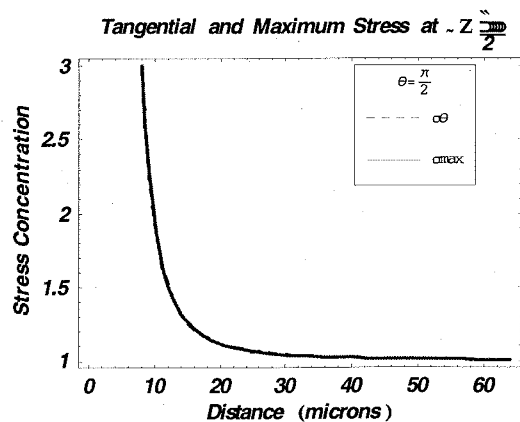

Figure 3.3 σ_θ and σ_{max} along the y-axis for a circular hole of ρ=8 microns and K=3.

Similar analyses to obtain a full field solution have been provided by studies on anisotropic and orthotropic composite materials. Tan [42] has derived approximate formulas for the orthotropic case based on Lekhniskii's work [43]. In the case of a finite strip, Tan derived finite width correction factors to correct the solution for the infinite plate.

3.2.2 Finite Width Correction Factors

The derivation of stresses described in paragraph 3.2.1 addresses infinitely dimensioned plates and applies well in the case of very wide specimens with small notches but not when the specimen dimensions are comparable to those of the notch. The presence of a straight edge near a notch causes an amplification of the stresses at the notch tip and thus the stress concentration has to be evaluated either numerically or analytically. In the present case approximate solutions for elliptically perforated finite plates exist in the literature. Isida [44, 45] conducted pioneer work in providing approximate analytical solutions for the stress field in the case of elliptical notches in semi-infinite and finite plates.

An alternate approach is the use of scale factors to compute the stresses near the notch tip. The calculation of scale factors is based on the assumption that the stress field along the y-axis is similar in shape for both the finite and infinite plate and differs in magnitude only by an amplification factor, so that

$$\frac{K_{hole}^{\infty}}{K_{hole}^{finite}} = \frac{\sigma_{hole}^{\infty}(y,0)}{\sigma_{hole}^{finite}(y,0)} \tag{3.10}$$

The finite width correction factors for an isotropic case are not dependent on the material properties and therefore being determined for a number of materials they find general applicability.

Tan [46] has derived improved approximate finite width correction factors for orthotropic materials based on the solution for the infinite plate. Using the same concept, finite width correction factors were derived for the case of isotropic materials. For the case of the ellipse in an isotropic plate the finite width factor is as follows:

$$\frac{K_{ellipse}^{\infty}}{K_{ellipse}^{finite}} = \frac{\lambda^2}{(1-\lambda)^2} + \frac{(1-2\lambda)}{(1-\lambda)^2}\sqrt{1+(\lambda^2-1)(\frac{2t}{W}M)^2} - \frac{\lambda^2}{(1-\lambda)}(\frac{2t}{W}M)^2\left[1+(\lambda^2-1)(\frac{2t}{W}M)^2\right]^{-\frac{1}{2}} \tag{3.11}$$

where

$$\lambda = \frac{b}{t}$$

W = Width of specimen gage section

M = Magnification factor calculated for the isotropic case by deriving in the limiting case the Heywood formula for circular notch. It is given by

$$M^2 = \frac{\sqrt{1-8\left[\frac{3(1-\frac{2t}{W})}{2+(1-\frac{2t}{W})^3}-1\right]}-1}{2(\frac{2t}{W})^2} \tag{3.12}$$

In the case of a circular notch (λ=1) equation (3.11) becomes

$$\frac{K_{circle}^{\infty}}{K_{circle}^{finite}} = \frac{3(1-\frac{2t}{W})}{2+(1-\frac{2t}{W})^3} \qquad (3.13)$$

Equations (3.11)-(3.13) are used to obtain a more accurate value of the stress concentration factor for the specimens tested in this work.

It is important, however, to discuss the implication of assumption (3.10) in the derivation of the isotropic finite width factor. This assumption is not valid everywhere on the y-axis. A finite element calculation of the stress field in a finite strip with an elliptical perforation shows that near the strip edge the stress is lower than the far field stress (see also later figure 3.7). On the other hand, for a plate of infinite width the stress on the y-axis far from the notch tip is the same as the far field stress. This implies that for the finite width plate the stress at the edge as determined via (3.11), is always higher than the far field stress, which is, of course, not true. The reason for this discrepancy is that equations (3.11)-(3.13) were derived using a force balance at the reduced cross-section, which contains thus the error that the stress concentration factors, as calculated by (3.11) and (3.13), are lower than actual. This conclusion is also evident by the finite element model results presented in table 3.3.

3.2.3 Design of Perforated Micro-Tensile Specimens

The surface micromachining process at MCNC was used to fabricate uniaxial tensile specimens with elliptical and circular perforations. Equation 3.5 was initially used to design the specimens and to place the specimen sidewall far from the hole so that its effect on the estimated stress concentration factor would be minimal for most of the specimens. Because of the deteriorating effect of HF post-processing (see Chapter 4), large surfaces of polysilicon without etch holes had to be limited. The maximum HF exposure for this batch of specimens was 15 minutes. For wide specimens it was necessary to include etch holes in the gage section near the notch, which makes the data interpretation complicated. Thus, for some samples the notch had to be placed near the specimen sidewall. Neuber theory [40] and other analytical solutions [43] available in literature for this problem do not apply in the case of elliptical holes close to the specimen straight boundary. A more accurate approach is to use the approximate solutions by Isida and the equations derived with the finite width correction factors calculated by Tan. As will be described latter, a finite element solution was compared with the analytical derivations. The nominal dimensions of the specimens and the stress concentration factors, K, as calculated by equation (3.5) are shown in table 3.1.

Table 3.1 Nominal K and dimensions of tested perforated specimens

Nominal K from equation (3.5)	**Radius of Curvature ρ (μm)**	**ρ / d (Notch radius) / (Grain Size)**
3	1, 2, 3, 8	3,6,10,25
6	1, 2, 3, 8	3,6,10,25
8	1, 2, 3, 8	3,6,10,25

The stress concentration varied from K=3, for specimens with circular notches, to K=11, for specimens with elliptical notches. For this range of stress concentrations, the radius of curvature varied between ρ=1 to ρ=8 microns. Thus, the radii of curvature of the sharp notches varied from 3 up to 25 times the grain size. According to the specifications provided by MCNC [22] microfabrication limitations demanded the minimum feature size to be 2 microns. In this work, elliptical and circular holes with radii of curvature as small as 1 μm were, therefore, incorporated (figure 3.4). The different geometries of the internal notches used in this investigation are shown in figure 3.5.

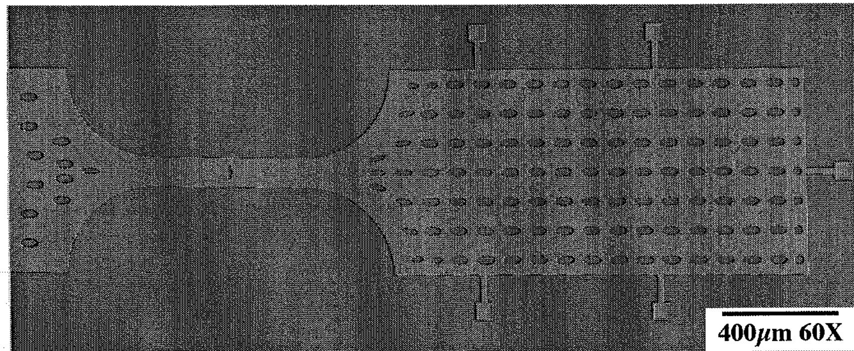

Figure 3.4 SEM micrograph of an elliptically perforated specimen

Although the specimen design included smooth curves in the notches, the photolithography mask design requires all curves to be ostensibly approximated by polygons. This implies that the actual dimensions of the fabricated structures may differ from the design values. However, the exact dimensions of the specimens were measured via SEM to image the specimen notches at various magnifications together with an AFM calibration standard (VLSI Standards Inc.) with pitch length of 5 microns, imaged as a reference at each magnification. The SEM imaging conditions, such as working distance

and beam angle, were kept constant during imaging of the samples and of the calibration standard. As seen in figure 3.5, the actual geometry of the specimens possesses spatial irregularities resulting from the limitations of the microfabrication technique.

The real dimensions of the microfabricated notches are listed in table 3.2. The accuracy of each measurement is within two pixels (one pixel at every end of any measured distance) and the spatial resolution is improved for the smaller perforations as shown in the last column of table 3.2. In almost all cases, the calculated radius of curvature based on the SEM measurements is higher than the design value while the difference between the two values is always much larger than the measurement error.

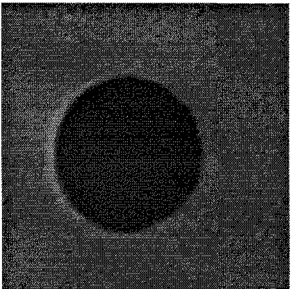

K = 3, ρ=1 µm

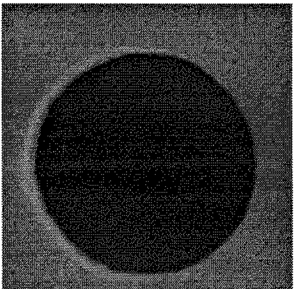

K = 3, ρ=2 µm

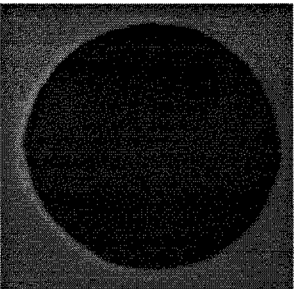

K = 3, ρ=3 µm

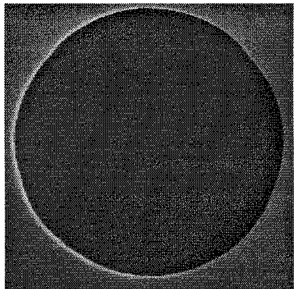

K = 3, ρ=8 µm

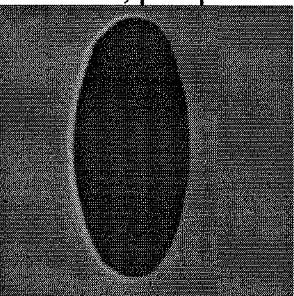

K = 6, ρ=1 µm

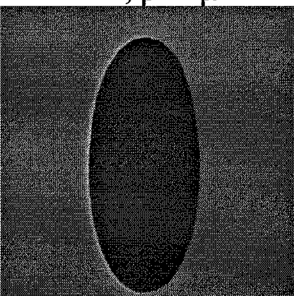

K = 6, ρ=2 µm

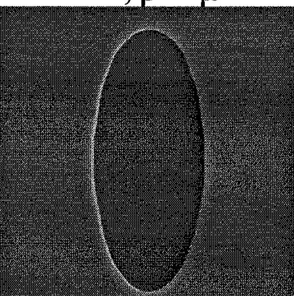

K = 6, ρ=3 µm

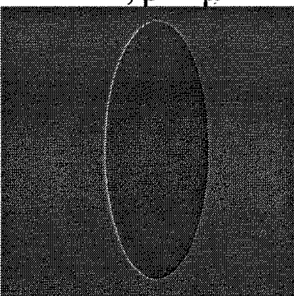

K = 6, ρ=8 µm

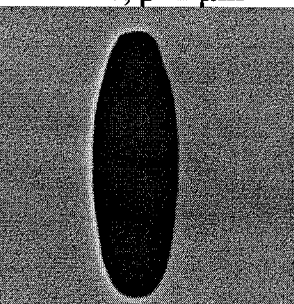

K = 8, ρ=1 µm

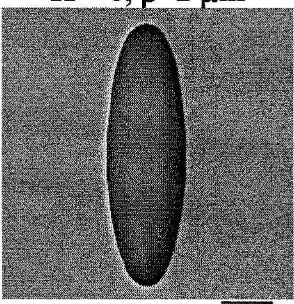

K = 8, ρ=2 µm

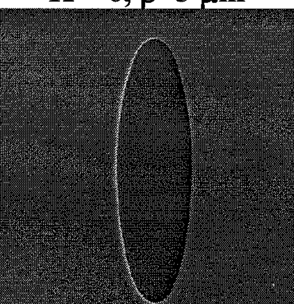

K = 8, ρ=3 µm

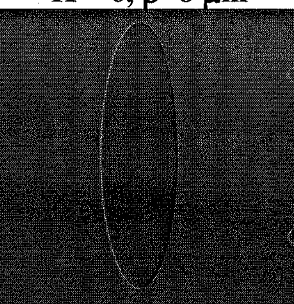

K = 8, ρ=8 µm

Figure 3.5 SEM micrographs of perforations with nominal K=3, 6, 8 as calculated by (3.5).

Table 3.2 Nominal vs. measured hole dimensions

Long Axis (microns)		*Short Axis (microns)*		*Radius of Curvature (microns)*		*Measurement Error (microns)*
Nominal	*Measured*	*Nominal*	*Measured*	*Nominal*	*Measured*	
2	2	2	2	1	0.98	0.015
4	4.1	4	4.2	2	2.17	0.01
6	6.3	6	6.4	3	3.23	0.015
16	16.3	16	16.25	8	8.12	0.03
12	11.6	5	5.4	1.04	1.25	0.03
24	23.2	7	7.5	1.02	1.22	0.05
24	23.7	10	10.4	2.08	2.30	0.05
36	35.7	15	15.7	3.13	3.44	0.08
48	47.3	14	14.6	2.04	2.24	0.1
72	71.2	20	20.6	2.78	2.98	0.61
100	99.6	40	40.2	8	8.13	0.22
196	195.2	56	56.2	8	8.1	0.44

3.2.4 Numerical Calculation of Stresses in a Finite, Perforated Plate

To take advantage of the highest precision in computing stress values, the test structures were modeled with the aid of ABAQUS to determine the stress concentrations. Six-node triangular elements were used to obtain the best approximation, while, due to the high density of elements near the notch, the use of three node triangular elements proved to be equally effective in describing the stress field. Compared to the quadratic elements, triangular elements provided better accuracy of the maximum stress concentration since the integration points were closer to the notch boundary. A very refined mesh in the area of interest has been used as shown in figure 3.6. The symmetry of the problem reduces the mesh to one quarter of the complete geometry. An iterative scheme has been used to place the load boundary condition sufficiently far from the notch so that the results were invariant with respect to the load position. Due to the existence of the edge near the notch, the tangential stress does not assume the far field value at the straight boundary. As seen in figure 3.7, the stress near the straight edge is smaller than the far field stress.

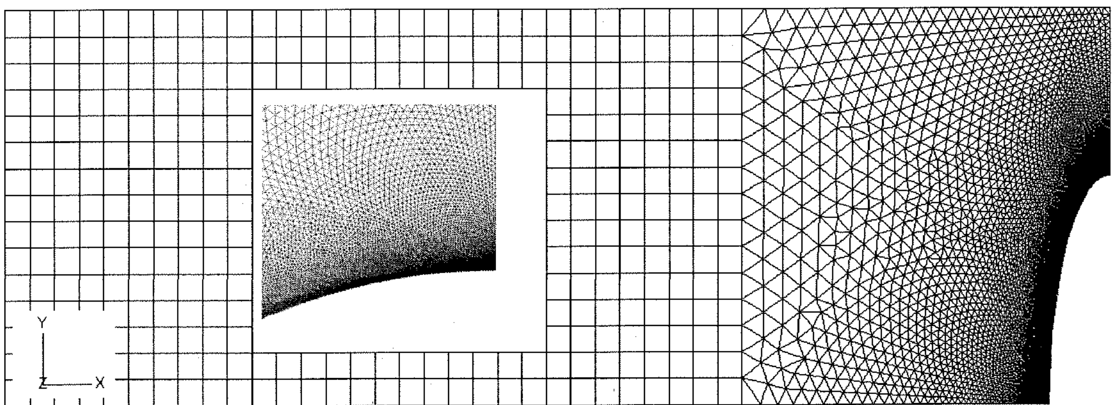

Figure 3.6 Representative mesh for the numerical calculation of the stress field around an elliptical notch in a finite plate. The inset illustrates the detailed mesh used in the region of the notch tip.

Figure 3.7 Numerically calculated σ_{11} stress for a specimen with nominal K=8, R=8.

3.2.5 Calculation of the Finite Width Correction Concentration Factor

The numerical and approximate analytical solutions were compared and used to obtain an estimate of the actual stress concentration at the notch tip. The approximate analytical solution for the stress concentration factor appears to be in most of the cases in excellent agreement with the value calculated by a finite element analysis except when the notch tip is very close to the specimen boundary (see table 3.3, 4th and 5th columns). The values of the finite width correction factors in the 5th column of table 3.3 are taken from a diagram of the finite width correction factors for isotropic materials in reference [47] as originally calculated by Isida [48]. The nominal specimen dimensions were used to derive K numerically, while the values of K listed in the last column of the table are calculated for the nominal and measured radius of curvature respectively. For high stress concentrations and small distances between the straight and the notch walls there is an

appreciable deviation from the numerical solution. The reason for this discrepancy is the assumption made in the derivation of the modified stress concentration factor, namely the whole stress field is proportional to that for the infinite strip. This assumption is valid near the notch tip but not close to the boundary where the stresses are lower than the far field stress (see figure 3.7).

Table 3.3 Stress concentration factors for the different perforations

Gage section (μm)	*Nominal ellipse axes (μm)*	*Calculated K from (3.5) (Nominal)ρ*	*Computed K using FEM (Nominal)ρ*	*Reference [47] (Nominal)ρ*	*Calculated K using [46] (Nominal/Real)ρ*
30	1/1	3	3.03	3	3.014/3.014
60	2/2	3	3.03	3	3.014/3.015
60	3/3	3	3.08	3.05	3.032/3.036
160	8/8	3	3.08	3.05	3.032/3.033
50	6/2.5	5.8	6.2	6.12	6.175/5.624
100	12/5	5.8	6.2	6.12	6.175/5.64
150	18/7.5	5.8	6.2	6.12	6.175/5.91
280	50/20	6	7	6.71	6.903/6.838
50	12/3.5	7.9	10.2	9.535	10.112/9.083
100	24/7	7.9	10.2	9.535	10.112/9.162
150	36/10	8.2	10.75	9.762	10.548/10.124
340	98/28	8	12	10.975	11.588/11.468

3.2.6 Results and Data Analysis

The specimens were subjected to uniaxial tension using the apparatus described in Chapter 2. The load was recorded at the time of failure to calculate the nominal stress far from the notch. The measured nominal far-field stress is then used to compute the local stress at the notch tip upon failure using the stress concentration factors determined via FEM. Since alignment of the specimens was accurate, the error in the measurement of the applied load and thus the calculation of the stress at the notch tip derives only from reading the oscilloscope. As described in paragraph 2.4, the error in the measurement of load was at most 0.5% for the minimum recorded load at failure. Thus, the uncertainty in the calculation of the failure stress due to measurement errors is at most 0.01 GPa for stresses that reach values of 2 GPa; this is very small relative to the experimental scatter.

Qualitatively, fracture always occurred at the notch tip and the cracks propagated in the same manner on both sides of the notch underlining the lack of bending or torsion. For the specimens with circular notches (figure 3.8, left) fracture assumed a "dynamic" character, after an initial crack propagation length, in which the crack propagated in a straight manner. Thus, as a result of crack branching, a wedge-shaped piece of material was fractured from each side of the notch. The dynamic character of failure must be attributed to the significant elastic energy stored in the specimens with circular notches. The elastic strain energy stored in these samples before failure is higher compared to that in the elliptically perforated samples because of the lower stress concentration of the circular notches. This fracture pattern has not been observed in the case of the elliptical notches that, as seen in figure 3.8, right, failed by crack propagation along a line.

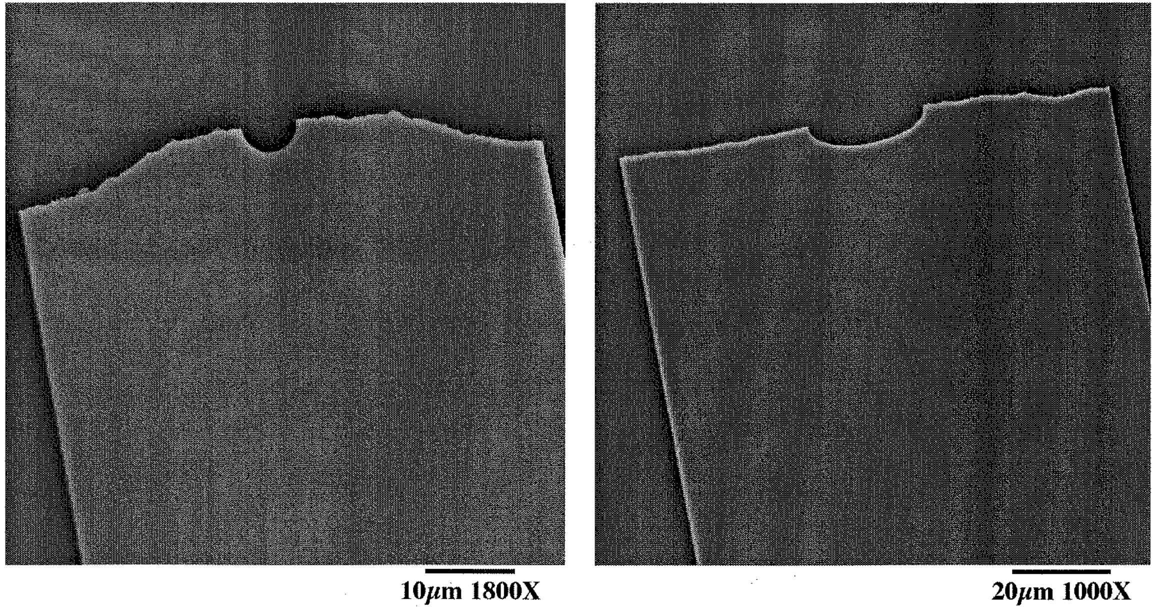

Figure 3.8 Fracture cross-section of specimens with circular (K=3) and elliptical (K=6) notches with ρ=2 μm.

The experimental results are presented in figures 3.9 and 3.10. The dashed line on each plot in figure 3.9 at stress of about 0.85 GPa represents the average value of the tensile strength as determined from non-notched specimens possessing a gage of 2x50x500 μm specimens. This "property" is referred to in the sequel as the "film strength". If the tensile strength were considered to be a material property, all experimental results of the calculated local stress at the notch tip should scatter around this value. For radii of curvature of 8 microns (and presumably larger) the local strength is close to the average values. For smaller radii of curvature the values of local strength increase relative to the film strength.

An alternative representation of the data is shown in figure 3.10. Here, it is seen clearly that the decrease in the radius of curvature results in a systematic increase in the local strength. This size effect is related to the localization of stresses in a gradually

smaller area as one moves from notches with large radius of curvature to those with small radii. The rationale for this phenomenon is demonstrated in figure 3.11 by the results from the FEM analysis. For specimens that had the same stress concentration (K=3), variable radii of curvature of ρ = 1, 2, 3, 8 microns result in the localization of the stresses in a gradually larger area. Failure in brittle materials occurs when a flaw (microcrack, defect) of a critical nature and located in the high stress region under a certain load. Since this region is larger for the specimens with notches of larger radius of curvature, the probability for critical flaws to exist is also higher and the local stress at failure is correspondingly lower. This behavior is also identified in our tests in figures 3.9 and 3.10.

Using approximate closed form solutions by Isida et al. [44], the stress gradient at the root of a circular notch in a finite width strip can be readily calculated. These values are shown in table 3.4. The gradient changes drastically as ρ changes from ρ=1 to ρ=8 μm. Using the average values of the measured failure stresses taken from figures 3.9 or 3.10, one can estimate the length scale needed so that the stresses will reach the value of the film strength. For notches with ρ =1 μm the stress reaches the "material strength" within a length of less than two grains while for ρ =8 μm a minimum length of 7 grains is needed.

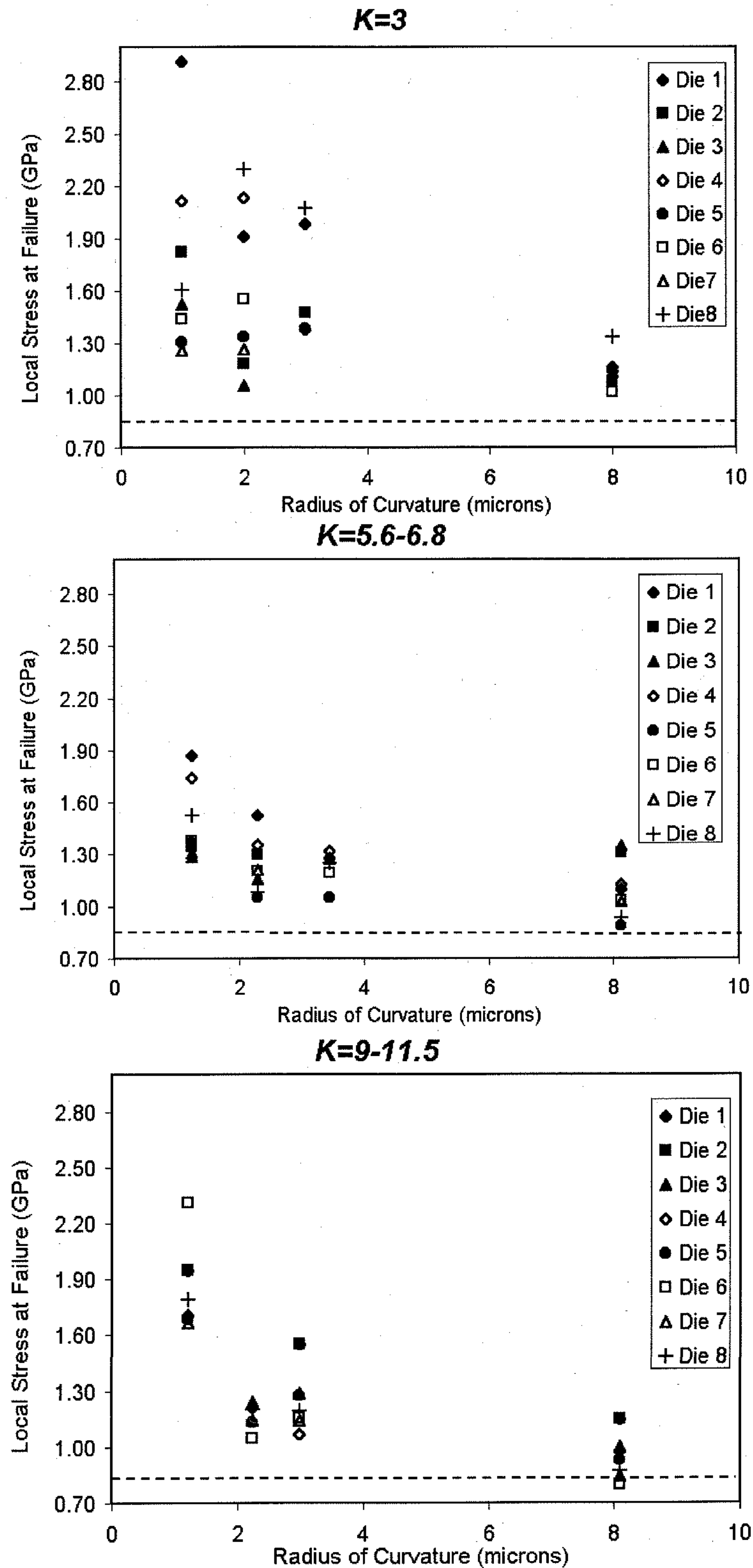

Figure 3.9 Experimental results of the local stress at failure at the tip of the notch for different stress concentrations. The dashed line shows the tensile strength.

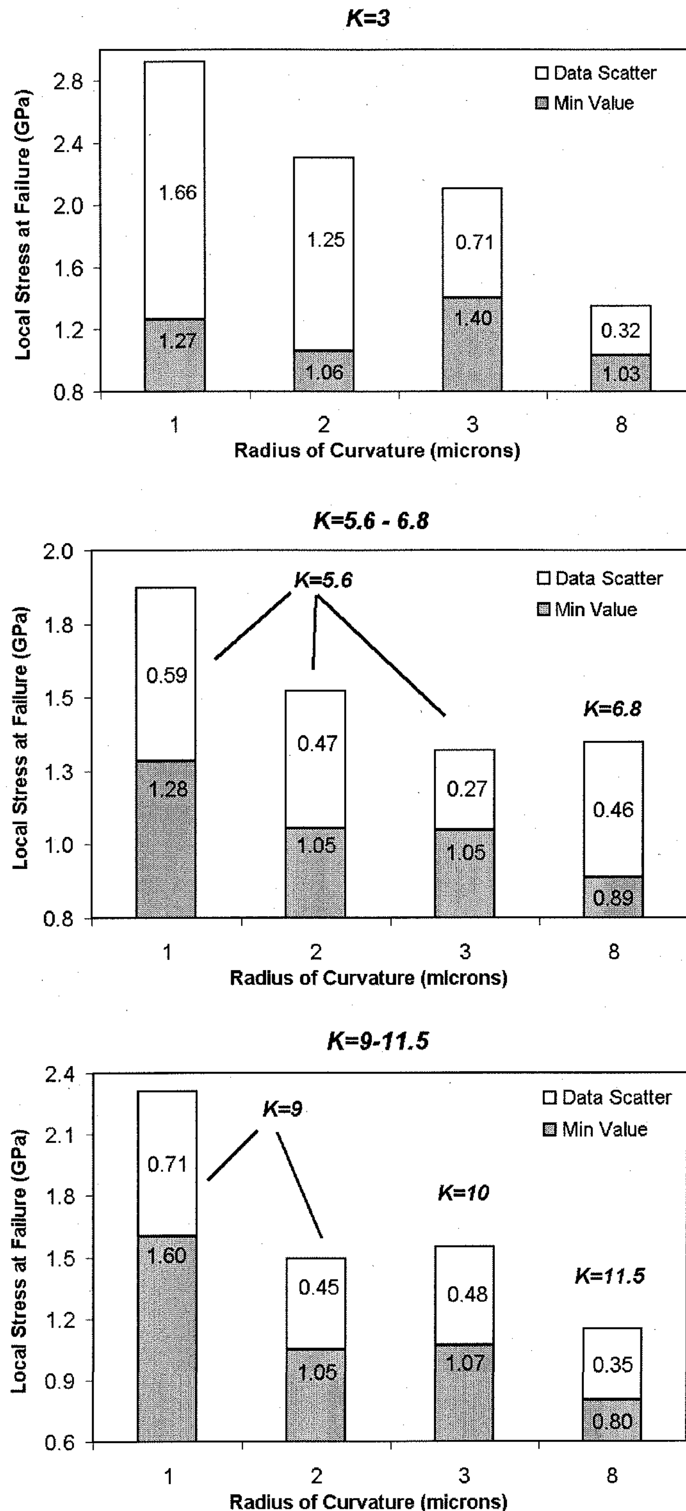

Figure 3.10 Local stress at failure for different stress concentrations. The gray bar indicates the minimum strength and the white bar, the scatter of the experimental data.

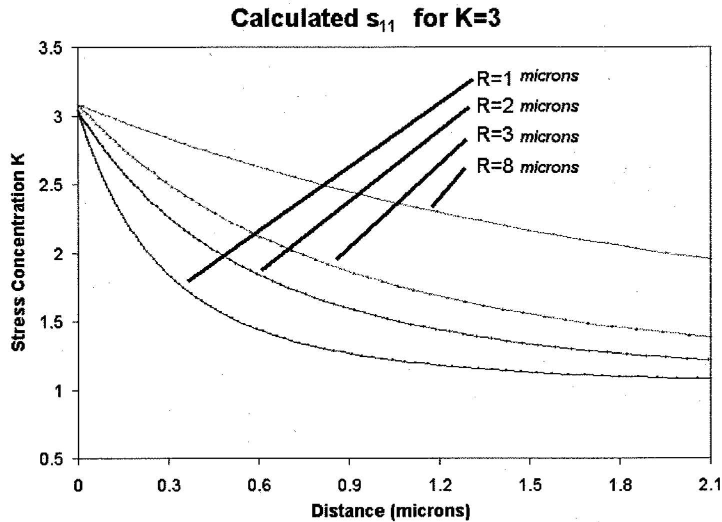

Figure 3.11 σ_{11} stress profile along the y-axis (according to figure 3.1) for constant K and different radii of curvature as calculated by the FEM model.

Table 3.4 Stress gradient at the notch root and decay length for K=3

Radius of notch (μm)	*Average failure stress at notch tip (GPa)*	*Stress gradient at y=ρ (GPa/μm)*	*Characteristic length for decay of stresses to σ_f*
1	1.76	-7.02	<2 grains
2	1.60	-3.51	3 grains
3	1.68	-2.34	5 grains
8	1.16	-0.88	7 grains

For the present test geometries, the important characteristic length that governs the stress field near the notch root is the radius of curvature, ρ, while away from the tip the length of the long axis of the ellipse, t, becomes important. In the proximity of the tip only the

local geometry is important, which is the radius of curvature, while the actual geometry of the perforation becomes important for the stress field only far from the notch tip. Then, the influence the ellipse's long axis becomes an important parameter for stress, but the latter has already assumed values considerably lower than the material strength. This is demonstrated in figure 3.12 where equation (3.5) is plotted for various K values. This observation is supported reasonably well by the data in figure 3.13. If the notch radius remains the same but the stress concentration changes, the plots tend to overlap although this is obscured by the large data scatter and the error associated with the measurement method.

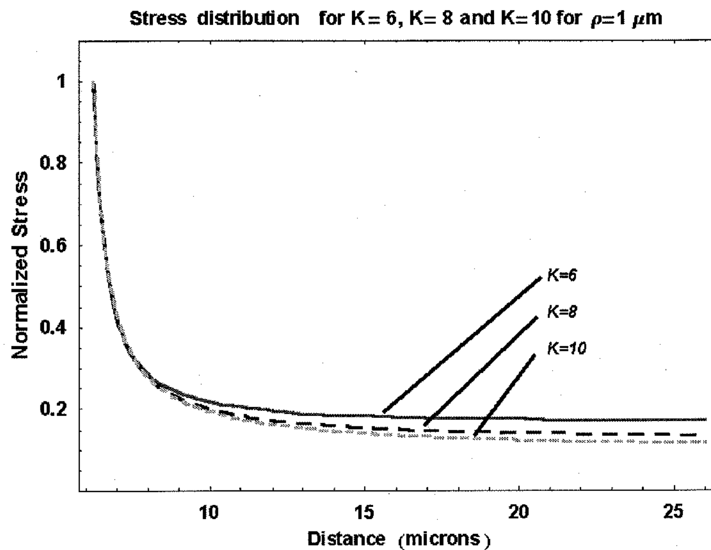

Figure 3.12 Tangential stress as computed by (3.5) for different K and same ρ.

The dominating influence of the notch radius, and the accompanying size of the high-stress region, is well summarized by the data in figure 3.13. There is a definitive dependence of the "strength" on the size scale. The local "strength" increases with smaller size scales by a factor of two or so. In addition to that, the scatter of the data increases with decreasing size scale. Although this scatter is considerable, a tentative

image emerges: The stress concentration plays a secondary role, if any, for size scales comparable to the grain size. The failure stresses resulting from small notch radii are larger, on average, by a factor of about two than those derived from the large scale (average) "property" measurements. Consequently the failure is governed (more or less) by the domain size where high stresses reign. The size-sensitive nature of "strength" makes the use of film strength a conservative approach.

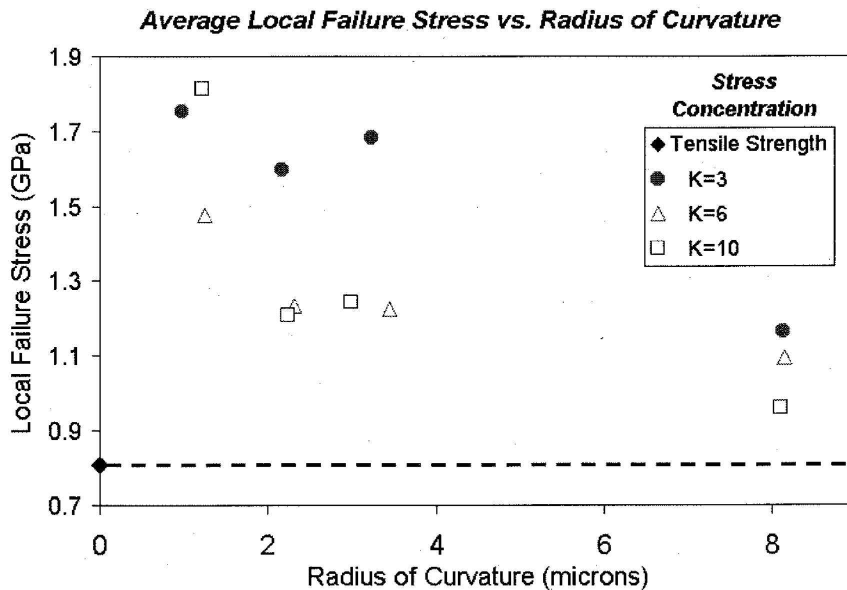

Figure 3.13 Experimental values of the average local failure stress as a function of the radius of curvature.

According to figure 3.13, at a radius of one to three microns, the failure data are not particularly ordered according to the stress concentration factor. On the other hand, once the notch radius attains large values on the order of eight to ten microns, figure 3.12 indicates that a difference in the stress level can become apparent for different stress concentration factors and, consequently, the failure data in figure 3.13 (see values at 10 microns) become ordered by the stress concentration factor for the largest notch radius.

In the previous investigation the material grain size was constant while the stressed geometry varied. One can gain more insight in the failure mechanisms at the sub-micron and nanometer scales if the grain size (and thus the underlying microstructure) is also a variable in the test. Moreover, as it will be discussed in detail in Chapter 4, the material condition can be important and affect the failure load measurements. Post processing can have pronounced consequences on the strength of the material affecting the grain boundaries of phosphorous-doped polysilicon. In the case of notches with large radius of curvature, the stresses are high in a large domain around the notch compared to the notches of the small radius. This large domain includes increased grain boundary area, which if it is affected by the exposure to HF will result to failure at lower loads compared to notches of smaller radii.

3.3 Specimen Size Effect

Most ceramic materials display a linear stress-strain behavior from zero strain to fracture. The lack of ductility or yielding capability leads to three characteristics for these materials [49]: (1) large data scatter, (2) low strain tolerance, (3) low fracture toughness. To account for the scatter in the data of fracture strength a probabilistic theory of the “weakest link” that uses the Weibull statistical distribution has been developed in the past. The applicability of the Weibull statistics is examined in the next paragraphs for micron-sized specimens.

3.3.1 Weibull Statistical Analysis of Failure

Mechanical strength displays volume dependence. For this reason a ceramic rod is stronger in bending than in simple tension. In tension the entire sample carries the tensile stress, while in bending only a thin layer close to the surface (thus a smaller volume) carries the peak stress.

The strength distribution of a set of specimens does not follow a Gaussian (normal) distribution, but failure is described by the widely used Weibull cumulative function. Weibull statistics are based on the "weakest link hypothesis" [50] which implies that the strength of a structure depends on the most important defect (flaw) in the material under the application of a specific load. It is not necessary that the largest flaw will cause catastrophic failure of the structure, but depends on the flaw orientation relative to the direction of the maximum failure stress. In Weibull statistics all samples are assumed to be subject to the same stress distribution. The Weibull failure probability distribution is given by

$$P = 1 - \exp\left(-V\left(\frac{\sigma - \sigma_u}{\sigma_0} \right)^m \right) \tag{3.14}$$

where

σ_u = threshold stress below which the failure probability is zero. Setting σ_u =0 results in an overestimate of the probability of failure.

σ_0 = scaling parameter. It is the stress that causes 63% ((1-1/e)*100%) of the specimens to fail.

m = the Weibull modulus. It provides the rate by which the strength falls, as the stress approaches σ_0 [51, 54]. The lower the value of m, the greater the

variability of strength and the higher the uncertainty that the material has a well defined and known failure stress.

The mean (strength) of the distribution is [50]

$$\bar{\sigma} = \sigma_u + \frac{\sigma_0 \Gamma\left(1 + \frac{1}{m}\right)}{V^{\frac{1}{m}}} \tag{3.15}$$

where

Γ = is the gamma function.

It is often quoted [50] that the mean strength of two components with different volumes are related by

$$\left(\frac{\bar{\sigma}_1 - \sigma_u}{\bar{\sigma}_2 - \sigma_u}\right) = \left(\frac{V_2}{V_1}\right)^{\frac{1}{m}} \tag{3.16}$$

which is a consequence of (3.15). However, the weakest link theory does not permit this conclusion: It only indicates that the modulus of fracture will be directly related to the volume.

If we know the failure probability from experiments on specimens with volume V_0, we can calculate the probability for volume V:

$$P_s(V) = \exp\left(-\frac{V}{V_0}\left(\frac{\sigma}{\sigma_0}\right)^m\right) \tag{3.17}$$

The failure probability P_j is computed for the jth specimen of a sample of n specimens using appropriate probability estimators. Those that give the least biased Weibull modulus, m, are [50]

$$P_j = \frac{j - \frac{1}{2}}{n} \qquad n \geq 20 \tag{3.18}$$

$$P_j = \frac{j - \frac{3}{8}}{n + \frac{1}{4}} \qquad n \leq 20 \tag{3.19}$$

These estimators have been validated for use with more and fewer than 20 specimens experimentally [52] and numerically [50].

3.3.2 Specimen Design and Testing

Non-perforated specimens with different dimensions were provided by Sandia National Labs for a limited round robin – cross correlation study [53] of the mechanical properties of polysilicon. The dimensions of these specimens were nominally 20 or 6 microns wide and 250 or 1000 microns long, while the thickness of the specimens was 2.5 microns in all cases. The measured dimensions of the specimens were provided by Sandia, and they were 19.8 and 5.8 microns in the width, while the thickness was very accurately controlled at 2.5 microns. Optical microscopy images of the specimens are shown in

figure 3.14. The indicated dimensions are the nominal length and the width of the gage section respectively. The specimens were tested in tension using the apparatus described in Chapter 2 with more than 95% success rate. The results from six dies (four different specimens on each) are shown in table 3.5:

The average Young's modulus for all experiments and all specimen sizes was 165.4±6.9 GPa, where 6.9 GPa is one standard deviation. This value agrees very well with the value obtained for MUMPs21 specimens (165±5 GPa). This was expected, since the modulus of elasticity is a material property and basically depends on atomic interactions only. The average tensile strength, however, is about 3 GPa, i.e., three times higher than the strength measured from specimens manufactured at MCNC. This can be attributed to the different processing conditions between the two microfabrication facilities. More insight in this difference in strength will be given in Chapter 4. The results of this table are plotted in figures 3.15-3.16. The values of the Young's modulus do not demonstrate any significant difference that can be correlated with the specimen size.

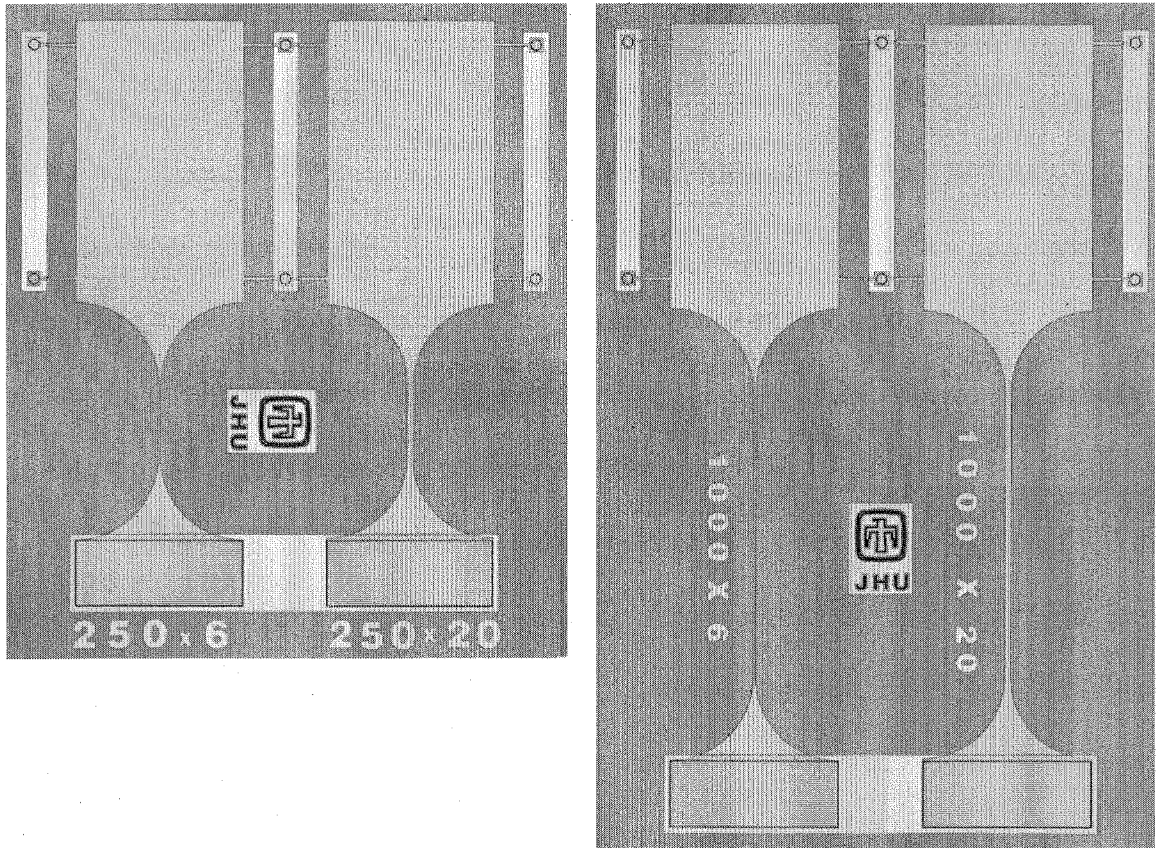

Figure 3.14 Optical microscope images of tensile specimens manufactured by Sandia National Labs. The indicated dimensions are the Length x Width of the gage section.

Table 3.5 Nominal dimensions and properties of tested samples

Specimen Width (μm)	*Specimen Length (μm)*	*Average Tensile Strength (GPa)*	*Stand. Deviation (GPa)*	*Young's Modulus (GPa)*	*Deviation (GPa)*
6	250	3.25	0.85	172.5	17.6
6	1000	2.88	0.58	169.4	6.9
20	250	3.47	0.17	162.4	6.3
20	1000	2.94	0.35	168.8	10.3

Although the results in table 3.5 demonstrate considerable scatter, agree very well with those obtained by Tsuchiya [53]. In that work the tensile tests were performed in an SEM chamber using the electrostatic technique. The comparison is shown in table 3.6. Tsuchiya's measurements were performed in the absence of oxygen in an SEM chamber, which, in conjunction with his large number of samples, justify the lower standard deviation of his data compared to the results of the present work.

On the other hand, there is no clear evidence of a size effect with regard to the mechanical strength of the specimens. The large scatter of the data does not permit any immediate conclusions. However, if one plots the data as shown in figure 3.17, however, a certain trend can be established. The average value of the "tensile strength" depends on the gage length of the specimens. Samples with the same length of 250 μm or 1000 μm and different widths demonstrated similar average strength. As it will be shown in the next section, this conclusion can also be established by a Weibull analysis.

Table 3.6 Cross comparison of experimental results

Length (μm)	*Width (μm)*	*Present Work*			*Tsuchiya*		
		N	*Mean*	*SD*	*N*	*Mean*	*SD*
250	5.8	5	3.26	0.58	9	3.27	0.24
250	19.8	5	3.47	0.20	10	3.37	0.17
1000	5.8	6	2.87	0.36	14	2.97	0.24
1000	19.8	6	2.96	0.32	8	3.10	0.22

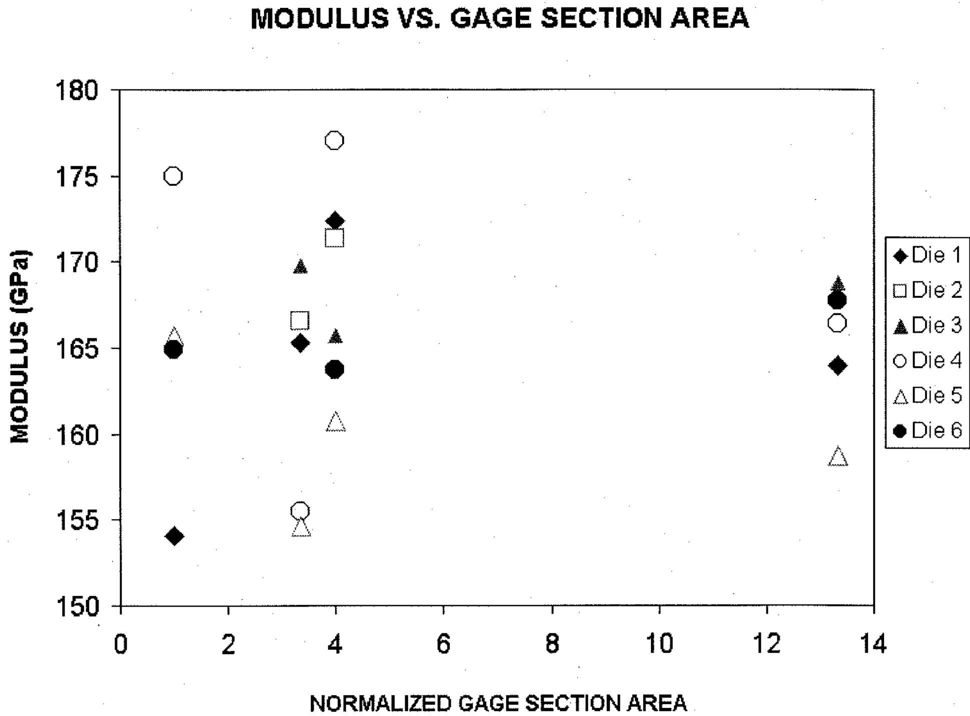

Figure 3.15 Young's modulus measured from specimens with various gage sections.

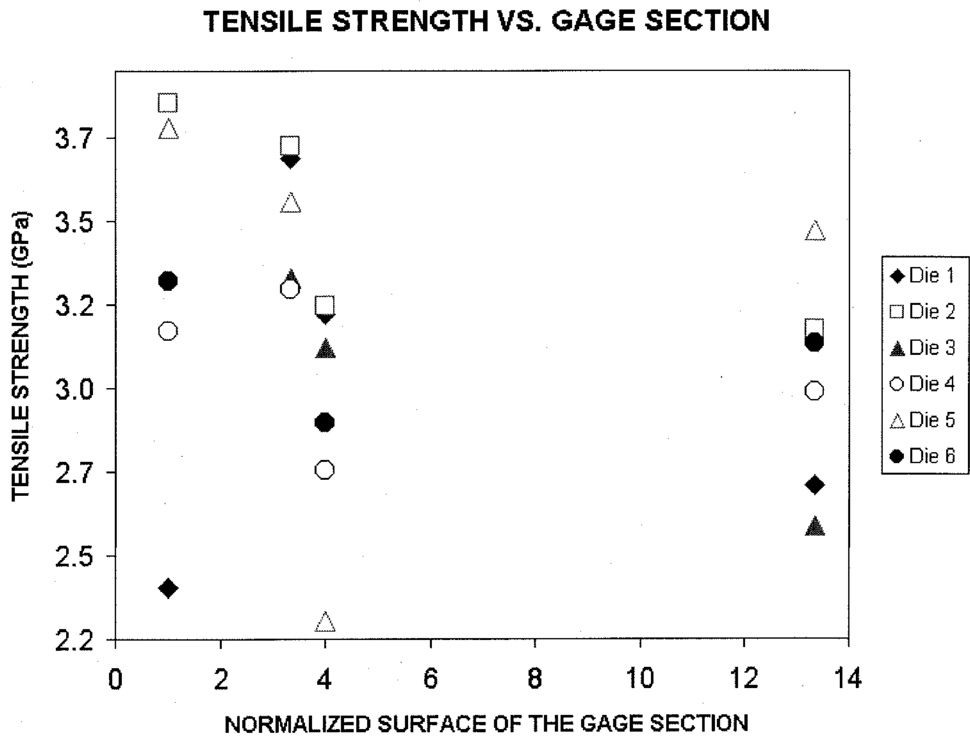

Figure 3.16 Tensile strength of microtensile specimens as a function of gage surface.

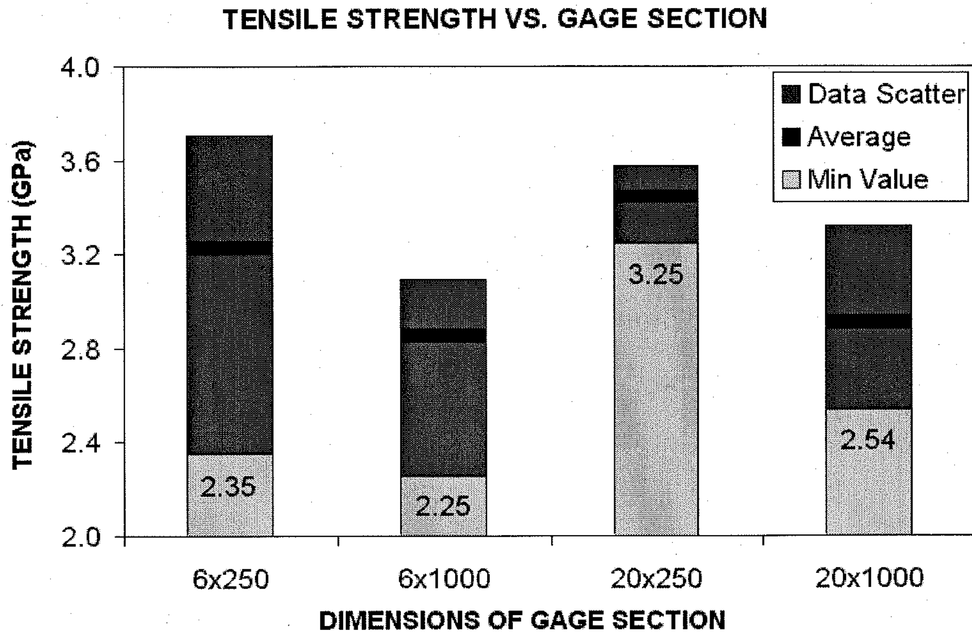

Figure 3.17 Bar chart of the tensile strength as a function of gage surface.

3.3.3 Failure Analysis

A study of the failure probability (equation 3.17) for every set of specimens of the same length[10] results in two distinctive curves (figure 3.18). Thus, the failure probability depends on the length of the specimens rather than the total surface area. If one calculates the scaling stress parameter, a striking result is obtained: This parameter is nearly the same for the specimens with the same length (see also figures 3.19 and 3.20). This is illustrated in table 3.7 by matching values of the scaling parameter for specimens of identical length. A statistical analysis of the data for all specimens of the same length provided a scaling parameter for specimens of 250 microns length of 3.574 GPa and for

---

[10] The probability parameters depend on the specimen size.

specimens with 1000 microns length a scaling stress of 3.062 GPa. These values agree very well with the data in table 3.7. It must be noted, however, that the limited number of data it is not really sufficient to draw firm and general conclusions.

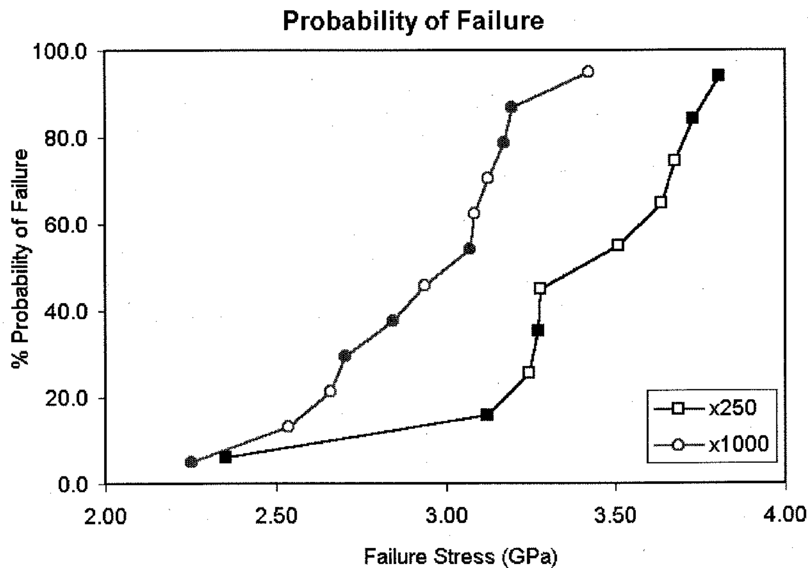

Figure 3.18 Probability of failure for different specimen lengths as a function of failure stress. The filled boxes are for 6 microns wide specimens and the empty boxes for 20 microns wide specimens

The Weibull distribution plot is shown in figure 3.21. The plot with the round points is derived for threshold stress equal to 1.2 GPa. This stress, σ_u, is chosen so that the correlation coefficient, R^2, becomes maximum [54]. These data, however, provide only a marginal improvement for R^2 when the value of the scaling parameter is only 2.11 GPa, which does not agree with the experimental data. According to the definition of this parameter, at σ_0 63% of the samples must have failed. On the other hand, if the stress threshold is set equal to 0 GPa (square data points in graph 3.18), the value of the scaling stress parameter is 3.3 GPa, which agrees well with the definition of σ_0 being the stress at

which 63% of the specimens fail. From the distribution function, as shown in figure 3.21, the value of the Weibull modulus is 8.56, and the scaling parameter is 3.3 GPa. The latter agrees very well with the 63% failure probability of the specimen population, which is 3.26 GPa.

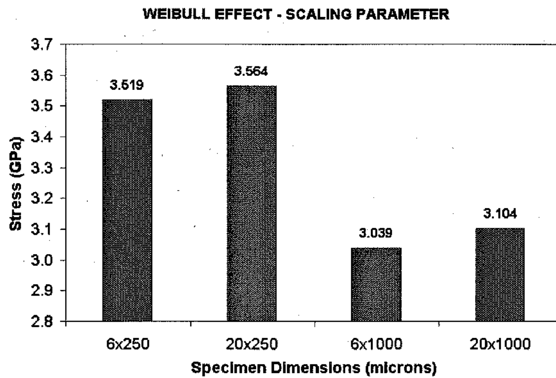

Figure 3.19 Scaling factor as calculated for different specimen dimensions.

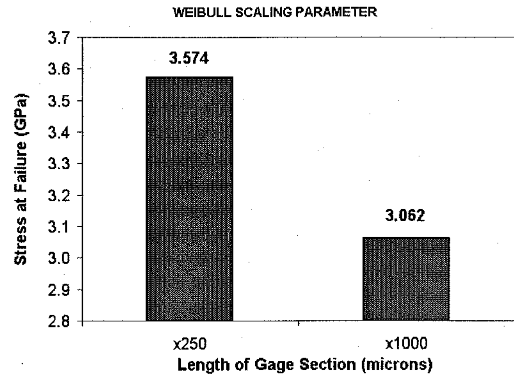

Figure 3.20 Scaling factor as calculated for specimen of the same length.

Table 3.7 Results of Weibull analysis

Specimen Width (μm)	*Specimen Length (μm)*	*Scaling Parameter (GPa)*	*Weibull Modulus (m)*
6	250	3.519	5.469
20	250	3.564	17.858
6	1000	3.039	8.096
20	1000	3.104	9.813

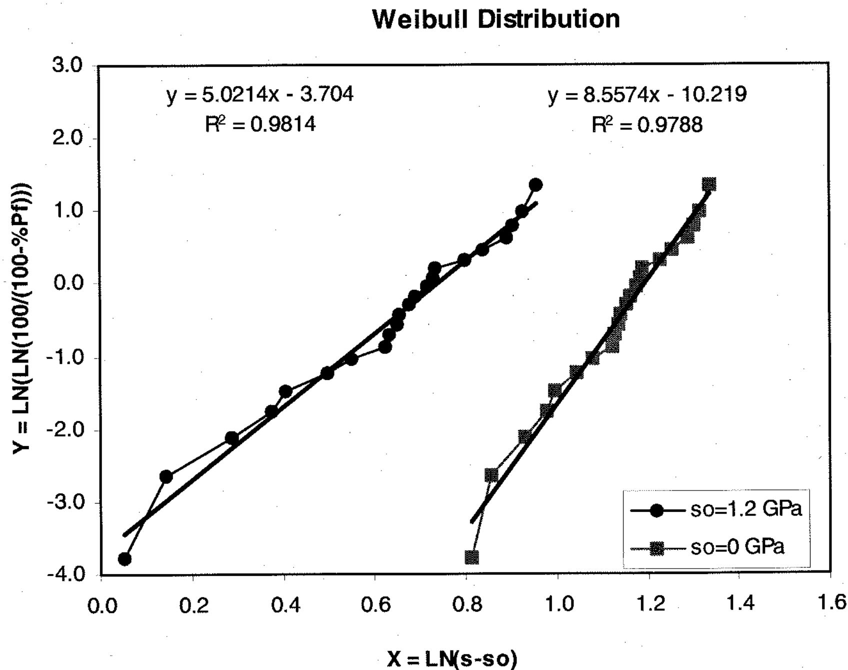

Figure 3.21 Weibull distributions for $\sigma_0 = 1.2$ (left) and $\sigma_0 = 0$ GPa (right).

3.3.4 Discussion and Implications

It is important to mention at this point that analogous Weibull distribution curves with similar scaling parameters (~10 GPa) have been established in the past for larger specimens of other materials with mechanical behavior similar to that of polysilicon, e.g., SiC, Si_3N_4, silica glass, Al_2O_3, *etc.* [49, 51]. It was also shown that a two-parameter Weibull distribution does not model the data with a well-defined straight line fit. Thus, plots similar that in figure 3.21 demonstrated limited linearity. Sometimes the standard deviation from this line can be large, as it also happens in the present study. The material fracture property near the surface can be different than away from the surface. This is so,

because the size distribution of flaws near the surface that can be quite different from those far from the surface and the fact that a crack near the surface is more detrimental than an identical crack far from it.

In a similar study [18] of thicker polysilicon (10.5 microns) and four different doping conditions, the measured modulus was 160±4.2 - 167±5.5 GPa, where 4.2 and 5.5 are the respective standard deviations. A high sidewall roughness of 0.5 microns peak to valley height was observed. The corresponding Weibull values based on the surface size effect were between 6 and 11.7 while the mean fracture strength varied between 1.08 and 1.25 GPa for the differently processed films. The values of m are within the range of the present results, while the fracture strength is significantly lower. This may be attributed to the significantly thicker specimens used in [18] and the resulting high population of micro-flaws in the film.

It is also important to mention the role of the grain boundaries in failure. They provide periodically weak regions on the surface of the film as will be described in Chapter 4. The grain boundaries may tend to block dislocation propagation that leads to plastic deformation. Consequently, polysilicon is linearly elastic until it fractures. On a macroscopic level, the grain boundaries may impede crack propagation, thus increasing strain capability. On the other hand, grain boundaries can be weak regions along which grain boundary sliding or crack initiation can occur [30].

CHAPTER 4

Effects of Prolonged Exposure to HF

4. 1 Introduction

Post-processing of thin films is critical for their mechanical response and life during applications. To better understand the geometric and boundary properties of a microstructure and their effect on the mechanical response of these materials under stress, the surface morphology of thin films processed under different conditions have been examined. This chapter discusses observations on certain aspects of the post-processing of polycrystalline silicon films that are crucial for their structure reliability.

An important step in MEMS fabrication by surface micromachining is the post-processing wet release with 49% HF. The latter is the strongest HF solution that can be contained and distributed commercially. It is a common belief in the surface micromachining community that the duration of exposure to HF does not affect the quality of the final polysilicon structure. Research work reported in the past is rather ambiguous presenting a disagreement as to what the actual effect of HF is on polysilicon. The potentially negative effects of HF on undoped polysilicon have been identified in the past in a study [55] that aimed at identifying the practical consequences of exposure of polysilicon in different chemical agents. A study of $POCl_3$-doped and undoped polysilicon has shown a catastrophic effect of buffered HF (NH_4F:HF) and HF vapor in air on $POCl_3$-annealed and as-deposited polysilicon [56]. The authors attributed the

damage to a possible grain boundary attack. Others stated that HF does not have a deleterious effect [57] on the material integrity. In a similar fashion an AFM/SEM analysis performed by Pleschinger et al. [58] showed that HF has a slightly smoothing effect on the polysilicon surface without reference to any adverse effects.

The present work illuminates this problem and discusses the microstructural effects and the resultant macroscopically measured strength of polysilicon exposed to 49% HF. Our observations have shown that this processing step is important because of the consequences of the attendant variations in surface roughness and of the change of film microstructure on failure behavior. The tensile strength of these specimens has been recorded for different exposure times to HF, and the failure surfaces have been examined to illustrate a possible association of the material microstructure with the measured mechanical "properties."

4.2 Effects of Exposure of Polycrystalline Silicon to HF Solutions

The specimens were manufactured at MCNC in runs MUMPs19, MUMPs21 and MUMPs35 primarily for determining Young's modulus and tensile strengths (see Chapters 2 and 3). All specimens were released at MCNC with a 49% HF wet etch for specific but different times, followed by a 15-minute de-ionized water rinse with subsequent water substitution by alcohol. They were dried using either a 10-minute oven bake (MUMPs19), or the supercritical drying CO_2 process (MUMPs21 and MUMPs35).

The evolution of surface roughness and notch acuity with exposure time in HF for the MUMPs21 run, as recorded in figure 4.1 with the aid of an AFM, illustrates the change in surface morphology with increasing exposure to HF. The release time is recorded in the upper right corner of each trace. The ordinates for all plots are amplified by a factor of 20 to accentuate the roughness profile. The surface scans were recorded within the same neighborhood on the samples, though not precisely on the same spot, so that the profiles are representative of a certain film area identified relative to the film (paddle) edges. The roughness clearly increases with etch time, rendering more and deeper trenches along grain boundaries that increase from 30 nm after 9 minutes exposure to HF, to almost 50 nm after 13 minutes of HF treatment. The evolution of the RMS roughness for specimens from MUMPs19 shows the same trend but involves larger amplitudes. These specimens had been exposed for 20 minutes in HF and 80 nm deep, randomly appearing, trenches have been recorded. This is ascribed to the difference in exposure time to HF: The longer the exposure, the deeper are the roughness patterns produced.

Deep surface grooves act as stress raisers and thus influence the fracture initiation. The tensile strength of samples from MUMPs21 tested in our laboratories was lower than that reported by other researchers [11] from the same MUMPs21 run, and this can be directly attributed to the fact that the etch time was longer for our specimens than that used in their studies as reported in table 2.1. The tensile strength of samples from MUMPs19, MUMPs21 and MUMPs35 runs and the corresponding exposure time in HF are shown in figure 4.2. The recorded tensile strength is shown next to each datum point, which represents an average of more than 20 measurements, with the error bounds indicating the standard deviation, which measured about 0.1 GPa for all tests. A distinct

trend of decreasing strength at a rate of 0.1 GPa/min exposure in HF is evident. The value of 1.3 GPa is cited in reference [11] from tensile tests with specimens of similar dimensions to these used in this work so that no potential size effects are introduced in the data of film strength. Large variations in tensile strength as an effect of exposure to HF, similar to these shown in figure 4.2, have been reported in the past [55] but without exposition of the likely cause of those variations.

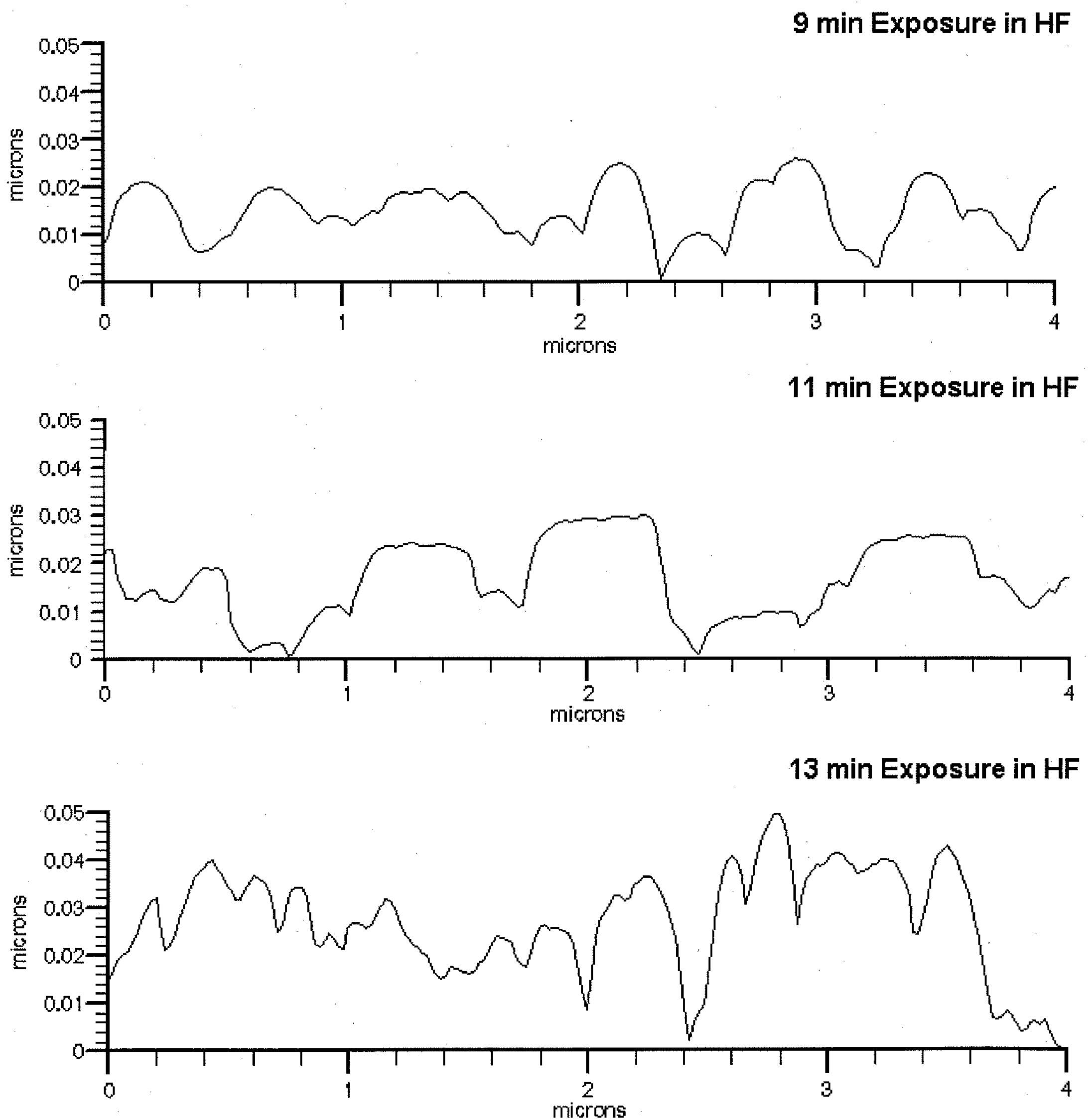

Figure 4.1 AFM line profiles of surface roughness for different etch times in 49% HF.

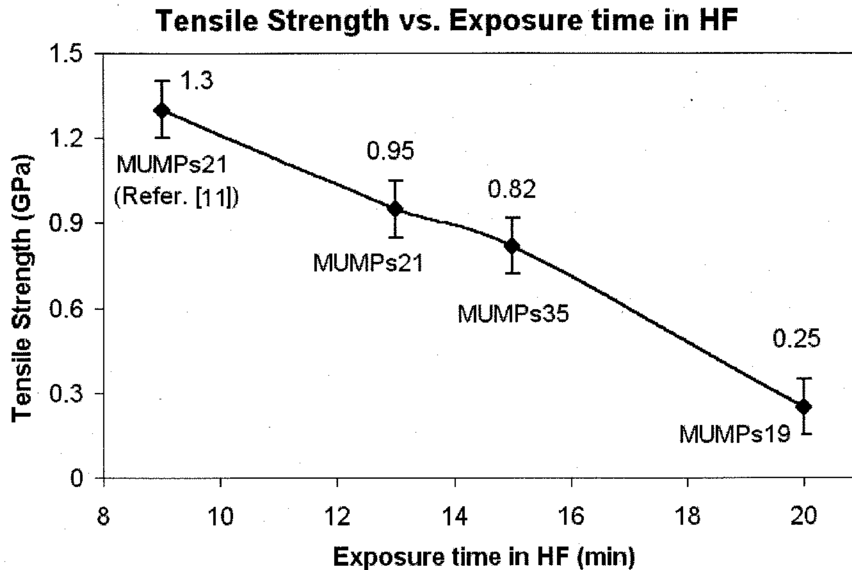

Figure 4.2 Tensile strength vs. exposure time in 49% HF.

The grain boundary depressions represent the largest (surface) flaws on the 2 μm thick film and provide stress concentrations for the onset of fracture. The average maximum depressions for (MUMPs21) films that possessed a 0.95 GPa tensile strength were about 30-35 nm while the average maximum depression for the (MUMPs19) samples that displayed a tensile strength of 0.25 GPa were about 60-80 nm.

An, at least qualitative, understanding of the role of this surface roughness may be obtained by a finite element study (ABAQUS) of a two-dimensional geometry which simulated the surface roughness by sinusoidal surface variation [20] and estimated the stress amplification for different frequencies and amplitudes of shallow surface notches. The prediction of this simple model with a wavelength of 300 nm, which corresponds to the average measured grain size for MUMPs21 specimens with 35 nm maximum roughness, gives a stress concentration at the surface grooves of about 1.7 times the average stress in the film, while for MUMPs19 specimens with 80 nm maximum

roughness, the stress concentration at the surface grooves is about 2.3 times larger than the average stress in the film (see figure 4.3). For this idealized geometry, the difference in the average strength of the two films should be about 30% (based on MUMPS21). However, measurements reveal this to be high as 65%. Thus, the significant difference in the average measured strength of the two specimen fabrication runs originates not only in the magnitude of the surface depressions that amplify the average stress in the film but also in additional damage. It is important to mention, however, that the actual surface features do not follow a sinusoidal profile and the surface undulations may be sharper which would lead to higher stress concentration and thus the results may differ from the conclusions derived from this simple model.

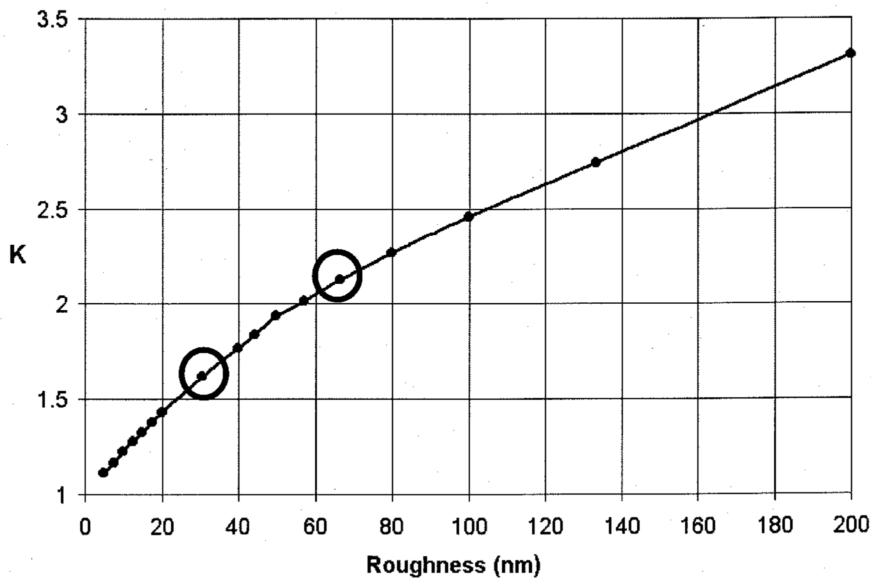

Figure 4.3 Stress concentration at a surface groove as a function of surface roughness computed in ABAQUS.

To provide further insight into this strength degradation, the fracture cross-sections of tension-tested specimens were examined in a SEM. In figure 4.4, the fractured

cross-section of a specimen exposed to HF for 13 minutes is shown. There are three distinct "layers" across the section, and this is characteristic of the film condition after exposure to HF: Thin layers on the top and bottom of the film and a thicker layer in the interior. The fracture features in the latter correspond to the columnar structure of the grains, and indicate a mixed intergranular and transgranular failure. The uneven pattern in the thin bottom layer has its origin in the nucleation of grains during deposition. It is important to mention the different failure pattern observed in the top layer of the film (in the upper part of the image). This layer contains the grooves along the grain boundaries; these facilitate a clear intergranular fracture indicated by holes comparable in size to the diameter of a grain measured via AFM.

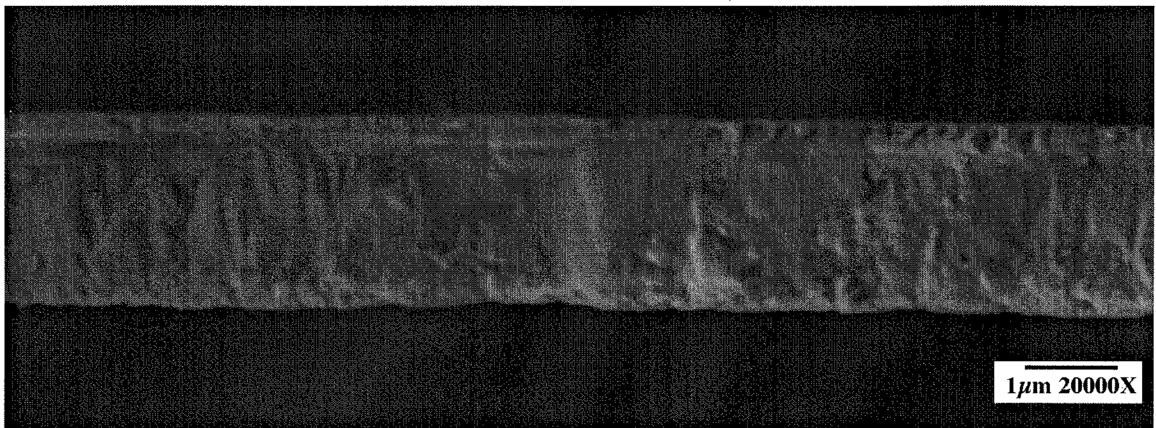

Figure 4.4 Fracture cross-section of specimen exposed to HF for 13 minutes. The tensile strength was 0.95 GPa.

Even relatively short exposure to HF (13 minutes) results in a surface layer of low strength (figures 4.5 - 4.6) as well as intergranular failure. The effect of HF on the top layer can be dramatic as can be seen from the delaminated surface "crust" at the lower right edge of the film in figure 4.6. The thickness of this weak crust is on the order of

100-150 nm with many small microcracks following the surface grooves along grain boundaries. Notice the grain structure of the cross-section as well as the delamination of the top surface layer in figure 4.6. Similarly, figure 4.7 shows that at 13 minutes exposure to HF the fracture profile is of mixed intergranular and transgranular failure, but the top surface clearly fails in an intergranular manner after individual, loosely held grains are ejected to form deep holes in the surface.

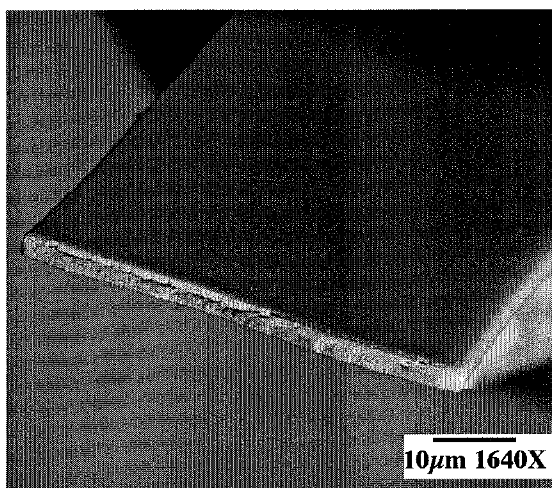

Figure 4.5 Cross-section of a specimen tested in tension. Note the "crust" on the top surface of the specimen (13 minutes of exposure to HF).

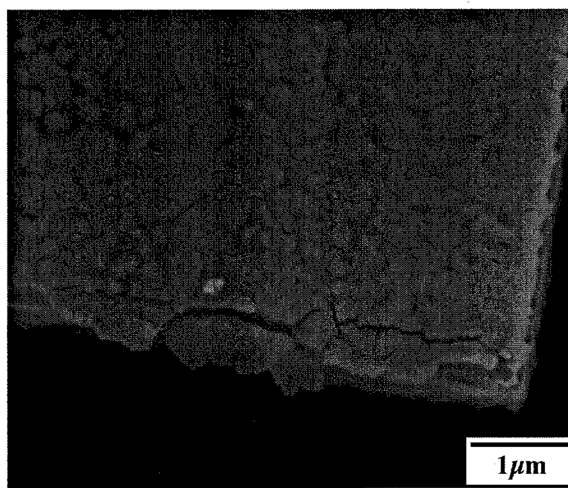

Figure 4.6 Specimens exposed for 13 minutes to HF demonstrated delamination of a surface layer (crust) and intergranular fracture at the top surface.

The strength of the MUMPs21 specimens was considerably higher than that measured for MUMPs19 specimens. The low strength of specimens tested from MUMPs19 (~0.3 GPa) is attributed to the long exposure of the latter (>20 min.) to HF when compared to the time used for the MUMPs21 specimens. Accordingly, the strength of the latter is lower than that which was reported by other researchers and can be directly attributed to the fact that the etching time was longer than that they have stated. These

deep surface grooves act as micro-notches that initiate fracture and occur at the grain boundaries that are etched more readily and faster than the grains themselves. Analogous results have been reported in the literature for various treatments with hydrofluoric acid that resulted in variations in Young's modulus and failure strength [55].

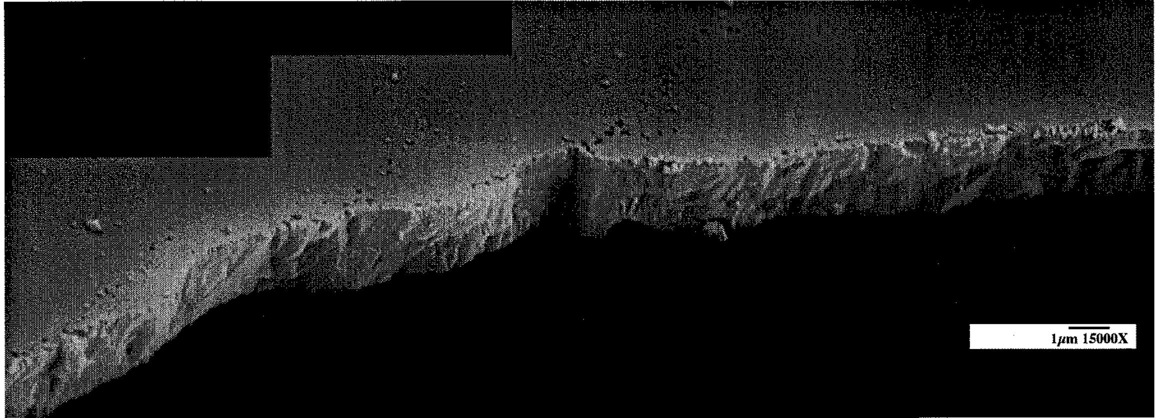

Figure 4.7 Fracture profile composed of a series of SEM pictures that indicates local intergranular fracture (see grooves on the top surface) as well as signs of transgranular failure at the cross-section. The film was exposed for 13 minutes to HF.

Our AFM/SEM study has indicated an intergranular fracture type for specimens from MUMPs19. This represented an effect of the etching process on the grain boundary strength. SEM observations have also shown that the release-induced roughness is strongly dependent on residual film stresses. Films with large lateral dimensions displayed variable roughness across their width demonstrating increasing roughness away from the free edges of the film. This was due to the fact that although different areas of the top surface of the film were exposed to HF for the same time, they were subject to the residual stresses for variable time as the release process progressed. By comparison, specimens from the MUMPs19 run exposed to HF for 20 minutes shown in figures 4.8 and 4.9 demonstrate a surface roughness of distinctively high amplitude. In addition,

these AFM records show an influence of the grain structure on the character of crack propagation and a preference for intergranular fracture.

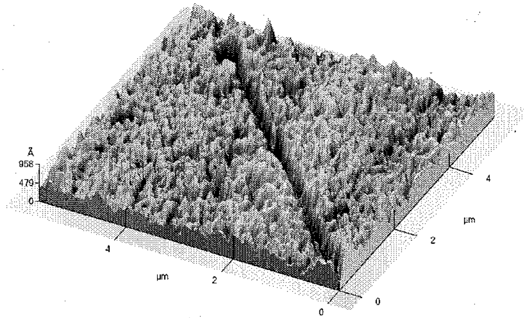

Figure 4.8 AFM image of intergranular failure by a through the thickness crack.

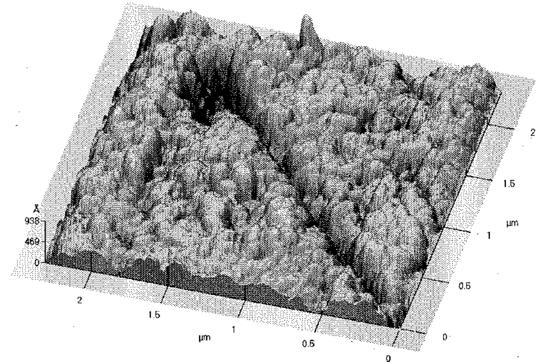

Figure 4.9 Detail of image 4.8 that shows crack arrest when a crack meets a grain.

SEM images provide additional information on the internal structure of the film of particularly low strength; a characteristically porous structure which results from HF etching inside the film or along the grain boundaries into the interior of the film (figures 4.10 and 4.11). The formation of an internal network of channels significantly decreases the material continuity and reduces the film strength. Similarly, because of this "porous" character of the polycrystalline material, the measured effective modulus is only on the order of 130 GPa as compared to 165 GPa for the MUMPs21 films.

Besides affecting the material rigidity (modulus) the internally eroded structure is responsible for reduced (failure) strength. Recall that the surface stress concentrations alone were insufficient to fully explain the low strength of MUMPs19 specimens. The internal network of void channels, however, induces numerous internal stress concentrations resulting in the low strength.

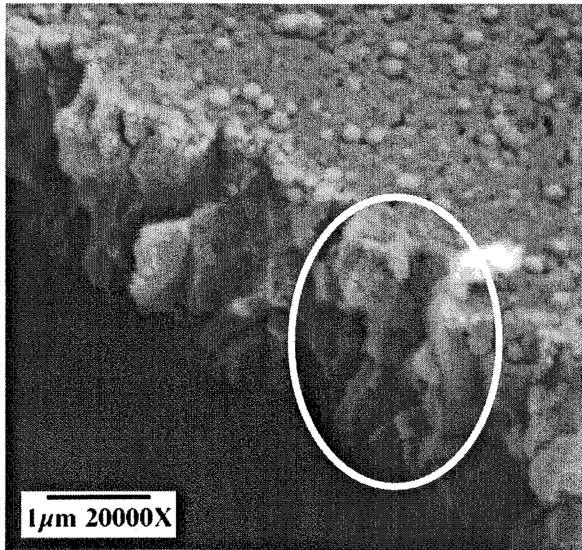

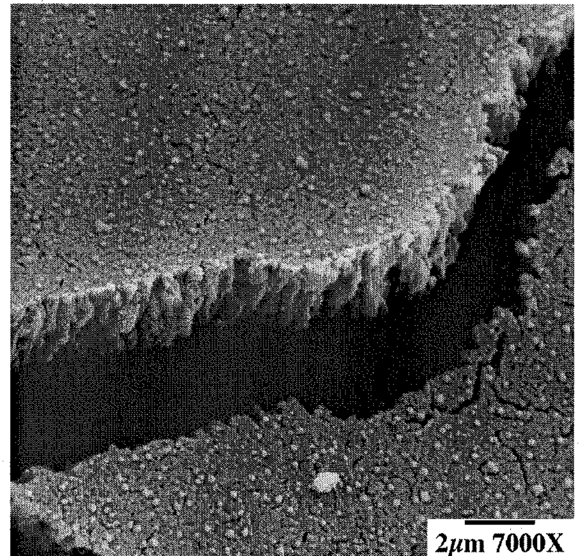

Figure 4.10 The marked groove indicates the missing columnar grain through the film thickness that corresponds to a grain diameter 0.3 microns.

Figure 4.11 Specimens exposed to HF for 20 min. Two matching surfaces with multiple cracks at the sides of the main crack.

In summary, it is evident that short exposure to HF results in the formation of surface stress concentrations that facilitate failure, while long exposures to HF leads to additional internal stress raisers through the formation of a network of voids or channels within the film. Long exposure to HF (20 minutes or more) leads to distinctly intergranular fracture throughout the thickness of the film as seen in figures 4.10 and 4.11. The lower right portion of the SEM image 4.11 shows that grooves around the grain boundaries are forming a microcrack network adjacent to the main crack, which is characteristic of intergranular brittle fracture. In the same manner, figures 4.12 and 4.13 illustrate the characteristic "zipper" pattern of intergranular fracture and the multiple cracks close to the main crack tip.

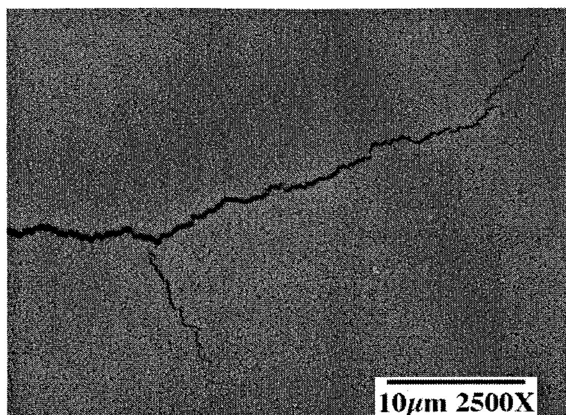

Figure 4.12 Long exposure to HF leads to distinct intergranular fracture.

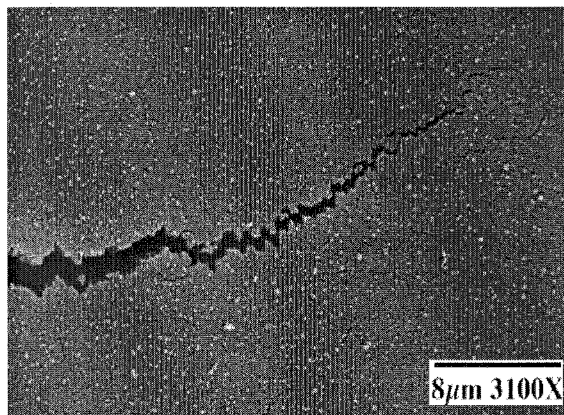

Figure 4.13 Characteristic "zipper" pattern of intergranular fracture.

4.3 Discussion

The observations on the effect of HF exposure on the degradation of polycrystalline silicon deserves discussion on the etch rates encountered in the MCNC and other specimen microfabrication processes. The etch rate of bulk silicon by HF is extremely low. Hu and Kerr [60] have measured an etch rate of 1.8 nm/h for the {111} face of *n*-type Si. The etch rate is much higher in amorphous silicon (up to 5 times higher than bulk Si) [61] reaching values of 10 nm/h. From the previous discussion it is clear that the grain boundaries, characterized by material disorder, are attacked more severely by HF. However, the HF exposures times encountered in this work are too low for these etch rates to have a serious effect and, therefore, the observed HF influence must be assisted by other factors. HF attacks SiO_2 with very high rates (>10 μm/min). The possibility of the existence of SiO_2 at the grain boundaries due to oxygen contamination has been addressed through an Auger study. This examination did not, however, show the presence

of measurable quantities of oxygen (beyond the level of background noise) after the removal of the top layer of the film by ion beam sputtering[11]. Very low concentration of oxygen contamination in the film and the presence of SiO_2 in the grain boundaries may still be a valid reason for the recorded effects. Several other factors, however, may contribute to the described observations including an the electrochemical effect due to the gold layer in contact with our silicon samples and the possible metal ion impurities in the HF release bath. It has been observed by Chan et al. [62] that polysilicon layers in contact with gold layers demonstrated a rougher surface after etching and were etched more by as much as 10 nm during only a 2.5 minute exposure to HF, when compared to polysilicon layers in the absence of gold. These authors observed also that beams "curl up," after etching, more when they are connected to a gold layer. This has also been observed in our work for specimens from MUMPs19 (see figure 4.14)[12]. The same specimens were etched faster by HF due to an electrochemical potential induced by the gold layer. In this case the polysilicon layer was thinner and rougher than the films not in contact with gold. The top surfaces are etched quickly leaving behind a specimen with higher average stress.

Poisson et al. [63] chemically plated gold on polysilicon using an HF solution and then heated the assembly to diffuse the gold. It was found that there is no particular preference for gold transport in the grain boundaries. Gold atoms migrate into the grains until they are trapped at the grain boundaries where they strongly segregate and diffuse only slowly [30]. This gold segregation increases with decreasing temperature.

---

[11] Personal communication with Professor A. Heuer in Case Western Reserve University and his collaborator Dr. C. Deeb, who has examined by chemical microanalysis samples from this work fabricated in MUMPs19, assured no presence of oxygen in the polysilicon grains.

[12] The gold pads are the brightest areas in SEM figures 4.14.

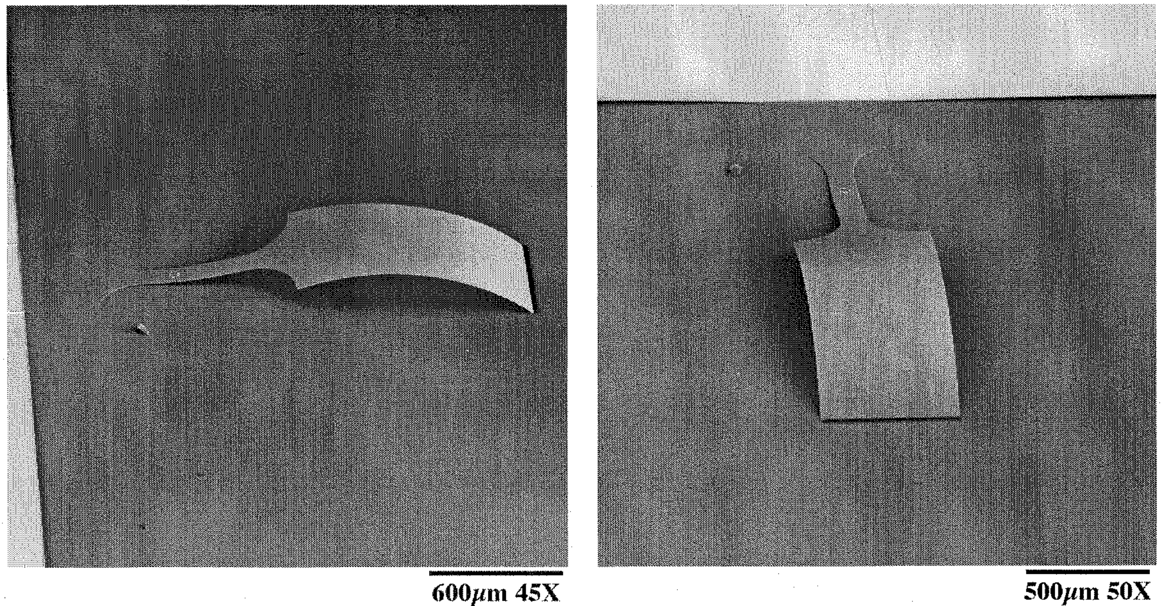

Figure 4.14 Specimens from MUMPs19 strongly curled after long HF release.

The presence of metal ions in the HF bath in the form of impurities would also assist a combined electrochemical effect capable of expediting the degradation of the material. The presence of copper and other ionic impurities in HF has been studied in the past with reference to the VLSI industry. It was found that, in HF solutions, copper, silver and palladium ions were selectively deposited on the silicon surface [64]. Torcheaux et al. [64] developed an electroless deposition theory, which supported that, in the presence of noble metals, silicon oxidation occurs to an electrically equivalent quantity of silicon atoms near the deposition metal site. Although the amount of dissolved silicon in aqueous HF solutions is very small, an ohmic drop inside the silicon layer results in corrosion that is localized in a small domain near the metallic nuclei. Moreover, polysilicon films with deposited gold layers have been found [65] to be excellent used-HF purification media via adsorption of metal ions (Cu and Au) on polysilicon surface. Thus, the presence of gold pads on our structures can accelerate the adsorption of metal ion impurities from the

etching bath to the surface of polysilicon. Then, according to the mechanism described in [64], chemical erosion of the structural material can take place.

On the other hand, annealing of polysilicon with an overlying gold layer results in the formation of polysilicon crystallites in the gold [66]. This occurs at annealing temperatures below the eutectic temperature of the Si-Au system (370 °C). The result is erosion of the silicon layer and growth of the crystallites in the metal layer. This growth of crystallites has been observed even at 200 °C annealing for a period of a few minutes. On the other hand, no similar phenomena have been observed for the Si-Cr system.

The conditions during etching of our specimens were very similar to those for the formation of porous silicon [67]. The chemical solution used for producing porous silicon is high purity 40% HF in aqueous solution diluted with ethyl alcohol. The latter is used because of the hydrophobic character of the silicon surface. The main conditions for the formation of porous silicon are: (1) The silicon wafer must be anodically biased, (2) light must be supplied.

The proposed chemical reaction is as follows [67]:

$$Si + 6HF \leftrightarrow H_2SiF_6 + H_2 + 2H^+ + 2e^- \quad (4.1)$$

Reaction (4.1) is also written [68] as:

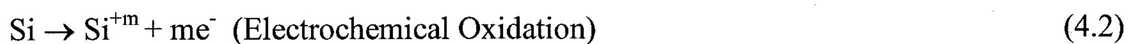

$$Si \rightarrow Si^{+m} + me^- \text{ (Electrochemical Oxidation)} \quad (4.2)$$

$$Si^{+m} + (4-m)H^+ \rightarrow Si^{+4} + \tfrac{1}{2}(4-m)H_2 \text{ (Chemical Oxidation)} \quad (4.3)$$

It is experimentally verified that $m \approx 2$.

In the present investigation, the polysilicon specimens were in contact with gold layers and have been treated in a HF/CH_3OH solution during sacrificial etching. These metal layers may set up the potential for the rapid etch of polysilicon. Thus a potential cause for the observed effects in the microstructure of polysilicon after exposure to HF may be a combined electrochemical and chemical oxidation that obey the chemical equations (4.2) and (4.3).

It is also important to mention that the specimens are not ideal silicon films but they are doped with phosphorous, which can affect the very low etch rate of bulk silicon. In polycrystalline materials grain boundaries provide disordered regions along which dopant atoms can readily diffuse [30]. In addition, grain boundaries also are low energy sites where dopant atoms can be preferentially located. Grain boundary diffusion is most rapid in materials with columnar grains. For phosphorus, important grain boundary segregation has been cited in literature [30]. Moreover, specimens from MUMPs process were doped on both sides using PSG and diffusion doping (see also paragraph 2.2.2), which can result to high dopant concentrations at the grain boundaries after segregation. This manufacturing step can also be important and responsible for the weak surface layer observed in figures 4.4-4.7.

Specimens from Sandia National Labs have also been tested. They were manufactured according to the SUMMiT-V process (Sandia Ultra-planar Multilevel MEMS Technology – five layer process) and released at Sandia with 90 min exposure to 1:1 $HF:H_2O$ [69]. These specimens have consistently demonstrated [53] high average tensile strength on the order of 3 GPa (see section 3.2.2). The failure pattern was clearly

transgranular[13], supporting the observations in this work that the failure pattern of polysilicon is transgranular associated with high material strength and it becomes intergrain-dominated with increasing exposure to HF and attendant low strength. It is also of interest to note that these specimens were not in contact with any metal layer.

The observations made here were gathered from polysilicon specimens exposed in HF for longer times than is common practice. The appropriate spatial distribution of etch-holes helps to avoid the detrimental effects of long exposure to HF. However, when this is not possible the current results need to be considered so that the undesired excessive surface roughness and the related release effects will be limited.

---

[13] Transgranular failure has also been reported in the past, see [59].

CHAPTER 5

Comments and Conclusions

The important accomplishments and results of this investigation can be summarized in the following points:

- An improved apparatus has been developed to measure the elastic tensile properties (Young's modulus, tensile strength) of surface micromachined polycrystalline silicon specimens. The newly designed tensile tester makes use of a UV curable adhesive and has made it possible to test polysilicon specimens until ultimate failure, which was not feasible by other methods. In the present method, records of the specimen surface topography acquired with an AFM are used to determine the displacement field by the digital image correlation. This full-field, direct and local measurements technique provides the capability of full field deformation measurement of any type of thin film materials with nanometer resolution.
- The measurements of Young's modulus agree very well with literature and are within the narrow theoretical bounds calculated by the Voigt – Reuss bounds. The local values of Young's modulus obtained using deformation records recorded by an AFM and digital image correlation over a small surface region also agree with average values deduced from end-to-end deformations of (non-uniform) tension specimens.

- A study of elliptically perforated specimen configurations showed a clear dependence of the local failure stress at the notch tip on the radius of curvature, especially when the latter is on the same order of magnitude as the grain size. The results demonstrated that variable notch radii have an important effect on the failure strength of MEMS-scale specimens. The local failure strength as well as the scatter of strength data increase when the domain becomes smaller. When the notch radius becomes one micron (three times the grain size) then a strong size effect is observed. This effect becomes moderate for larger radii of curvature until the latter reaches a value of about eight or ten microns (25 times the grain size); then, the local stress at failure at the notch tip reaches the value of the material "tensile strength," as recorded in tensile tests of specimens with similar dimensions. These observations are in accordance with the probabilistic nature of failure. It is also suggested that there is no significant dependence of the failure stress on the stress concentration factor at the notch tip.

- In the same context, it is found that there is no dependence of the Young's modulus on tensile specimens volume. An analysis using the Weibull cumulative function, however, reveals a clear dependence of polysilicon strength on the length of the tensile specimens. An immediate implication is the lack of a unique value for the tensile strength of brittle thin polysilicon films due to the dependence of the measured strength on the dimensions of the test samples.

- MEMS post-processing by 49% HF has been identified as a key parameter in determining thin film failure characteristics. It is found that surface roughness in the form of groove formations at grain boundaries depends distinctly on the HF release time and is identified as one cause for reduced fracture strength.

- Increasing exposure to HF results in a change of fracture from transgranular to an intergranular mode on the "top" surface. After long exposures to HF (longer than 20 minutes), failure becomes intergranular throughout the film thickness. The change in the failure type results in an attendant decrease of the tensile strength. Several parameters in post processing treatment may intensify the effect of HF on the quality of the material; the presence of metal ions in the etch bath or the contact of polysilicon with gold or other metal layers may create an electrochemical potential that along with the presence of HF accelerates the etching of polycrystalline silicon at the grain boundaries and the consequent degradation of its mechanical strength.

References

[1] R. Howe, B. Boser and A. Pisano, "Polysilicon Integrated Microsystems: Technologies and Applications," *Sensors and Actuators A*, **56**, pp. 167-177, 1996.

[2] W. Lang, "Reflections on the Future Microsystems," *Sensors and Actuators A*, **72**, pp. 1-15, 1999.

[3] M. Pottenger, B. Eyre, E. Kruglick and G. Lin, "MEMS: The Maturing of a new Technology," Solid State Technology, **40** (9), pp. 89-96, 1997.

[4] D. S. Eddy and D. R. Sparks, "Application of MEMS Technology in Automotive Sensors and Actuators," *Proceedings of the IEEE*, **86** (8), pp. 1747-1755, 1998.

[5] N. Yarzdi, F. Ayazi and K. Najafi, "Micromachined Inertial Sensors," *Proceedings of the IEEE*, **86** (8), pp. 1640-1659, 1998.

[6] H. Fujita, "Microactuators and Micromachines," *Proceedings of the IEEE*, **86** (8), pp. 1721-1732, 1998.

[7] K. Schwab, J. L. Arlett, J. M. Worlock and M. L. Roukes, "Thermal Conductance Through Discrete Quantum Channels," *Physica E*, **9** (1), pp. 60-68, 2001.

[8] J. Voldman, M. L. Gray and M. A. Schmidt, "Microfabrication in Biology and Medicine," *Annual Reviews in Biomedical Engineering*, **1**, pp. 401-425, 1999.

[9] H. Fujita and H. Toshiyoshi, "Optical MEMS," *IEICE Transactions of Electronics*, **E83-C** (9), pp. 1427-1434, 2000.

[10] D. M. Tanner, J. A. Walraven, K. S. Helgesen, L. W. Irwin, D. L. Gregory, J. R. Stake and N. F. Smith, "MEMS Reliability in a Vibration Environment," *IEEE International Reliability Physics Symposium,* San Jose, CA, April 10-13, pp. 139-145, 2000.

[11] W. N. Sharpe, J. S. Brown, G. C. Johnson and W. G. Knauss, "Round-robin tests of modulus and strength of polysilicon," *Mater. Res. Soc. Proc.* **518**, San Francisco, CA, pp. 57-65, 1998.

[12] T. Yi and C. J. Kim, "Measurement of mechanical properties for MEMS materials," *Meas. Sci. Technol.* **10**, pp. 706-716, 1999.

[13] J. Koskinen, J.E. Steinwall, R. Soave and H.H. Johnson, "Microtensile Testing of Free-Standing Polysilicon Fibers of Various Grain Sizes," *J. Micromech. Microeng.*, **3**, pp. 13-17, 1993.

[14] D. Maier-Schneider, J. Malbach and E. Obermeier, "Variations in Young's Modulus Intrinsic Stress of LPCVD Polysilicon due to High-Temperature Annealing," *J. Micromech. Microeng.*, **5**, pp. 121-124, 1995.

[15] Y. C. Tai and R. S. Muller, "Measurement of Young's Modulus on Microfabricated Structures using a Surface Profiler," IEEE Micro Electro Mechanical Systems, 11-14 February, Napa Valley, CA, pp. 147-152, 1990.

[16] S. Greek, F. Ericson, S. Johansson and J. Schweitz, "In Situ Tensile Strength Measurement and Weibull Analysis of Thick Film and Thin Film Micromachined Polysilicon Structures," *Thin Solid Films*, **292**, pp. 247-254, 1997.

[17] T. Tsuchiya, O. Tabata, J. Sakata and Y. Taga, "Tensile Testing of Polycrystalline Silicon Thin Films Using Electrostatic Force Grip," *T.IEE Japan*, **116-E** (10), pp. 441-446, 1996.

[18] S. Greek, F. Ericson, S. Johansson, M. Fürtsch and A. Rump, "Mechanical Characterization of Thick Polysilicon Films: Young's Modulus and Fracture

Strength Evaluated with Microstructures," *Journal of Micromechanics and Microengineering*, **9**, pp. 245-251, 1999.

[19] F. A. Breton and W. G. Knauss, "Error Limitations in the Determination of Mechanical Properties of Thin Films," *Journal of Reinforced Plastic and Composites*, **16** (1), 1997.

[20] I. Chasiotis and W. G. Knauss, "Mechanical Evaluation of Polysilicon Properties by Means of Probe Microscopy," *Proc. of the SPIE*, **3512**, Santa Clara, pp. 66-75, 1998.

[21] W. N. Sharpe, K. T. Turner and R. L. Edwards, "Tensile Testing of Polysilicon," *J. of Experimental Mechanics*, **39**, (3), pp. 162-170, 1999.

[22] D. A. Koester, R. Mahadevan, B. Hardy and K. W. Markus, "MUMPs Design Handbook," **Rev. 5.0**, 2000.

[23] R. Maboudian and R. T. Howe, "Critical Review: Adhesion in Surface Micromechanical Structures," *J. Vac. Sci. Technol. B*, **15** (1), pp. 1-20, 1997.

[24] N. Tas, T. Sonnenberg, H. Jansen, R. Legtenberg and M. Elwenspoek, "Stiction in Surface Micromachining," *J. Micromech. Microeng.*, **6**, pp. 385-397, 1997.

[25] G. Vendroux and W. G. Knauss, "Submicron Deformation Field Measurements II: Improved Digital Image Correlation," *Experimental Mechanics*, **38** (2), pp. 86-92, 1998.

[26] G. Vendroux, N. Schmidt and W. G. Knauss, "Submicron Deformation Field Measurements III: Demonstration of Deformation Determinations," *Experimental Mechanics,* **38** (3), pp. 154-160, 1998.

[27] M.A. Sutton, M. Cheng, W. H. Peters, Y. J. Chao and S.R. McNeil, "Application of an Optimized Digital Image Correlation Method to Planar Deformation Analysis," *Image Vision Computing*, **4** (3), pp. 143-150, 1986.

[28] Y. Huang, "Scanning Tunneling Microscopy and Digital Image Correlation in Nanomechanics Investigations," Ph.D. Thesis, California Institute of Technology, 2001.

[29] P. Lange, M. Kirsten and W. Riethmuller, "Thick Polycrystalline Silicon for Surface Micro-Mechanical Applications: Deposition, Structuring and Mechanical Characterization," *Sensors and Actuators A*, **54**, pp. 674-678, 1996.

[30] T. Kamins, "Polycrystalline Silicon for Integrated Circuits and Displays," Kluwer Academic Publishers, 2nd edition, 1998.

[31] B. Fultz and Jim Howe, "Transmission Electron Microscopy and Diffractometry of Materials," **Vol. 1**, 1995.

[32] R. Hill, "The Elastic Behavior of a Crystalline Aggregate," *Proc. Phys. Soc. London, Sect. A*, **65**, pp. 349-354, 1952.

[33] W. Voigt, "Lehrbook der Kristallphysik," 2nd Edition, Teubner, Leipsig, pp. 962, 1928.

[34] A. Reuss, "Berechnung der Fliessgrenze von Mischkristallen auf Grund der Plastizitättsbediengung fuer EinKristalle," *Z. Angew. Math. Mech.*, **9** (1), pp. 49-58, 1929.

[35] W. A. Brantley, "Calculated Elastic Constants for Stress Problems Associated with Semiconductor Devices," *Journal of Applied Physics*, **44** (1), pp. 534-535, 1973.

[36] L. Elbrecht and J. Binder, "The Mechanical Properties of Thin Polycrystalline Silicon Films as a Function of Deposition and Doping Conditions," *Sensors and Materials*, **11**(3), pp. 103-179, 1999.

[37] A. A. Griffith, "The Phenomena of Rupture and Flow in Solids," *Philosophical Transactions of the Royal Society A*, **221**, pp. 163-197, 1921.

[38] Z. P. Bazant and J. Planas, Fracture and Size Effect in Concrete and other Quasibritle Materials, CRC Press, 1997.

[39] C. E. Inglis, "Stresses in a Plate due to the Presence of Cracks and Sharp Corners," *Transactions of the Royal Institution of Naval Architects*, **60**, pp. 219-230, 1913.

[40] H. Neuber, Theory of Notch Stresses, Edwards Bros Inc., 1946.

[41] S. P. Timoshenko and J. N. Goodier, Theory of Elasticity, McGraw-Hill, 1970.

[42] S. C. Tan, "Laminated Composites Containing an Elliptical Opening. I. Approximate Stress Analyses and Fracture Models," *Journal of Composite Materials,* **21**, pp. 925-948, 1987.

[43] S. G. Lekhnitskii, S. W. Tsai and T. Cheron, Anisotropic Plates, 2nd edition, Gordon and Breach Science Publishers, pp. 167, 1968.

[44] M. Isida and K. Nakagawa, "On the Stress Gradients in Tension and Bending of a Perforated Strip," P*roceedings of the Third Japan National Congress for Applied Mechanics,* pp. 1-4, 1954.

[45] M. Isida, "On the Tension of a Semi-infinite Plate with an Elliptic Hole," *Scientific Papers of Faculty of Engineering Tokushima University*, **5** (1), pp. 75-94, 1955.

[46] S. C. Tan, "Finite Width Correction Factors for Anisotropic Plate Containing a Central Opening," *Journal of Composite Materials,* **22**, pp. 1080-1097, 1988.

[47] R. E. Peterson, Stress Concentration Factors, Wiley, New York, 1974.

[48] M. Isida, "On the Tension of a Strip with a Central Elliptic Hole," *Transactions of the Japan Society of Mechanical Engineers*, **21**, pp. 514, 1955.

[49] T. T. Shih, "An evaluation of the probabilistic approach to brittle design," *Engineering Fracture Mechanics*, **13**, pp. 257-271, 1980.

[50] B. Bergman, "On the Estimation of the Weibull Modulus," *Journal of Materials Science Letters,* **3**, pp. 689-692, 1984.

[51] M. F. Ashby and D. R. H. Jones, Engineering Materials II: An Introduction to Microstructures, Processing, and Design, Pergamon Press, pp. 170, 1998.

[52] J. D. Sullivan and P. H. Lauzon, "Experimental Probability Estimators for Weibull Plots," *Journal of Materials Science Letters,* **5**, pp. 1245-1247, 1986.

[53] D.A. LaVan, T. Tsuchiya, G. Coles, W. G. Knauss, I. Chasiotis and D. Read "Cross Comparison of Direct Strength Testing Techniques on Polysilicon Films," Mechanical Properties of Structural Films, ASTM **STP 1413**, American Society for Testing and Materials, West Conshohocken, PA, 2001.

[54] A. J. Hallinan, "A Review of the Weibull Distribution," *Journal of Quality Technology*, **25**(2), pp. 85-93, 1993.

[55] J. A Walker, K. J. Gabriel and M. Mehregany, "Mechanical Integrity of Polysilicon Films Exposed to Hydrofluoric Acid Solutions," *Journal of Electronic Materials,* **20** (9), pp. 665-670, 1991.

[56] T. A. Lober and R.T.Howe, "Surface Micromachining Processes for Electrostatic Microactuator Fabrication," IEEE Solid-State Sensor and Actuator Workshop, Hilton Head, SC, pp. 59-62, 1988.

[57] W. N. Sharpe, Y. Bin and E. L. Richard, "Advances in Tensile Testing of Polysilicon Thin Films," Proceedings of the 1997 ASME International Mechanical Engineering Congress and Exposition, Dallas, TX, pp. 113-116, 1997.

[58] A. Pleschinger, J. Lutz, F. Kuchar, H. Noll and M. Pippan, "A Structural and Topographical Study of low-pressure Chemical Vapor Deposited Polysilicon by Scanning Probe Microscopy," Journal of Applied Physics, **81** (10), pp. 6749-6753, 1997.

[59] R. Ballarini, R. L. Mullen and A.H. Heuer, "The Fracture Toughness of Polysilicon Microdevices: A First Report," *Journal of Materials Research*, **12** (4), pp. 915-922, 1997.

[60] S. M. Hu and D. R. Kerr, "Observation of Etching of n-type Silicon in Aqueous HF Solutions," *Journal of Electrochemical Society,* **114**, pp. 414, 1967.

[61] L. Liou, W. G. Spitzer and S. Prussin, "Amorphous-Silicon Produced by Ion-Implantation - Etching Rate in HF Solution and Effect of Annealing," *Journal of Electrochemical Society,* **131**(3), pp. 672-674, 1984.

[62] E. K. Chan, K. Garikipati and R. W. Dutton, "Comprehensive Static Characterization of Vertical Electrostatically Actuated Polysilicon Beams," *IEEE Design and Test* **16** (4), pp. 58-65, 1999.

[63] C. Poisson, A Rolland, J. Bernardini and N. A. Stolwijk, "Diffusion of Gold into Polycrystalline Silicon Investigates by means of the Radiotracer ^{195}Au," *Journal of Applied Physics*, **80**(11), pp. 6179-6187, 1996.

[64] L. Torcheaux, A. Mayeux and M. Chemla, "Electrochemical Coupling Effects on the Corrosion of Silicon Samples in HF Solutions," *Journal of Electrochemical Society,* **142** (6), pp. 2037-2046, 1995.

[65] K. Yamamoto, T. Shimono, T. Okada, Y. Kawazawa and T. Tatsuno, "New Method of Purification of HF Chemicals for Very Large Scale Integration Manufacturing," *Journal of Electrochemical Society,* **143** (12), pp. 4119-4124, 1996.

[66] K. Nakamura, J. O. Olowalafe, S. S. Lan, M. A. Nikolet, J. W. Mayer and R. Shima, "Interaction of Metal Layers with Polycrystalline Si," *Journal of Applied Physics*, **47**(4), pp. 1278-1283, 1976.

[67] C. Vinogoni and L. Paresi, "Porous Silicon Microcavities," *Technical Report*, pp. 1-35, 1999.

[68] A. Uhlir, "Electrolytic Shaping of Germanium and Silicon," *The Bell System Technical Journal*, **3**, pp. 333-347, 1956.

[69] C. W. Dyck, J. Smith, S. Miller, E. Russick and C. Adkins, "Supercritical Carbon Dioxide Drying of Surface-Micromachined Micromechanical Structures," *Proceedings of the SPIE,* **2879**, pp. 225-235, 1996.

[70] D. Meier-Schneider, "LPCVD-polysilizium in der Mikromechanik: Bestimmung der Elastischen Eigenschaften" Doctoral Dissertation, VDI-Verlag, Düsseldorf, 1995.

APPENDIX

A. Calculation of the Voigt - Reuss - Hill Bounds

Using the equations from Hill [32] we can calculate the bounds for the elastic constants for polycrystalline silicon assuming no preferred orientation:

The Young's modulus is

$$E = \left[\frac{1}{3G} + \frac{1}{9K}\right]^{-1} \quad (A1)$$

and the Poisson's ratio

$$\nu = \frac{1}{2}\left[1 - \frac{3G}{3K + G}\right] \quad (A2)$$

where

K= Bulk modulus

G = Rigidity modulus

The moduli for the Voigt model are

$$K_{Voigt} = \frac{1}{9}\left[(c_{11} + c_{22} + c_{33}) + 2(c_{12} + c_{13} + c_{31})\right] \quad (A3)$$

$$G_{Voigt} = \frac{1}{15}\left[(c_{11} + c_{22} + c_{33}) - (c_{12} + c_{23} + c_{31}) + 3(c_{44} + c_{55} + c_{66})\right] \quad (A4)$$

and for the Reuss model

$$K_{Reuss} = \frac{1}{\left[(s_{11} + s_{22} + s_{33}) + 2(s_{12} + s_{13} + s_{31})\right]} \quad (A5)$$

$$G_{Reuss} = \frac{15}{4(s_{11} + s_{22} + s_{33}) - 4(s_{12} + s_{23} + s_{31}) + 3(s_{44} + s_{55} + s_{66})} \quad (A6)$$

where

$$c_{11} - c_{12} = \frac{1}{s_{11} - s_{12}}, \quad c_{11} + 2c_{12} = \frac{1}{s_{11} + 2s_{12}}, \quad c_{44} = \frac{1}{s_{44}} \tag{A7}$$

Also for silicon due symmetries in the fcc structure

$$c_{11} = c_{22} = c_{33}, \quad c_{12} = c_{23} = c_{31}, \quad c_{44} = c_{55} = c_{66} \tag{A8}$$

The values of c_{ij} and s_{ij} are shown in table A1 [35]. Using these values in the aforementioned equations, the Voigt-Reuss-Hill bounds are calculated and listed in table A2. These bounds are independent of texture and the actual stress values should lie between those values. If a certain texture is assumed, then the bounds may change significantly [70].

Table A1. Silicon stiffness, c_{ij}, and compliance, s_{ij}, elastic constants

$c_{11}=c_{22}=c_{33}$ (GPa)	$c_{12}=c_{23}=c_{31}$ (GPa)	$c_{44}=c_{55}=c_{66}$ (GPa)	$s_{11}=s_{22}=s_{33}$ $(GPa)^{-1}$	$s_{12}=s_{23}=s_{31}$ $(GPa)^{-1}$	$s_{44}=s_{55}=s_{66}$ $(GPa)^{-1}$
165.7	63.9	79.56	0.00768	-0.00214	0.0126

Table A2. Voigt - Reuss bounds for the elastic constants of polysilicon

	E, Young's modulus (GPa)	**ν, Poisson's ratio**
Isostrain Voigt model	165.82	0.218
Isostress Reuss model	159.44	0.229